AFIT/GAE/ENY/91D-27

ANALYSIS OF AN ADVANCED FIGHTER AIRCRAFT USING JET FLAP TECHNIQUES AND THE VORTEX LATTICE METHOD

Thesis

Steven P. Snyder, Captain, USAF

AFIT/GAE/ENY/91D-27

AFIT/GAE/ENY/91D-27

ANALYSIS OF AN ADVANCED FIGHTER AIRCRAFT USING JET FLAP TECHNIQUES AND THE VORTEX LATTICE METHOD

Thesis

Presented to the Faculty of the School of Engineering
of the Air Force Institute of Technology
Air University
In Partial Fulfillment of the
Requirement for the Degree of
Master of Science in Aeronautical Engineering

Steven P. Snyder, B.S.
Captain, USAF

December 1991

Acknowledgements

I would like to acknowledge Dr. Milton Franke, advisor, who provided support and guidance for this project; Mr. Ray Fredette, the designer of many interesting aircraft, who contributed a subject which made this study more than just an academic exercise; and Mr. Jim Snyder, aerodynamicist, who provided his personal analysis program and patiently endured countless questions and blank stares. I would also like to thank my father, Don Snyder. He sowed the seeds early in my life which instilled within me a love of aviation. Without him, I never would have made it to this point.

Most of all, I would like to thank my wife, Vicke, who provided the endless love, support, and understanding which made this all bearable.

Steven P. Snyder

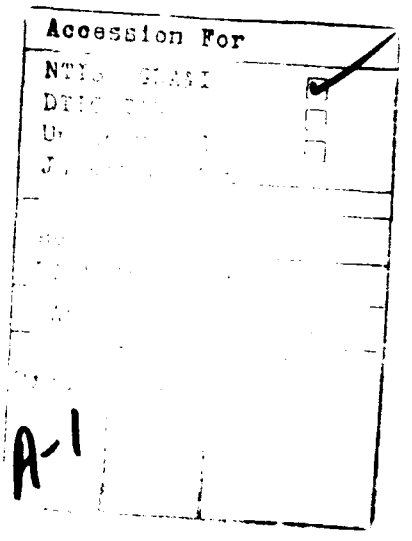

Table of Contents

List of Figures

List of Tables

List of Symbols

AR	Aspect Ratio
b	Span
BC	Blowing Condition
c	Chord
$\bar{c}$	Mean Aerodynamic Chord
C_{Di}	Induced Drag Coefficient
cg	Center of Gravity
C_J	Blowing Coefficient, Gross
$C_{L\alpha}$	Lift Curve Slope
C_l	Two Dimensional Lift Coefficient
C_L	Three Dimensional Lift Coefficient
C_M	Moment Coefficient
$C_{m,n}$	Influence Coefficient
C_μ	Blowing Coefficient, 2D
deg	Degree
F'	Force Per Unit Span Acting on Jet
FS	Fuselage Station
l	length
L	Lift
L'	Lift Per Unit Span
m_j	Mass Flow Rate of Jet
m'_j	Mass Flow Rate of Jet Per Unit Span
N	Total Number of Panels
p	Pressure

q	Dynamic Pressure
r	Radial Distance
R	Jet Sheet Deflection Radius
S	Area
SM	Static Margin
TR	Taper Ratio
V	Induced Velocity
v_j	Jet Velocity
w	Nondimentionalized Downwash
α	Angle of attack
γ	Circulation per Unit Area
Γ_c	Wing Circulation Per Unit Span
Γ_j	Jet Circulation Per Unit Span
Γ_{mn}	Local Circulation
δ_j	Flap Deflection Angle
δ_{mn}	Kronecker Delta
θ	Jet Sheet Curvature Angle
λ	Taper Ratio
$\Lambda_{c/2}$	Sweep of Wing Half Chord Line
ρ	Air Density

Subscripts

CLmax	Pertaining Maximum Lift
i	Induced Parameter
j	Pertaining to the Jet
L=0	Pertaining to Zero Lift Conditions

m	Panel of Current Interest
n	Influencing Panel
∞	Freestream Condition

Abstract

A computer code employing the vortex lattice method with modified boundary conditions was used to determine the induced aerodynamic characteristics of high aspect ratio, vectoring, exhaust nozzles located at the wing root of a canard configured fighter aircraft. Comparison with existing wind tunnel data verified results of the method. The exhaust was modeled as a singularly blown jet flap at deflection angles of -10, 0, 10, 20, 30, and 40 degrees. Jet momentum coefficients were based gross engine thrust for maximum afterburner and military power settings at a Mach number of 0.6 and an altitude of 20,000 ft. Lift, induced drag, and pitching moment coefficients were calculated for untrimmed conditions. The nozzle provided lift augmentation at all deflections and blowing conditions, a reduction in induced drag at high lift coefficients, and an increased nose down pitching moment. An optimum flap deflection to achieve minimum induced drag existed for each unique lift and blowing condition. Measurement of the static margin showed that the aircraft as configured was statically unstable. Example cases of comparable wing planforms varying in aspect ratio from 2 to 5 and taper ratio from 0.05 to 1 showed similar behavior.

ANALYSIS OF AN ADVANCED FIGHTER AIRCRAFT USING JET FLAP TECHNIQUES AND THE VORTEX LATTICE METHOD

I. Introduction

Conceptual aircraft design generally concerns itself with trends or technology that may be 15 to 20 years in the future. At this early point in the life of an aircraft, the designer must be able to comprehend how proposed technologies will enable accomplishment of requirements put forth. This comprehension leads to well founded decisions throughout the process. One technology which has been proposed for use on advanced aircraft for many years is the jet flap.

In the case of this study, the designer, Mr Raymond Fredette, proposed the use of a very high aspect ratio jet exhaust nozzle located at the wing/body juncture of a canard fighter configuration.(See Figure 1) One reason for incorporating this type of nozzle was to improve the drag polar of the aircraft due to the increase in circulation provided by a jet flap. There were also survivability benefits and weight penalties to be investigated. The key question was whether or not the benefits would outweigh the penalties.

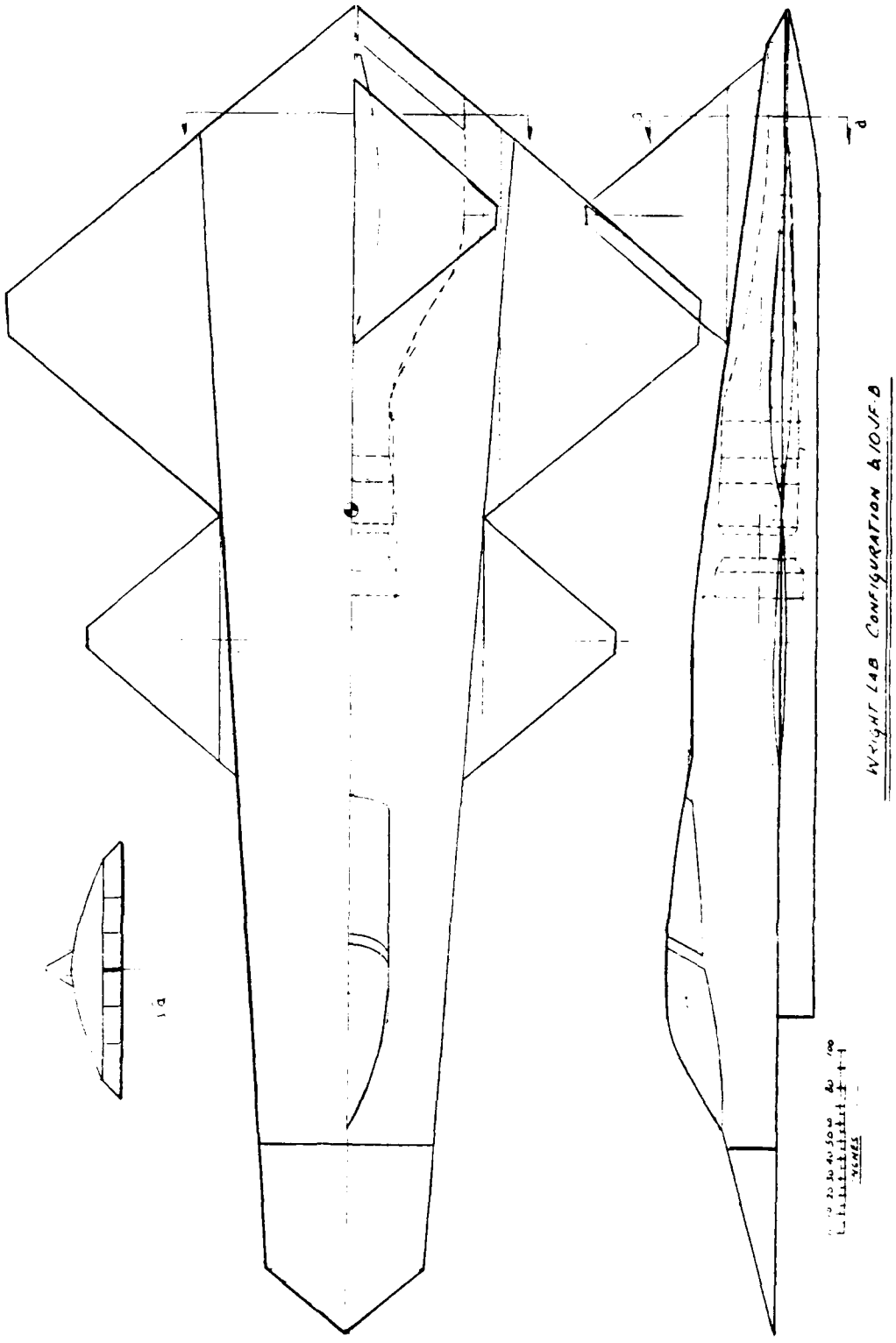

Figure 1 Wright Lab b.10JF-B Two View

Fredette had no verified aerodynamic methods to predict the effects of the nozzle. Additionally, the aircraft itself was pushing the capability limits of existing empirical methods because of its unusual configuration. He believed that some sort of computational method was needed to generate useful aerodynamic data. By treating the thin, vectored exhaust like a jet flap, it was felt that worthwhile aerodynamic coefficients could be determined. After studying several methods of calculating jet flap effects, a vortex lattice method with modified boundary conditions was selected.

A secondary study of generic wing planforms similar in aspect ratio and taper ratio to the b.10JF-B wing was also performed in order to demonstrate the effects of varying wing parameters on the aerodynamic characteristics of a jet flapped wing.

II. Background

1 The Jet Flap

According to Kohlman, (Ref 2), Shubauer first proposed the jet flap in 1932. Kohlman goes on to state that Hagedorn and Ruden carried out the initial experimental work in 1938. The concept involves a sheet of high velocity air blown from a thin slot near the trailing edge of a wing. Because the sheet has a finite amount of momentum, it can support a pressure difference which deflects the freestream. (Ref 14) This is analogous to the Kutta condition being met somewhere aft of the trailing edge. The result is an increase in lift beyond the circulation lift of the wing and the lift component of jet thrust. According to McCormick, under strong blowing conditions, the jet can also act like a boundary layer control device and delay leading edge separation, resulting in 6 to 8 degree increments in α_{CLmax}

The change in induced drag compared to a standard wing depends on the amount of blowing and flap deflection, δ_j. Induced drag reduction is realized at high lift conditions while some penalty is paid at low lift. There is a point in between these conditions where the unblown and blown drag polars cross over each other. This point is dependant on the amount of blowing and the flap deflection.

Theoretically, all thrust from the deflected jet is recovered if it is turned parallel to the freestream.

However, due to a finite value of downwash at infinity, a fraction remains unrecovered and is accounted for as an induced drag component, $C_{D_{jet}}$. Some thrust is also lost due to friction at the jet/freestream boundary.(Ref 14) One penalty paid is in the form of a severe nose down pitching moment at high lift conditions. The drag associated with trimming this moment can be significant enough to outweigh many benefits.

Jet flaps come in two distinct varieties. The first is a singularly blown flap where the jet sheet exits the wing at the trailing edge and is vectored by a nozzle arrangement. The second type is known as a blown flap. It blows the jet over a mechanical flap which deflects it due to the Coanda effect. Each concept has its shortcomings. The singularly blown flap is tough to incorporate both structurally and mechanically into a thin trailing edge, while the blown flap has problems with the hot exhaust interacting with the flap. This study will model the jet exhaust as a singularly blown flap.

Confusion sometimes exists between the concepts of the jet flap and circulation control since they both use a form of blowing to achieve high lift conditions. With circulation control, a thin jet of air is blown over a rounded trailing edge, eliminating the Kutta condition. This moves the aft stagnation point to the lower surface,

thereby increasing circulation and lift.(Ref 14) On the other hand, the primary purpose of blowing in a jet flap is to add momentum to the wake in order to support a pressure discontinuity. Each method has different means of achieving similar objectives.

1.1 Applications of Blowing

One of the few purely jet flapped aircraft to fly, was the Hunting H.126. (Ref 2, 15) Engine air was ducted solely to full span, blown flaps along the trailing edge of this research aircraft. All thrust used to propel the aircraft in forward flight came from the jet flaps.

Two forms of blown flaps were utilized in competing prototypes for the Air Force Advanced Medium STOL Transport (AMST) program in the 1970s. (Ref 15) McDonnell Douglas used an externally blown flap on its entry, the YC-15. The exhaust of its underwing mounted turbofan engines was blown through large two-segment slotted flaps. Boeing employed upper surface blowing on the YC-14. The exhaust from its over the wing mounted engines was deflected downward over large flaps via the Coanda effect.

The Navy tested a rather bulky circulation control high lift device on a Grumman A-6 in the late '70s. (Ref 2) Bleed air pulled from the engines was ducted through plenums mounted at the trailing edges. A slot running lengthwise along the plenums provided an exit for the jet sheet. The

rounded outer surface of the plenum acted as a Coanda surface in order to deflect the flow. In order to counter the strong nose down pitching moment, the horizontal stabilizer was increased in area and recountoured with an extreme negative camber.

Blowing is typically associated with lift enhancement in aircraft. However, reference 6 proposed the use of a circulation control stern plane on a submarine. The purpose was to prevent a catastrophic crash dive which could be caused by a mechanical stern plane becoming jammed.

1.2 Jet Flap Theory

The basis for most analytical theory of the jet flap can be attributed to D. A. Spence of the Royal Aircraft Establishment. (Ref 17) The following development was adapted from Reference 14. Spence used a control volume approach to represent the jet exiting the trailing edge of the wing. Although it entered at some angle against the free stream, he reasoned that it would eventually be turned parallel. The pressure, Δp which turned the jet, transferred itself in part to the lifting surface. Figure 2 depicts this concept in schematic form.

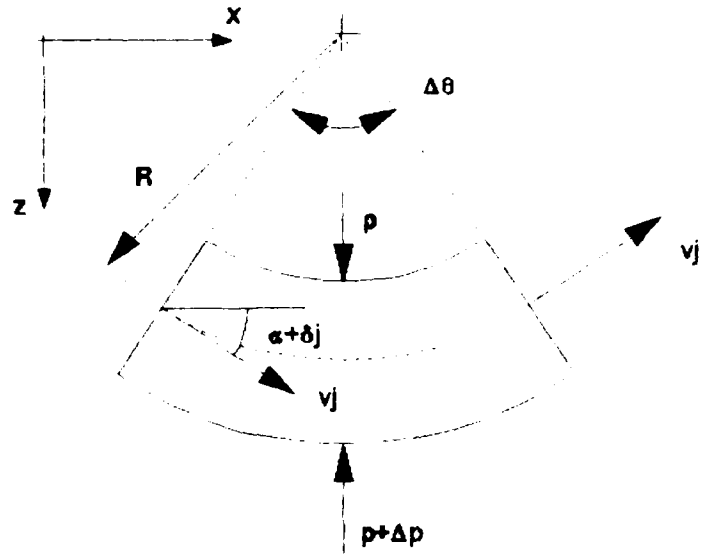

Figure 2 Jet Control Volume (Adapted From Spence)

Applying the momentum equation to the control volume,

$$m_j' v_j \Delta\theta = \Delta p R \Delta\theta \tag{1}$$

and solving for Δp,

$$\Delta p = \frac{m_j' v_j}{R} \tag{2}$$

The force per unit width acting on the jet is,

$$F' = \Delta p R \Delta\theta \tag{3}$$

Using a vortex with strength per unit width, the force can be represented by:

$$F' = \rho_\infty V_\infty \gamma R \Delta\theta \tag{4}$$

Solving for γ as circulation due to the jet, γ_j,

$$\gamma_j = \frac{m_j' v_j}{\rho_\infty V_\infty R} \tag{5}$$

With a large radius of curvature and small $\Delta\theta$, this becomes

$$\gamma_j = \frac{-m_j' v_j}{\rho_\infty V_\infty} \frac{d^2 z}{dx^2} \tag{6}$$

Integrating γ_j from the trailing edge to infinity yields Γ_j, jet induced circulation per unit span.

$$\Gamma_j = \frac{-m_j' v_j}{\rho_\infty V_\infty} \int_0^\infty \frac{d^2 z}{dx^2} dx = \frac{m_j' v_j}{\rho_\infty V_\infty} (\alpha + \delta_j) \tag{7}$$

given small values of α and δ_j. The total two dimentional lift coefficient is then expressed as a combination of factors due to the airfoil and the jet.

$$C_l = \frac{2\Gamma_c}{V_\infty c} + \frac{m_j' v_j}{q_\infty c} (\alpha + \delta_j) = \frac{2\Gamma_c}{V_\infty c} + C_\mu (\alpha + \delta_j) \tag{8}$$

where the blowing coefficient, C_μ, is the primary nondimensional parameter used in describing jet momentum in two dimentions. C_J is a gross blowing, or jet coefficient for three dimentions.

$$C_\mu = \frac{m_j' V_j}{q_\infty c} \qquad C_J = \frac{m_j V_j}{q_\infty S} \tag{9}$$

The solution of Γ_c and Γ_j involves a pair of simultaneously solved integro-differential equations.

Spence graciously provided curve fit solutions to the equations, Eq (10).

$$\frac{\partial C_l}{\partial \delta} = \left[4\pi C_\mu \left(1 + 0.151 C_\mu^{\frac{1}{2}} + 0.139 C_\mu\right)\right]^{\frac{1}{2}}$$

$$\frac{\partial C_l}{\partial \alpha} = 2\pi\left(1 + 0.151 C_\mu^{\frac{1}{2}} + 0.219 C_\mu\right) \qquad (10)$$

$$C_l = \frac{\partial C_l}{\partial \alpha}\alpha + \frac{\partial C_l}{\partial \delta_j}\delta_j$$

These allow painless determination of jet flapped airfoil solutions.

Spence continued on to a three dimensional solution with Maskel. A very good description of this method is found in Reference 14. However, the solution assumes that the lift distribution and the blowing coefficient vary elliptically over the span. Because this is an idealized case, and the objective of this study was to analyze a specific configuration, a method with more flexibility was pursued.

2 The Vortex Lattice Method

One of the primary computational methods used to model the jet flap has been the vortex lattice method. Using boundary conditions similar to those set up by Spence, the jet sheet can be modeled as a component interacting with wing and body.(Ref 4)

The level of detail involved with methods varies greatly from code to code. The author wrote a relatively short BASIC program as an undergraduate to solve for the incompressible aerodynamic coefficients of basic planar geometries. On the other hand, Douglas Aircraft developed the Elementary Vortex Distribution, or EVD, panelling code which modeled circulation singularities at the wing leading edge with square root singularities and hinge lines with logarithmic singularities.(Ref 13)

2.1 Vortex Lattice Theory

The theoretical development described here is actually from a combination of sources. (Ref 3,4,5) Some variable and indices have been changed to assure uniformity. Essentially, the vortex lattice method models the velocity induced by a wing of finite aspect ratio with a distribution of horseshoe vortices. Each vortex is of a strength which satisfies a set of boundary conditions. These strengths are solved simultaneously over the planform with a system of linear equations. Given the strengths, the aerodynamic characteristics of the configuration can then be determined.

The foundation of vortex lattice theory is the Biot Savart law, which is used in determining the velocity induced by any given vortex filament at a particular control point. In vector form:

$$d\vec{V} = \frac{\Gamma_n(d\vec{l} \times \vec{r})}{4\pi r^3} \tag{11}$$

integrating Eq (11) determines the induced velocity at a given point in space for a given vortex strength, Γ_n.

$$V = \frac{\Gamma_n}{4\pi r_p}\int_{\theta_1}^{\theta_2} \sin\theta \, d\theta = \frac{\Gamma_n}{4\pi r_p}(\cos\theta_1 - \cos\theta_2) \tag{12}$$

and

$$r_p = \frac{|\vec{r}_1 \times \vec{r}_2|}{r_0} \qquad \cos\theta_1 = \frac{\vec{r}_0 \cdot \vec{r}_1}{r_0 r_1} \qquad \cos\theta_2 = \frac{\vec{r}_0 \cdot \vec{r}_2}{r_0 r_2} \tag{13}$$

so that

$$\vec{V} = \frac{\Gamma_n}{4\pi}\frac{\vec{r}_1 \times \vec{r}_2}{|\vec{r}_1 \times \vec{r}_2|^2}\left[\vec{r}_0 \cdot \left(\frac{\vec{r}_1}{r_1} - \frac{\vec{r}_2}{r_2}\right)\right] \tag{14}$$

The most general form of Eq (14) is the formula for the induced velocity of a straight infinite vortex filament,

$$V = -\frac{\Gamma_n}{2\pi r} \tag{15}$$

Figure 3 shows a generic vortex filament and its associated parameters.

According to the Helmholtz theorem, any vortex in inviscid flow must either, extend to infinity, terminate at a wall, or form a closed loop. (Ref 14) In the case of the horseshoe vortex in Figure 4, points A and B define the bound portion of the vortex, and both ends trail off to

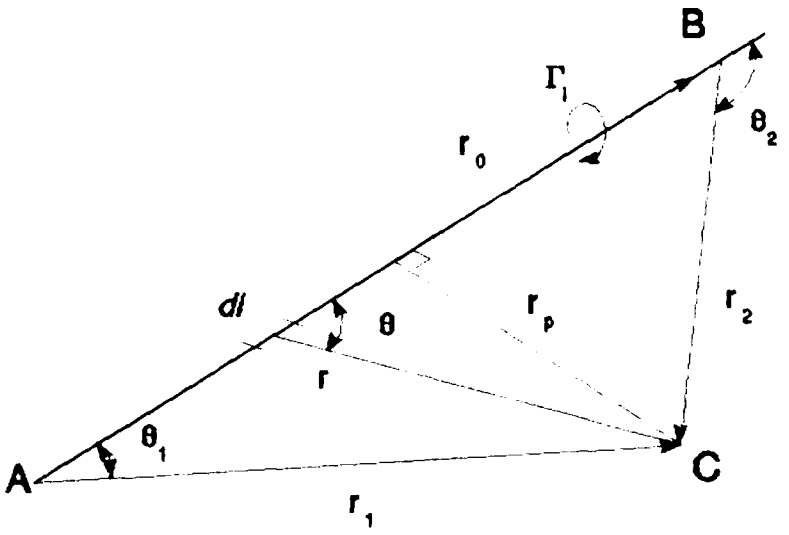

Figure 3 Vortex Filament (From Bertin, et al.)

positive infinity. The induced velocity at a point may be determined once the influences of the individual segments are known. Due to the linear nature of potential flow and its elementary flows, the influences of the legs may then be added together to get the total velocity. In turn, the induced velocity at any given point may be determined by summing the contributions of all the other horseshoe vortices.

Assuming the wing in Figure 5 is to be studied, modeling begins with dividing the planform up into spanwise and chordwise panels. Each panel corresponds to a horseshoe vortex.(The distribution of these panels will be discussed later.) The sides of each panel are parallel to the X axis, and their fore and aft sides follow the taper of the wing.

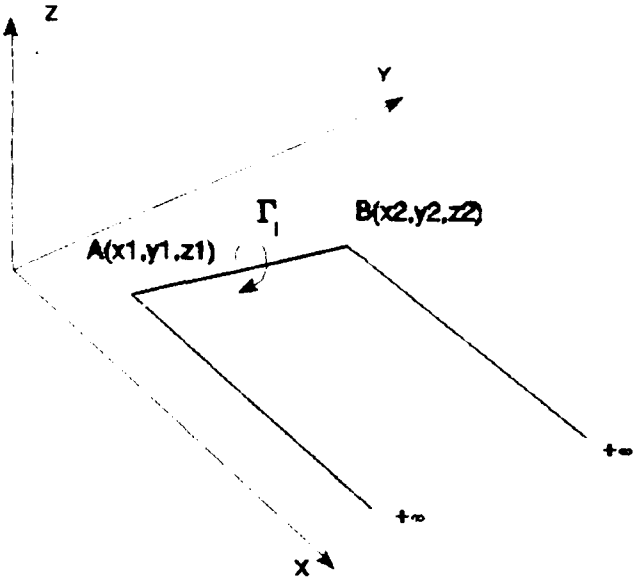

Figure 4 Horseshoe Vortex (From Bertin, et al.)

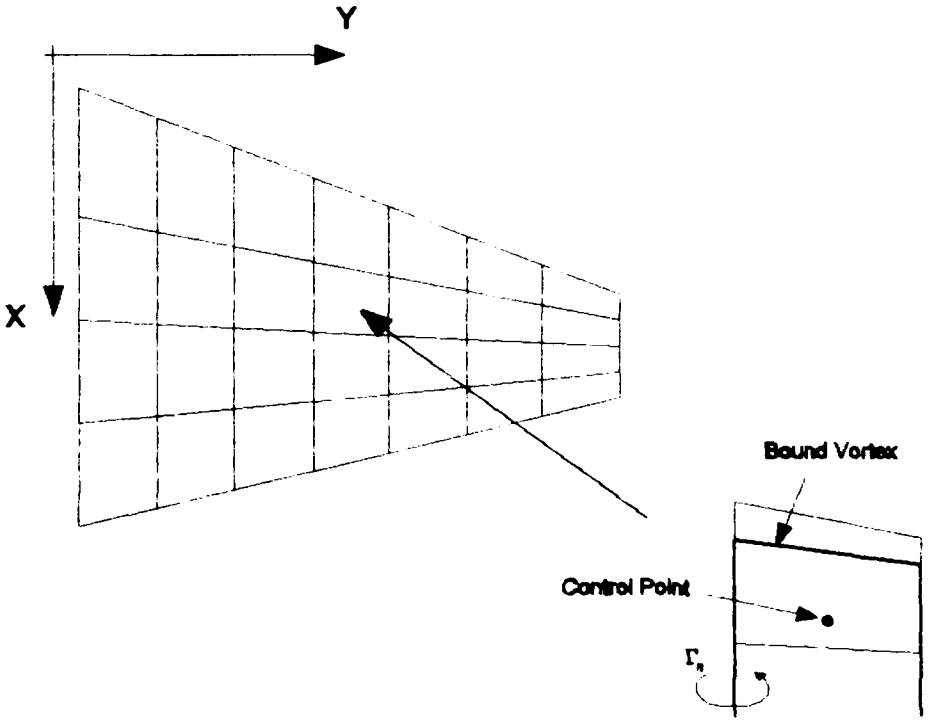

Figure 5 Paneled Wing

A horseshoe vortex is bound to the quarter chord of every

panel and the free ends are allowed to trail back to infinity in the X direction. Surface boundary conditions are enforced at the control points located at the 3/4 chord location, midway between the sides.

The following notation is helpful when summing up velocities. The panel number of the current control point is represented by the m index, and n represents a horseshoe vortex influencing it, such that:

$$\vec{V}_{m,n} = \vec{C}_{m,n}\Gamma_n \tag{16}$$

C is the influence coefficient based on the location and orientation of the vortex. It is the only known portion of Eq (14) since it is determined by geometry alone. Summing the individual velocities together,

$$\sum_{n=1}^{N} \vec{C}_{m,n}\frac{\Gamma_n}{V_\infty} = \vec{V}_m \tag{17}$$

Where the right hand side is the normalized velocity at induced at control point m. The left hand side sets up a system of linear equations which may be solved for Γ_n/V_∞. Boundary conditions specify the normalized velocity.

2.1.1 Boundary Conditions

Boundary conditions for the vortex lattice method result from the requirement that the flow be tangential to the surface at the control points located at the 3/4 panel chord, and mid panel span. The easiest way to enforce this

constraint is to force the normal component of velocity to zero at all control points.

$$(\vec{V}_\infty + \vec{V}_m)\cdot\hat{n} = 0 \tag{18}$$

The system of linear equations is then solved using the matrix inversion technique of choice.

2.2 Calculation of Aerodynamic Coefficients

Once the individual panel circulations are calculated, the values may be used to determine the forces acting on individual panels. Starting with the Kutta-Jukowski law in its most general form,

$$\vec{F} = \int_{s_1}^{s_{1+1}} \rho \vec{V} \times \vec{\Gamma} ds \tag{19}$$

The lift per unit span becomes

$$L' = \rho_\infty V_\infty \Gamma \tag{20}$$

and C_L is solved in terms of the local singularities in both the chordwise and spanwise directions.

$$C_L = \frac{4}{S} \sum_{n=1}^{N} \frac{\Gamma_n}{V_\infty} \Delta y_n \tag{21}$$

N is the total number of panels on one half of a symmetric wing. The moment is simply the summation of the various panel lift contributions multiplied by the moment arm from the point of interest to the panel vortex location.

$$C_{M_{cg}} = \frac{-4}{S\bar{C}} \sum_{n=1}^{N} \frac{\Gamma_n}{V_\infty}(x_n - x_{CG})\Delta y_n \qquad (22)$$

The induced drag coefficient is slightly more complicated. For the near field drag value used in this study, the induced velocity normal to the surface at the local bound vortex must be determined. This velocity then takes the place of V_∞ in Eq (20), and the summation becomes

$$C_{D_i} = \frac{4}{S} \sum_{m=1}^{N} \sum_{n=1}^{N} C_{m,n} \frac{\Gamma_m}{V_\infty} \frac{\Gamma_n}{V_\infty} \Delta y_n \qquad (23)$$

2.3 Application Of The Jet Flap

Applying the jet flap to the vortex lattice method is an exercise in enforcing a specific set of boundary conditions over an additional set of panels representing the jet sheet. Since the jet sheet supports a pressure discontinuity, it can be modeled with a typical horseshoe vortex panel. The following development was adapted from Bonner et al. Some variables and indices have been renamed for the sake of continuity.

The change in jet inclination due to the pressure discontinuity causes the major difference to boundary conditions.

First, starting over with Eq (4)

$$F' = \rho_\infty V_\infty \gamma R \Delta\theta \tag{4}$$

and note that for a large radius of curvature,

$$\frac{1}{R} \approx \frac{d^2z}{dx^2} = \frac{dw}{dx} \tag{24}$$

where w represents the downwash nondimentionalized with respect to V_∞ and dw/dx represents its change along the length of the jet. Then

$$\frac{\gamma_j}{V_\infty} = \frac{m_j' v_j}{\rho_\infty V_\infty^2 R} = \frac{m_j' v_j}{\rho_\infty V_\infty^2} \frac{dw}{dx} = \frac{1}{2} c C_\mu \frac{dw}{dx} \tag{25}$$

or

$$c C_\mu \frac{dw}{dx} - 2\frac{\gamma_j}{V_\infty} = 0 \tag{26}$$

Integrating this equation in the x direction, between control points

$$c C_\mu \int_{x_{m-1}}^{x_m} \frac{dw}{dx} dx - 2 \int_{x_{m-1}}^{x_m} \frac{\gamma_j}{V_\infty} dx = 0 \tag{27}$$

resulting in

$$c C_\mu [w_m - w_{m-1}] - 2\frac{\Gamma_n}{V_\infty} = 0 \tag{28}$$

Given the fact that w is a function of Γ, the governing equation becomes

$$\sum_{n=1}^{N} \left[cC_{\mu}(C_{m,n} - C_{m-1,n}) - 2\delta_{m,n} \right] \frac{\Gamma_n}{V_{\infty}} = 0 \qquad (29)$$

where δ_{mn} is the Kronecker delta. (Not to be confused with δ_j, the flap deflection angle) The jet panel adjacent to the jet exit must take into account the flap deflection angle relative to the wing.

$$cC_{\mu}\left[w_m - (w_{m-1} + \delta_j) \right] - 2\frac{\Gamma_n}{V_{\infty}} = 0 \qquad (30)$$

Now, the summation becomes:

$$\sum_{n=1}^{N} \left[cC_{\mu}(C_{m,n} - C_{m-1,n}) - 2\delta_{m,n} \right] \frac{\Gamma_n}{V_{\infty}} = cC_{\mu}\delta_j \qquad (31)$$

Essentially, this means that the influence coefficient on the jet, $C_{m,n}$, becomes a function of the traditional influence coefficient on the current panel and the one immediately aft of it.

$$C_{m,n_{jet}} = cC_{\mu}(C_{m,n} - C_{m-1,n}) - 2\delta_{m,n} \qquad (32)$$

on the jet, and the right hand side becomes:

$$\begin{array}{ll} cC_{\mu}\delta_j & \text{on the jet, adjecent to the nozzle} \\ 0 & \text{elsewhere} \end{array} \qquad (33)$$

2.4 Panel Distribution

Panel distribution remains as one of the few black arts left regarding paneling methods. The fact that the vortex

lattice method actually solves the flow only at the control points implies that it probably misrepresents certain phenomena. One of the primary things it does miss are the singularities in the vorticity distribution at the leading edge and hinge lines. One solution to this problem increases panel density in the location of a singularity. However, this quickly eats up computer time and storage, and some codes may only have a limited number of panels to use. The McDonnell Douglas EVD Method (Ref 13) models the chordwise circulation at these points with logarithmic and inverse square root singularities. Another approach to increase convergence, using significantly fewer panels, is to space the wing tips and hingelines fractions of panel widths from their actual boundaries.

The number of spanwise panels necessary for a given convergence has been shown to be significantly reduced by insetting the wing tip 1/4 of a panel span. Hough proved this by deduction for an elliptic planform. By induction, he shows it to be the case for wings with sweep and constant chord.

A similar method exists when modeling the circulation singularity existing at a flap hingeline. The bound vortex of the flap panel will better represent the circulation if it overlaps the flap and wing by approximately 1/4 of a

panel chord. (Ref 19) This places it closer to the hingeline.

In general, adjacent panels should be kept relatively similar in size and shape. Significant differences will exist between the root and tip panels of a highly tapered wing, but the variation is minimal from panel to panel. This rule becomes important when joining separate components like a wing and flap. Adjacent panels should be aligned and of the same span. The chords should also be similar.

2.5 Jet Sheet Convergence

Theoretically, the jet sheet extends to infinity. To limit the size of the model, an investigation was conducted to determine the minimum sheet length required to achieve acceptable convergence. A wing planform was run with jet sheets varying in length from 1 to 10 chord lengths. The lift coefficient converged to within 0.1% of the final value in three chord lengths. The bound vortex strengths on the jet sheet were negligible aft of this point.

3 Planform Study

This additional investigation was included to give the reader some idea of how the characteristics of a wing planform affect the influence of the jet flap, especially for lower aspect ratio wings. The study varied planform AR from 2 to 5 and λ from 0.05 to 1. Table I lists the

parameters which specifically describe each planform. Each case was run for the following values of α, δ_j and C_μ.

α = 0, 5, 10, 15, 20 deg

δ_j = 0, 15, 30 deg

C_μ = 0, 0.5, 1.0

Table I Planform Study Wing Parameters

AR	λ	b (1)	S (1^2)	$\bar{c}$ (1)	$\Lambda_{c/2}$ (deg)
2	0.05	2.121	2.25	1.35	0
2	0.25	2.121	2.25	1.188	0
3	0.05	2.598	2.25	1.102	0
3	0.25	2.598	2.25	0.97	0
3	0.5	2.598	2.25	0.898	0
5	0.5	3.354	2.25	0.696	0
5	1	3.354	2.25	0.671	0

4 Vortex Lattice Software

The computer code used in this study, LATJET, was written by Mr James Snyder, ASD/XRH. (Ref 18) LATJET allows relatively complex shapes to be developed. Components are developed by defining chords from root to tip. Subcomponents between chords are divided into evenly spaced spanwise and chordwise panels. Up to 300 panels may be defined.

Camber and twist are modeled by modifying the local angle of attack at a given panel to account for the variation in surface slopes. The local angle of attack is factored into the boundary conditions when the vortex lattice method constructs the set of linear equations. Slopes can be input by hand or a table may be created using CAMBER. CAMBER is a FORTRAN code developed in house by ASD/XRH for producing specific camber distributions. Camber lines may be defined in one of several ways.(Ref 7) One method generates camber lines given a combination of one or more NACA airfoil types. Lines are defined at both inboard and outboard chords so that spanwise variations can be determined by interpolation.

The jet sheet is defined as an individual component linked to the trailing edge of another. C_μ and δ_j are specified on a strip by strip basis.

At subsonic speeds, the program uses vortex lattice panels, while above Mach 1, constant pressure panels are employed. A Prandtl-Glauret correction accounts for compressibility. The set of linear equations is solved using Lower Upper decomposition. This solution method allows a significant reduction in computation time if multiple boundary conditions such as camber, control deflections or α, are to be run for the same geometry.

The LATJET output file can vary greatly in size depending the settings of the user defined print options. Individual component, strip or panel information may be output in addition to a final table which contains the resulting aerodynamic, moment and jet flap coefficients of the model being studied.

Since the method is predicated upon potential flow, no viscous effects are modeled. This is especially important when looking at the C_L vs α curves. No maximum lift coefficient is implied. The relationships are linear. In this case, the designer will use empirical methods to determine the effects of viscosity. All components are assumed to be thin, $t/c << 1$.

5 Data Collection

LATJET was run on the VMS cluster at the Air Force Institute of Technology. Individual data cases were piggy-backed into large files with similar blowing conditions. These files were then processed in the background mode using multiple batch files. A FORTRAN sorting code distilled the large output files into manageable sized ASCII files. Finally, these data files were imported into Quattro® Pro 3.01 where they were parsed and lumped into a large relational data-base. Data could be plotted at will for any available choice of parameters using a custom made spreadsheet.

III. Aircraft Configuration

1 Design Philosophy

The personal philosophy behind the design of the b.10JF-B is described by Fredette in Appendix A and reference 8. One potential benefit derived from choosing the high aspect ratio nozzle is survivability. It is widely circulated in open literature that a nozzle of this type masks hot parts and mixes the exhaust plume.(Ref 16) In addition to the jet flap benefits mentioned, there is also the prospect that this type of nozzle can reduce the boat-tail drag (drag caused by the separation of airflow over the aft portion of the fuselage), if it can induce favorable flow conditions over the aft portion of the fuselage.

The advantages of the jet flap seem very lucrative. However, there are several disadvantages. The primary are: nozzle weight and the additional fuselage weight acquired when accommodating the greater transition section weight, length, and width of the nozzle. Using first order estimates, the nozzle and transition section combination can constitute from 40 to 60 percent of the bare engine weight.(Ref 8) Weight penalties magnify several times when actual take off gross weight is addressed. In the case of the b.10JF-B configuration, each additional pound of nozzle weight increased the gross weight by 3.9 pounds when considering the extra body weight and additional fuel

required to meet mission radius requirements. Complexity is another detractor. However, standard nozzles, especially two dimensional vectoring types, are approaching the jet flap in overall complexity. The extreme length of the nozzle and the fact that it must transition the flow from a round to rectangular cross section indicates that propulsive losses will be higher than standard. If the nozzle reduces boat-tail drag, the length could be shortened. The shorter transition will create steeper slopes at the aft end, but separation conditions might be avoided due to favorable influence the flowfield by the jet.

2 Requirements and Figures of Merit

When determining whether or not the nozzle will be of benefit to the aircraft, there are several performance requirements to be considered. These requirements, set at the beginning of the design study, can be divided into two main categories, maneuverability and mission performance. Maneuverability concerns itself with the aircraft's performance at specific points in the operating envelope usually defined with Mach number, altitude, and power setting. The different criteria include instantaneous turn rate, sustained turn rate and specific excess power. Mission performance deals with ranges, loiter times, take-off distance, etc.

Generally two or three of these requirements play a pivotal role in sizing the wing, engine and take-off weight. Instantaneous turn rate is directly related to the amount of lift the wing produces. Sustained turn rate depends on lift and the amount of associated drag that engine thrust must overcome. The specific engine and wing sizes chosen to fulfil these maneuverability criteria will then affect the overall weight of the aircraft needed to meet mission radius requirements. Generally, wing and engine sizes must be as small as possible in order to minimize take-off weight. This makes it crucial for the designer to have sound aerodynamic data early in the conceptual design process to optimize performance and maneuverability for the smallest possible weight. The fact that the lift and drag of this aircraft are linked directly to the propulsion system magnifies the significance of being able to predict the aerodynamic characteristics with accuracy and convenience.

As stated by the designer in Appendix A, page 63, the high aspect ratio nozzle can reduce the weight of the aircraft by improving the efficiency of the drag polar to a point where a wing with lower aspect ratio and/or area could be used. A smaller, lower aspect ratio wing generally weighs less, which thereby lowers the empty weight of the aircraft. The major question remaining is whether or not

this weight savings can offset the weight increase of the installed nozzle.

3 The Computational Model

3.1 Panelling

The model as specified to LATJET was essentially a planar configuration with a "butterfly tail." Four major components, the forebody, canard, wing and v-tail modeled

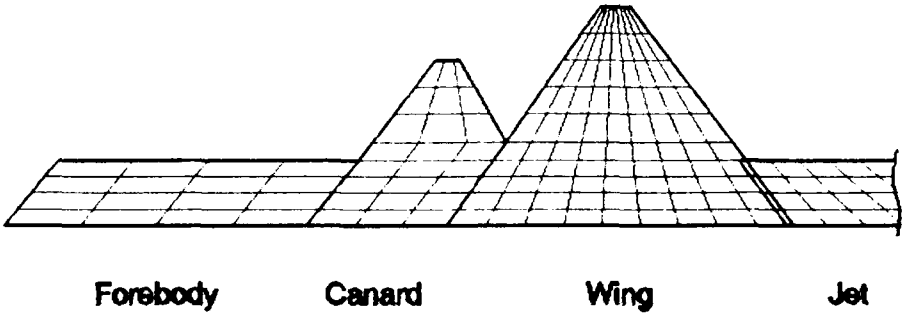

Figure 6 b.10JF-B Panel Model

the aircraft, and a single component represented the jet sheet. (See Figure 6) All tips and sides have been inset 1/4 of a panel width. The angled edge of the forebody has been approximated with a side parallel to the freestream. This was done in order to prevent extreme panel distortion caused by tapering a component to zero over a very small displacement in the Y direction. In order to represent the singularity at the jet, a 1/4 panel overlap was used as

recommended by reference 19. The jet sheet extends out three chord lengths past the trailing edge of the wing. Fredette supplied the NASA sharp edged transonic airfoil used in this study and seen in Figure 7. Since sizing the canard surface was one of the design objectives, the influence of wing camber was especially important in

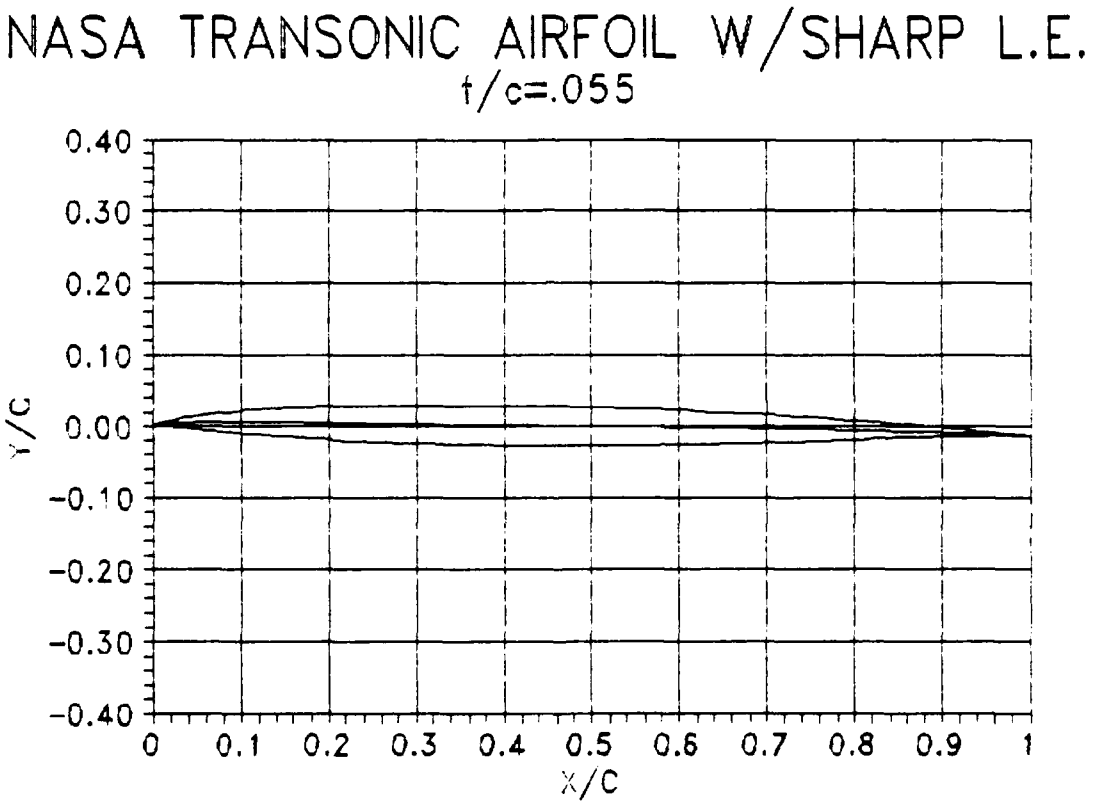

Figure 7 NASA Transonic, Sharp Leading Edged Airfoil

determining the overall pitching moment. A camber line constructed with upper and lower surface coordinates was input to CAMBER.FOR. No twist, or camber variation was assumed in the spanwise direction.

3.2 Blowing Coefficient

In calculating the blowing coefficients for this study, the $m_j v_j$ term was assumed to be equal to the gross engine thrust at the specified flight condition. The mass flow rate and velocity across the nozzle exit plane were also assumed to be constant. This implies that the nozzle has a constant height side to side. This also means that C_μ varies in the spanwise direction proportionally to the chord. As far as flight parameters go, C_μ was a function of Mach, altitude, and power setting.

All engine data supplied by the designer was generated with a parametric engine deck employing the characteristics in Table II. The resulting gross thrust data was multiplied by an engine scale factor of 1.169. When calculating C_μ, the $m_j v_j$ terms used were the gross thrust divided by the six panels across the exit plane of the nozzle.

Table II b.10JF-B Engine Characteristics

Bypass Ratio	1.0
Air Flow	350 lbm/sec
Overall Pressure Ratio	30
Turbine Inlet Temperature	3000°R

To comprehend the effects of fanning the exhaust out, a reference case was created to see the characteristics of a

configuration with a smaller 2D vectoring nozzle. For the comparison case, the exhaust spanned over a width of 36 inches (two panels) compared to 110 inches for the baseline.

3.3 Nozzle Vector Angle

The nozzle vector angle, or flap angle δ_j was allowed to vary from -10 to +40 deg. It was assumed to act as a singularly blown flap, and have a constant mass flow rate in the spanwise direction.

3.4 Modification for Control Surface Sizing

To remove the influence of the existing canard for the canard sizing process, the canard component was terminated at the buttline even with the forebody. Individual moment curves were generated for this modified configuration.

IV. Verification

1 Verification of Vortex Lattice Code

1.1 Two Dimensional Case With Camber (NACA 64-206)

The verification studies were initiated by creating a flat plate model with a constant chord of one unit and a span of 100 units. This provided a pseudo 2D approximation. The lift curve slopes came out to 2π/rad, and $\alpha_{L=0}$=0 deg.

Next, the functioning of the camber option was verified. Using the CAMBER program, a local angle of attack table was produced for a NACA 64-206 airfoil. This airfoil was chosen because it was relatively thin, its camber line could be easily generated by CAMBER.FOR, and its aerodynamic characteristics were readily available. The result are compared to values from Reference 1, in Table III.

Table III LATJET Comparison for NACA 64-206

	LATJET	Theory of Wing Sections
$C_{L\alpha}$ (deg^{-1})	.1095	.105
$\alpha_{L=0}$ (deg)	-2.07	-1.5
C_{Mac}	-.05	-.04

It should be reemphasized that although the example airfoil has a 6% thickness, no thickness was modeled.

1.2 Jet Sheet Convergence

Convergence of the aerodynamic parameters with respect to jet sheet length was alluded to earlier. Jet sheets of

varying lengths were attached to the trailing edge of the 2D flat plate. C_L was monitored as the sheet length increased. After approximately 3 chord lengths, the parameters converge to within 0.1% of the stabilized values.

1.3 Three Dimensional Wing With Camber

The b.10JF-B wing was analyzed without its jet sheet. $C_{L\alpha}$ results were compared to analytic values. According to Hough (Ref 10), Eq (34) is accurate to 0.75% for $16 \geq AR \geq 1$.

$$C_{L_\alpha} = \frac{2\pi AR}{AR + 2.903 + \frac{.377}{AR}} \tag{34}$$

The results are found in Table IV. Values for the wing with camber are also included. The negative zero lift angle of attack indicates that the camber is generating lift at $\alpha=0$ deg.

Table IV Analytic and Computational Values for b.10JF-B Wing

	Analytic	Plain Wing	Wing w/Camber
$C_{L\alpha}$ (deg^{-1})	.0431	.0463	.0463
$\alpha_{L=0}$ (deg)	-	0	-.9365

1.4 NADC Jet Flapped Fighter Study

With the conventional aspects of LATJET checked out, the jet flap results needed evaluation. There is a great deal written about the jet flap. However, finding valid,

well presented wind tunnel data is very difficult. Quite a bit of data is available on blown flaps and upper surface blowing, but singularly blown jet flaps is another matter. Reference 9 was the only document located which involved a relatively simple configuration with a singularly blown flap.

In reference 9, Hemmerly presents data for a family of tapered wings with and without tip plates and washout. The jet flap was intended strictly as a fixed high lift device which would vary its effect by modifying C_J. Air exits from a thin, spanwise, constant height slot placed just above a trailing edge with a small radius of curvature. A jet deflection angle of 65 deg was determined by tufting the trailing edge. Hemmerly made no mention as to how varying flight conditions and blowing coefficients affected the deflection.

While reviewing data from this study, the importance of properly presenting all assumptions and book keeping schemes became apparent. In general, drag is assumed to be positive when measured in the direction of V_∞. With the reaction force of a jet flap to consider, the net force in this direction may actually be negative when measured by a balance in a wind tunnel. This would indicate that the thrust component of the jet has overcome the drag of the wing. This isn't always obvious if the drag never becomes

negative, which was the case with the NADC study. The drag presented in the report included the thrust component of the jet flap (strictly as measured from the force balance). Drag curves compared here include the thrust of the jet.

Another confusing aspect was the calculation of the blowing coefficient. The C_μ values as specified actually corresponded to a gross blowing coefficient, or C_J, as presented in Eq (9). Because the slot height was constant over the span, there was essentially a constant mass flow rate out the slot. All other things being equal, this meant that C_μ varied over the span, inversely proportional to the chord.

These facts were taken into account when a comparison was run using LATJET. The cases involve a simple tapered wing evaluated at three C_J values and an assumed flap setting of 65 deg. Results of the lift data can be seen in Figure 8. Lift coefficient values in the three cases agree well with respect to both slopes and intercepts.

Figure 9 shows the variation in drag coefficients and highlights the typical dilemma the vortex lattice method has with predicting drag. Each curve exhibits a parabolic relationship between lift and drag, but all three LATJET cases are optimistic compared to the wind tunnel results. It should be pointed out though, that the wind tunnel data

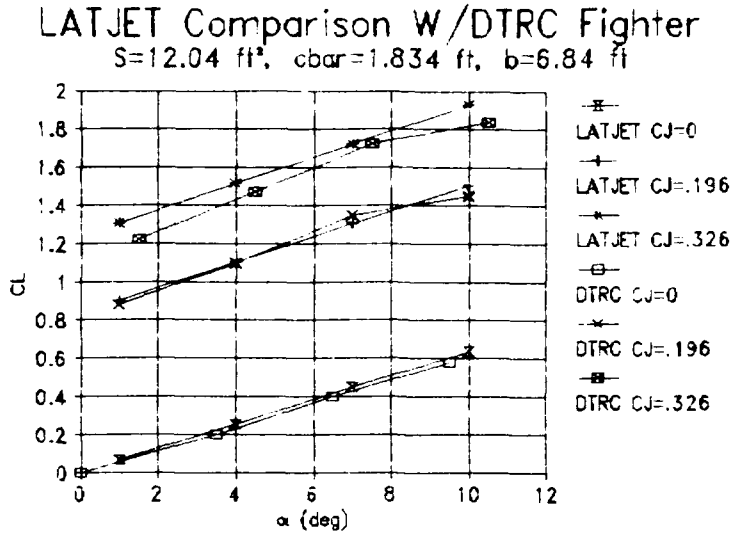

Figure 8 DTRC Fighter Comparison Lift Curves

includes viscous effects whereas the computational data does not.

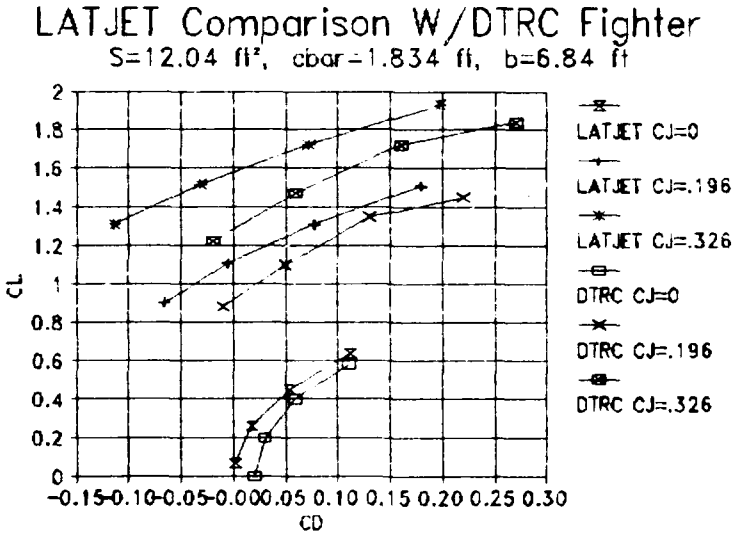

Figure 9 DTRC Fighter Comparison Drag Data

Moment data in Figure 10 also shows similar trends. LATJET data appears to be slightly optimistic by under

predicting the magnitude of the pitching moment. However, the vertical distribution of DTRC data for C_J=0 indicates that the reference position that the moment is calculated about may actually be the aerodynamic center, and not the $\bar{c}/4$ as stated by Hemmerly.

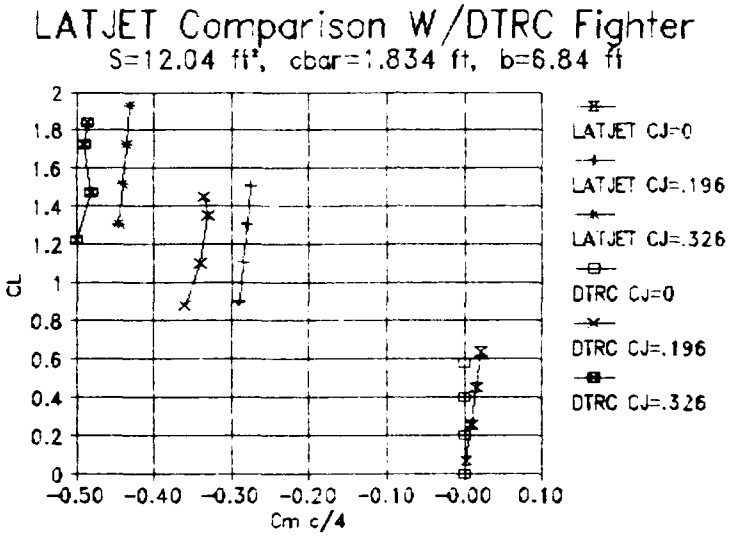

Figure 10 DTRC Fighter Comparison Moment Data

V. Results

All cases were run from input files based on blowing coefficients. In the case of the configuration study, this refers to specific power settings. Each input file included individual cases to account for every combination of α and δ_j.

1 Force Accounting

Before discussing the results themselves, the actual accounting of forces due to both the wing and jet should be explained. The lift coefficient, C_L, as presented here includes both the lift of the wing and the component of jet thrust in the lift direction. In order to present a true powered drag polar, lift effects were not separated. Jet contributions to the lift coefficient can be calculated with the following equation.

$$C_{L_{jet}} = C_J \sin(\alpha + \delta_j) \tag{35}$$

Since the drag is based on forces acting on each of the individual panels, the thrust of the jet must not be accounted for twice. It is popular convention for the designer to account for engine, and/or jet thrust independent from drag. This fact detaches the jet component from the system of aerodynamic forces acting on the aircraft. The induced drag presented here includes a near

field calculation and a component due to the jet, C_{Djet}. C_{Djet} is the result of the jet sheet never really reaching a horizontal position because of some finite value of downwash at ∞. (See Figure 11) This difference between theoretical and realized thrusts is accounted for as a component of drag. In terms of the LATJET output parameters.

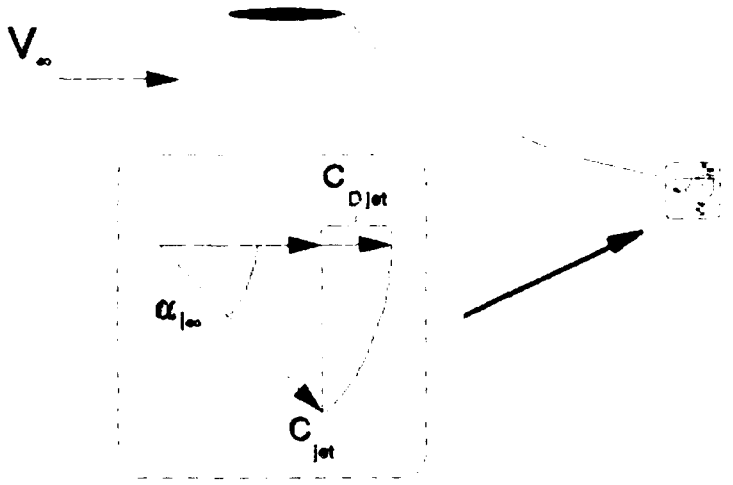

Figure 11 C_{Djet} Schematic

$$C_D = C_{Di} + C_{DJet} + C_{Jet} \qquad (36)$$

With the sharp edged airfoil used on the b.10JF-B, the C_{Di} value used included no leading edge suction. This equates to the situation of a sharp leading edge flap deflected directly into the relative wind. At high blowing coefficients, with increased circulation, the relative wind will have a definite vertical component with respect to the free stream.

Table V lists the reference parameters used in calculating the nondimensional coefficients shown for the b.10JF-B.

Table V b.10JF-B Constant Parameters

S_{ref} (ft^2)	481.5
$\bar{c}$ (ft)	19.36
b (ft)	37.58
x_{cg} (ft)	31.6

2 b.10JF-B Results

Initial calculations showed that C_μ values would fall within 2% of each other for identical power settings at both 10,000 and 20,000 feet of altitude and a Mach number of 0.6. This indicates that for a given power setting, the change in engine gross thrust varies directly with density. Because of the similarity of the coefficients, only the data for 20,000 feet is presented on the curves. The blowing conditions, BC, describe the current power setting and flap arrangement. Jet coefficient values corresponding to each blowing condition appear in Table VI.

2.1 Influence of Blowing Coefficient

Figures 12-17 display edited examples of data found in Appendix B, page 63. They primarily exhibit the effects of blowing coefficient on the various aerodynamic parameters plotted. Blowing conditions 3 and 4 have been removed from

Table VI b.10JF-B Blowing Conditions

BC	Power Setting	C_J	Nozzle Width (in)
0	Unpowered	0	110
1	Mil Power	.1658	110
2	Max AB	.2873	110
3	Mil Power	.1658	36
4	Max AB	.2873	36

the plots to increase clarity.

Figure 13 shows how the blowing coefficient increases the overall lift produced at a given angle of attack. At first, there appears to be no variation in the lift curve slope. Upon closer examination, Figure 12 reveals that $C_{L\alpha}$ actually varies linearly with respect to C_J. It increases approximately 10% over the range of C_J.

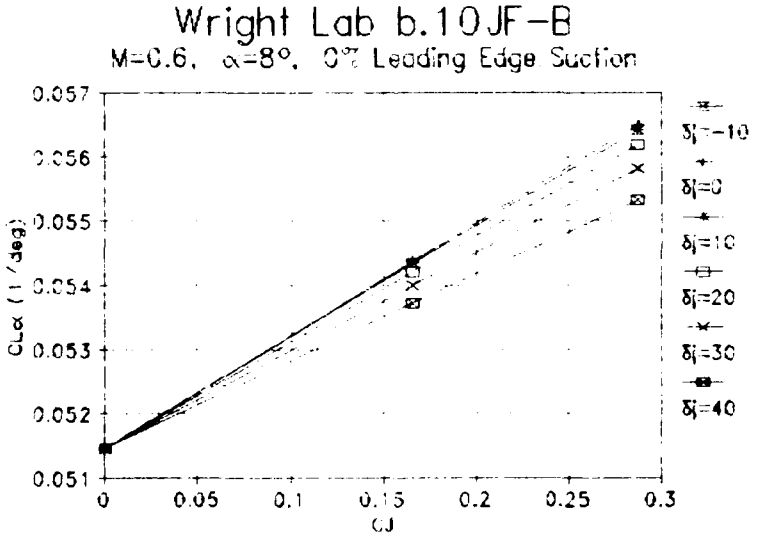

Figure 12 Variation in $C_{L\alpha}$ with Respect to C_J

The variation of $C_{L\delta j}$ with respect to C_J also has a direct influence on lift. Figure 14 shows a non-linear relationship with respect to C_J. Since the study limited

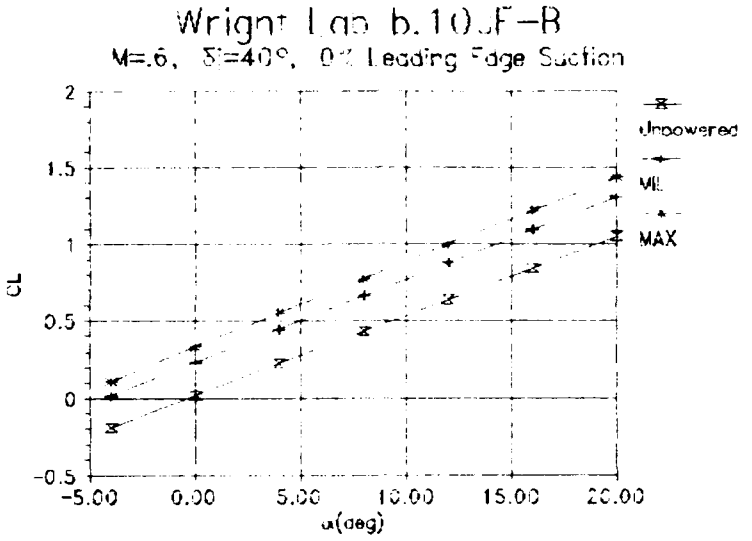

Figure 13 Example b.10JF-B Lift Data, δ_j=40°

itself to investigating blowing coefficients corresponding to only three power settings, the exact relationship is unclear.

The effect of C_J on the pitching moment is similar to its effect on the lift curve. As C_J increases, it shifts the curves downward, Figure 15. The slope of this curve has an important relationship to the static stability of an aircraft. The negative of its value is the static margin of the aircraft.

$$SM = -\frac{C_M}{C_L} \qquad (37)$$

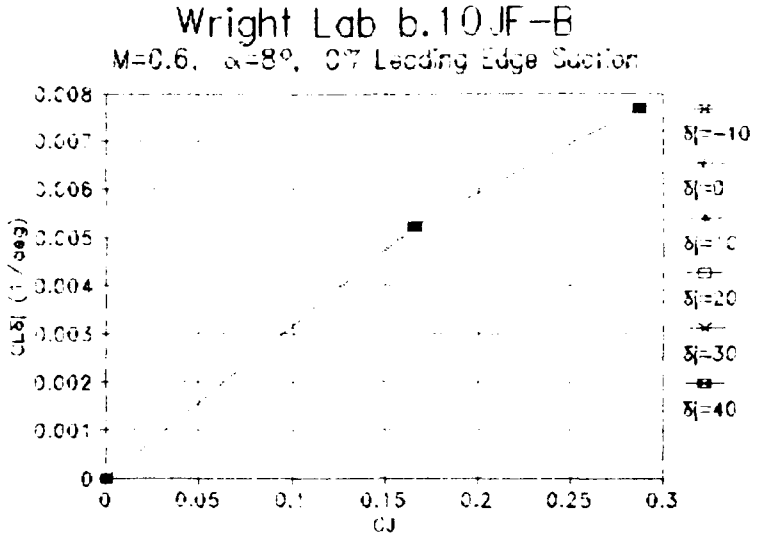

Figure 14 Variation of $C_{L\delta J}$ with Respect to C_J

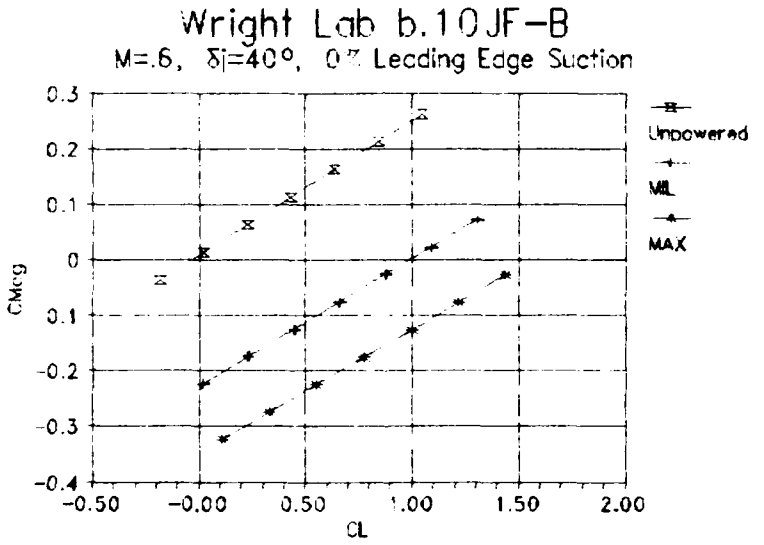

Figure 15 Example b.10JF-B Moment Data, δ_j=40°

Static margin is a convenient term which describes the distance of the CG from the aerodynamic center as a percentage of $\bar{c}$. A negative static margin implies that the aircraft is statically unstable. Figure 15 shows that the static margin for the b.10JF-B lies between -.21 and -.24 as

C_J varies from 0 to .2873. The relationship between SM and C_J is non-linear.

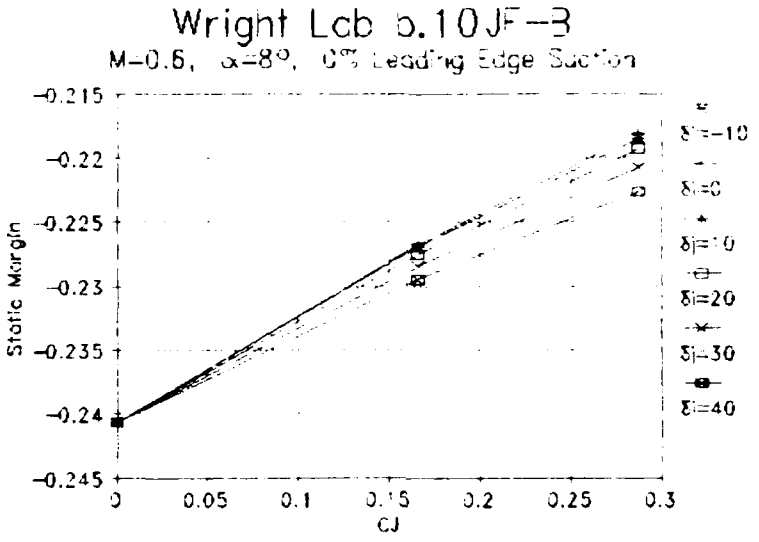

Figure 16 Variation in Static Margin with Respect to C_J

A mechanical flap analogy may explain the increase in static margin as C_J increases. Theoretically, a larger blowing coefficient represents a flap with more area. Since this increase in "area" is downstream of the trailing edge, the aerodynamic center shifts aft. This rearward shift in corresponds to the increasing static margin.

The influence of C_J on induced drag can be seen in Figure 17. When compared to the drag polar for C_J=0, BC=0, the blown cases show induced drag penalties at C_L=0. As α, or C_L, increases, the blown curves begin to cross over the unpowered condition and show a decrease in induced drag. BC=1 crosses over at approximately C_L=0.5 and BC=2 does so at about C_L=.6. This demonstrates that an optimum C_J exists

for a particular flap deflection and lift condition. The induced drag increase at low α is due to the upset of the spanwise lift distribution from the flap deflection.

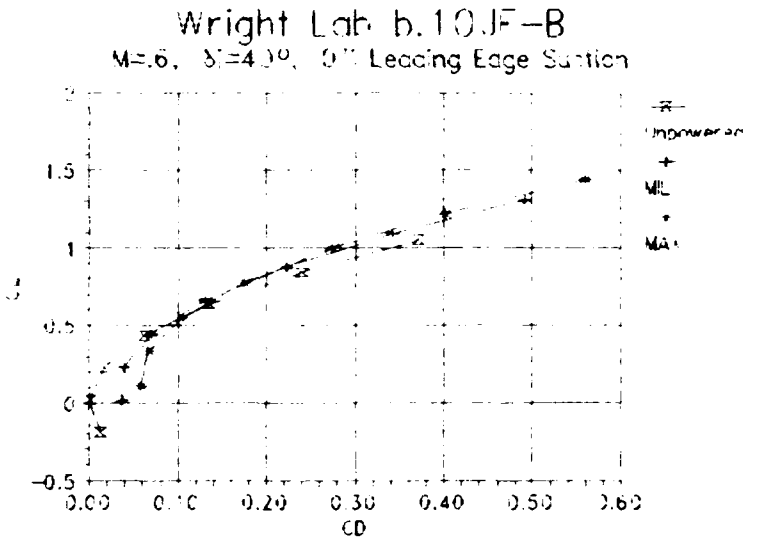

Figure 17 Example b.10JF-B Drag Data, δ_j=40°

2.2 Influence of Flap Deflection

Example effects of flap deflection are presented in Figures 18-22. Each plot illustrates a blowing condition representing maximum afterburning thrust, BC=2. For clarity, flap deflections have been reduced to 0, 20, and 40 degrees.

Effects of δ_j were found to be very similar to those of a mechanical flap. The lift curve in Figure 18, shows a definite lift increment for each level of δ_j with no discernable variation in $C_{L\alpha}$. Looking at $C_{L\alpha}$ values with respect to δ_j in Figure 19, a smoothly varying trend becomes apparent.

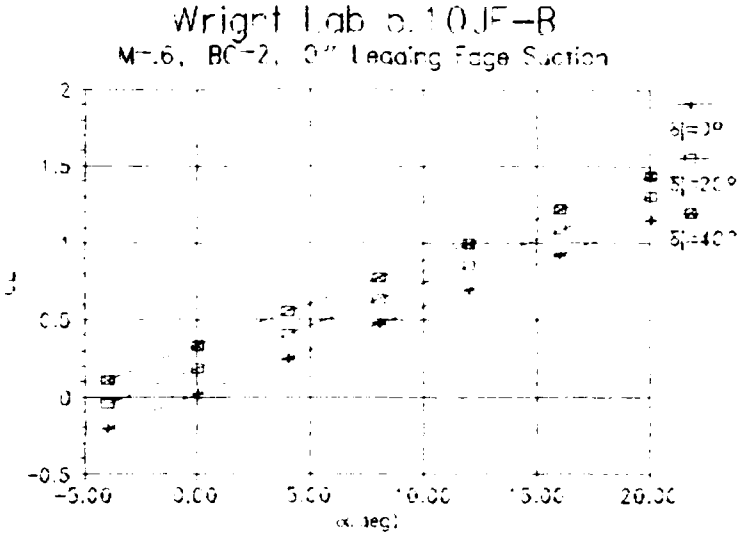

Figure 18 Example b.10JF-B C_L vs δ_j, BC=2

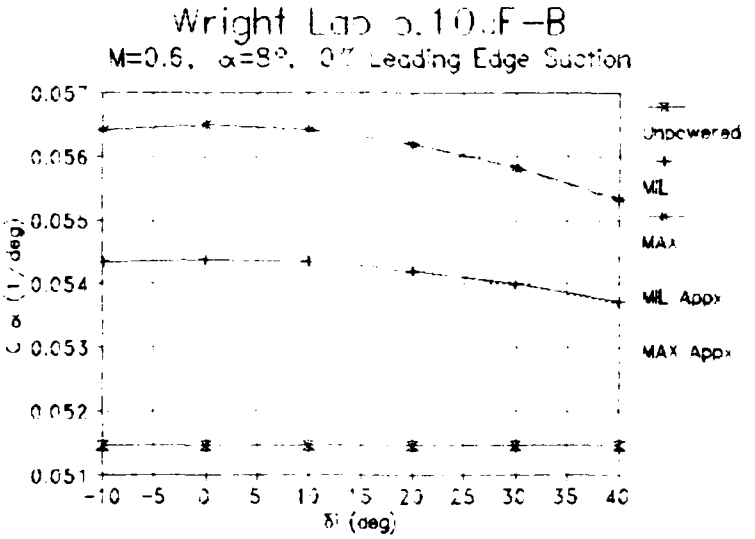

Figure 19 $C_{L\alpha}$ Variation with Respect to δ_j

The curves can be approximated with a cosine relationship.

The rationale for a cosine approximation was that the projected "area" of the jet flap varies with respect to the

$$C_{L_\alpha} = .00292\,COS(\delta_f) + .051463\ [deg^{-1}] \qquad \text{for BC 1}$$

$$C_{L_\alpha} = .00502\,COS(\delta_f) + .051463\ [deg^{-1}] \qquad \text{for BC 2}$$

cosine of the flap deflection. In Figure 19 the approximations overlap the actual values almost exactly.

Induced drag in Figure 20 is minimized at δ_f=0 and α=0, but there is a cross over phenomenon similar to the one seen in Figure 17. Knowledge of this is very beneficial since an aircraft will generally be flying at a fixed power setting and weight which would correspond to C_J and C_L respectively. The optimized flap setting appear to reduce the induced drag by approximately 10%.

The drag reduction may be short lived. This reduction comes with the corresponding increase in nose down pitching

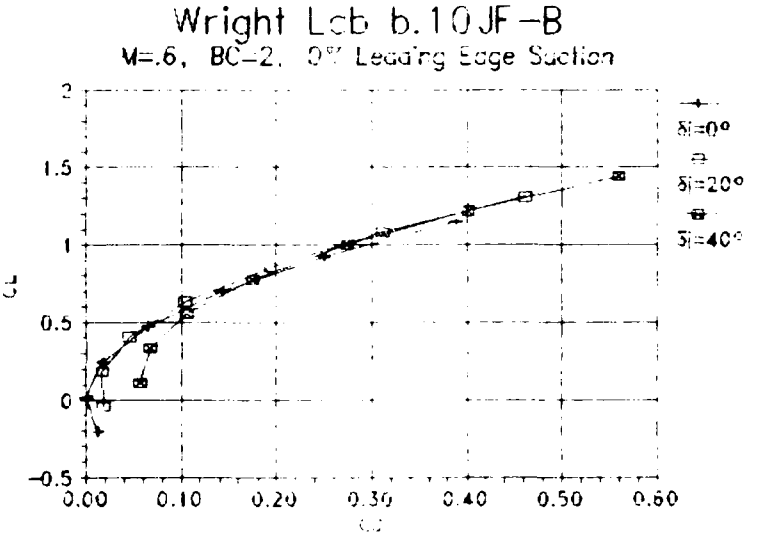

Figure 20 Example b.10JF-B Drag Data, BC=2

moment, Figure 21. The control surface drag required to trim the moment to zero may be prohibitive. Again, like the lift data, there is a cosine variation in SM with respect to

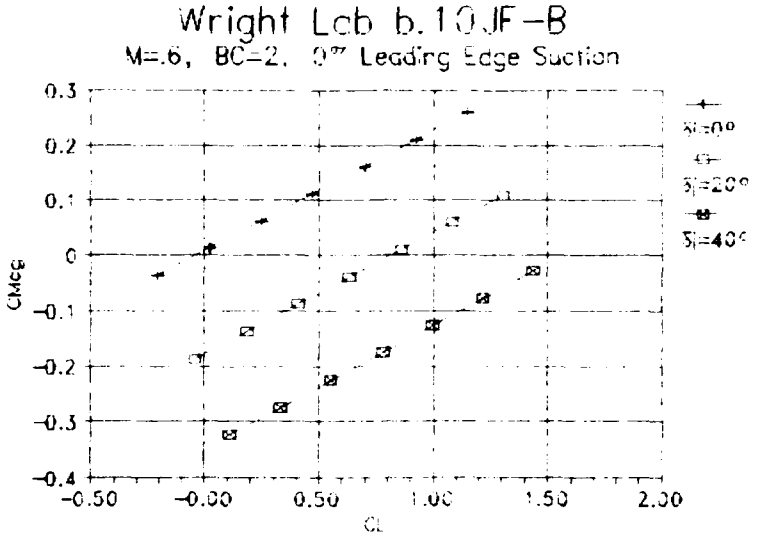

Figure 21 Example b.10JF-B Moment Data, BC=2

δ_j in Figure 22. The approximations are

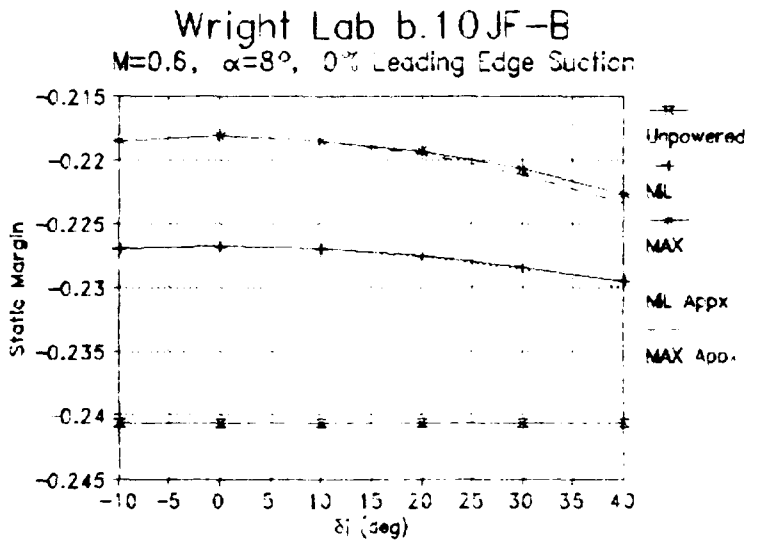

Figure 22 Variation in Static Margin with Respect to δ_i

$$SM = .01384\,COS(\delta_j) - .24063 \quad [deg^{-1}] \qquad \text{for BC 1}$$

$$SM = .02250\,COS(\delta_j) - .24063 \quad [deg^{-1}] \qquad \text{for BC 2}$$

These values do not match quite as well at high flap

2.3 Influence of Nozzle Width

Figure 23 shows a lift curve with varying nozzle width. Both cases have the same value for C_j, 0.2873. However, the narrow nozzle has a much larger value for C_μ across its

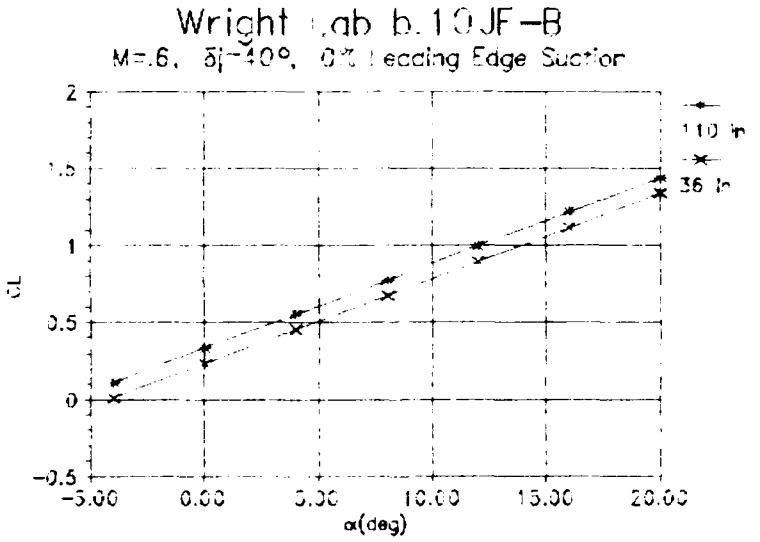

Figure 23 Example b.10JF-B Nozzle Width Comparison, Lift

center panels. With equal mass flow rates, the narrow nozzle must have a larger value of m_j. There is no variation in slope. The increase in lift of the wider nozzle is the result of it acting on a much larger area of the wing.

Figure 24 indicates a small induced drag increase due to the narrow nozzle. The overall shape of the polar is the same, and the is no cross over tendency.

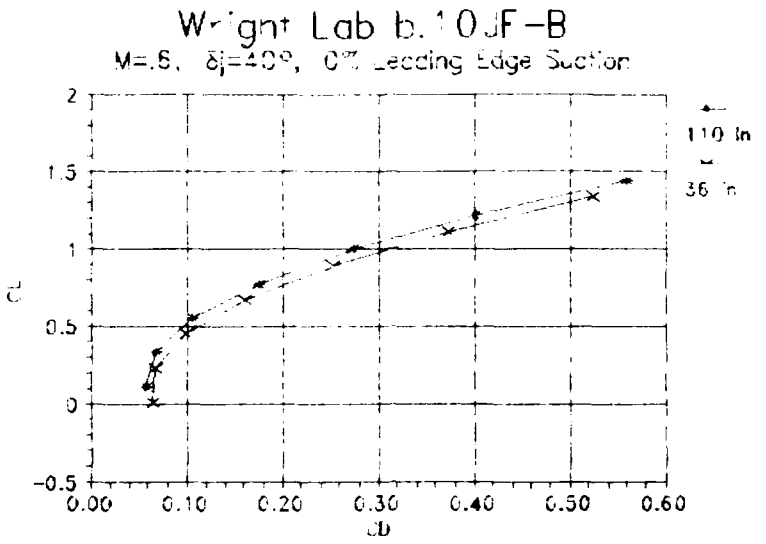

Figure 24 Example b.10JF-B Nozzle Width Comparison, Drag

Pitching moments created by the narrow nozzle, Figure 25, are less severe.

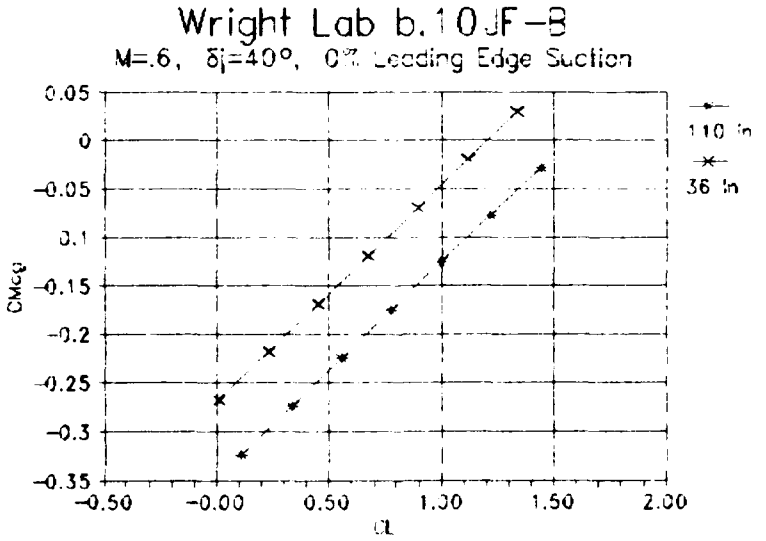

Figure 25 Example b.10JF-B Nozzle Width Comparison, Moment

One assumption which needs to be addressed is jet thickness. As the jet width was reduced to 36 inches, the thickness increased to maintain a constant exit area. This case is presented as an example only. Any conclusions drawn from it must be regarded skeptically. Reference 12 presents a method for dealing with thick jets.

All curves in Appendix B, except for the drag polars, show linear trends due to the absence of viscous effects. The CL vs α curves shows linear data up to and including α=20 deg. This does not necessarily mean that this is an achievable, unstalled angle of attack, especially in the linear portion of the curve. C_{Lmax} and α_{CLmax} values determined empirically will have to be faired in to the curves.

3 Stability and Control Results

Removal of the destabilizing canard changed the static margin to a positive value of approximately .02, Figure 26. This indicates aft movement of the aerodynamic center. The blown cases still show strong nose down moments which will have to be trimmed somehow. Moment variation due to C_J and δ_j is similar to the full configuration. Given the pitching moment without the canard, the size of the actual control surface can be calculated so that it produces an adequate level of control. Appendix C, page 86, contains the full

set of moment graphs pertaining to the stability and control investigation.

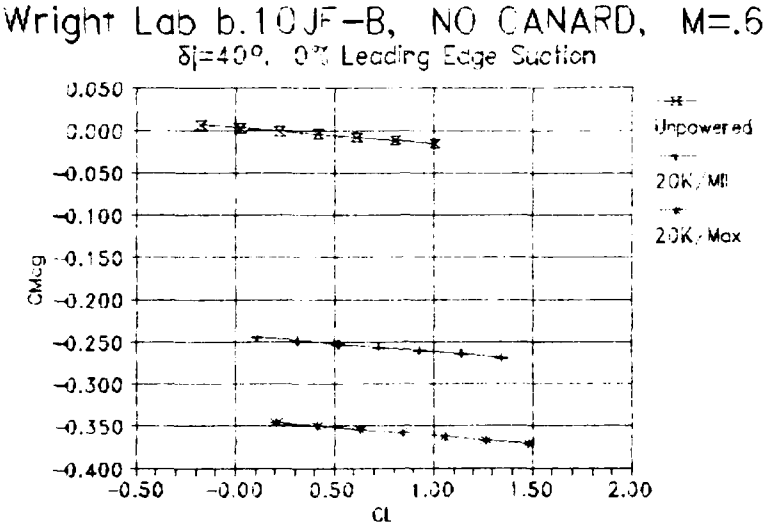

Figure 26 Example b.10JF-B With Canard Removed, Moment

4 Planform Study Results

Wing planform data can be found in Appendix D, page 92. Cases were run for each planform with variation of C_J and δ_j about nominal values of 0.2 and 15 deg respectively. With respect to δj, and C_J, the generic wing planforms behaved like the aircraft configuration. Similar trends were seen in all graphs.

Since the primary purpose of this part of the study was to provide additional data to the designer on a variation in wing planform, the influence of AR and λ characterized in the following example figures.

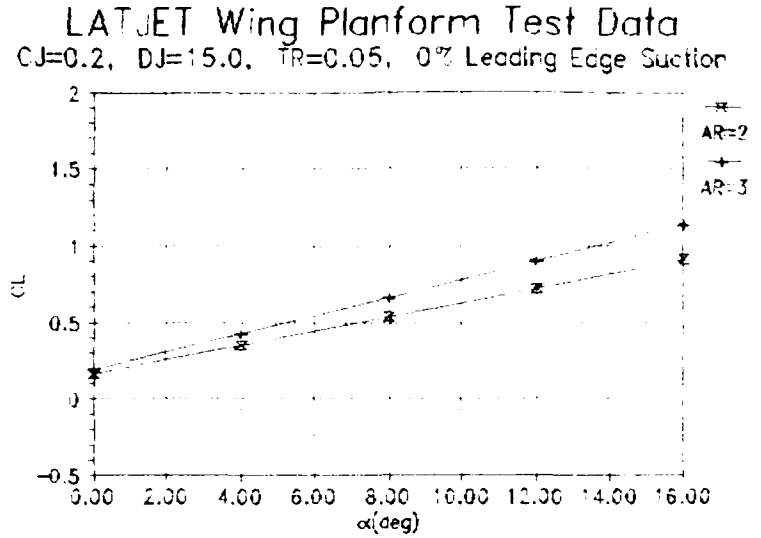

Figure 27 Lift Curve Variation with Respect to AR

As the planform parameters, AR and λ, varied, results typical of conventional wings occurred. Increasing AR raised the slope of the lift curve, Figure 27, and relaxed the drag polar, Figure 28.

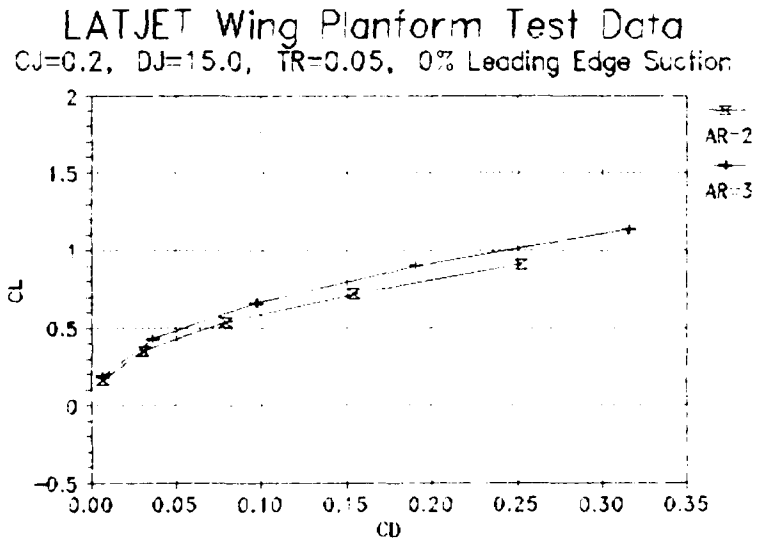

Figure 28 Drag Polar Variation with Respect to AR

The moment curve, Figure 29, shifted downwards and became steeper. This steeper, negative slope would have indicated an increase in the static margin had the moment been taken about a known or predicted CG instead of the planform quarter chord.

Variation in λ showed little influence over the curves. There was essentially no change in the lift curve,

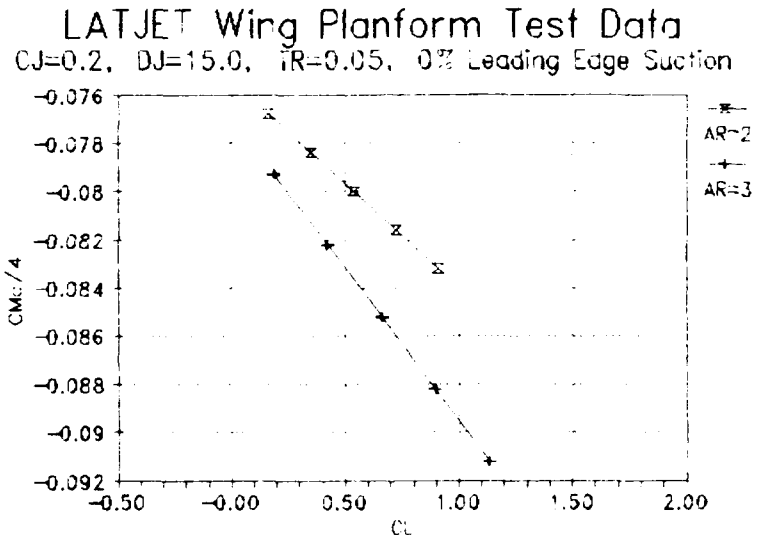

Figure 29 Moment Variation with Respect to AR

Figure 30. The drag polar, Figure 31, also shows insignificant changes. There was however, an appreciable change in the pitching moment. Figure 32 shows the moment shifting downwards with the increase in λ.

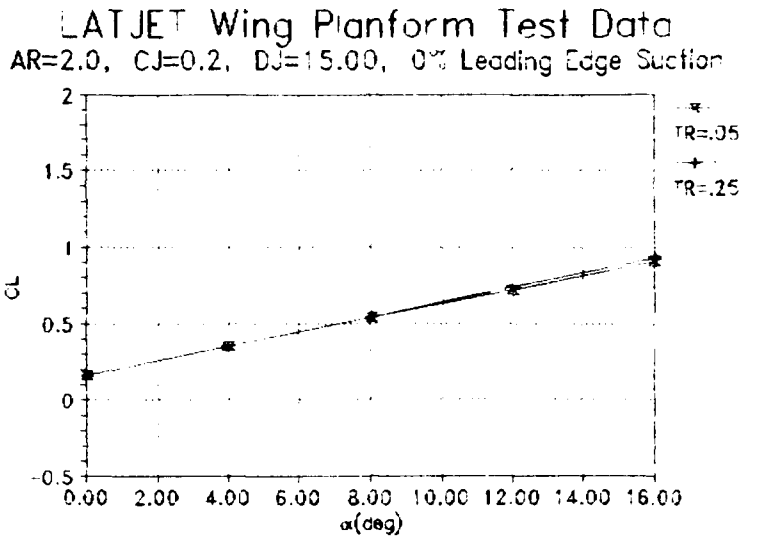

Figure 30 Variation of Lift with Respect to λ

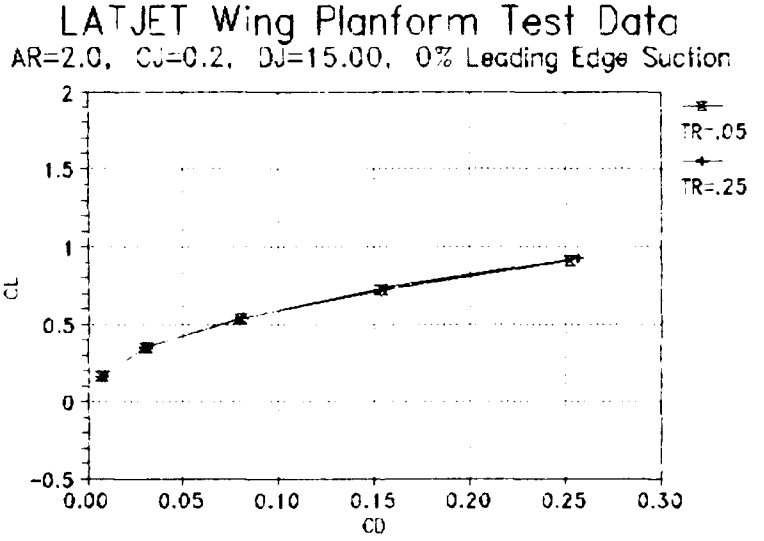

Figure 31 Variation in Drag with Respect to λ

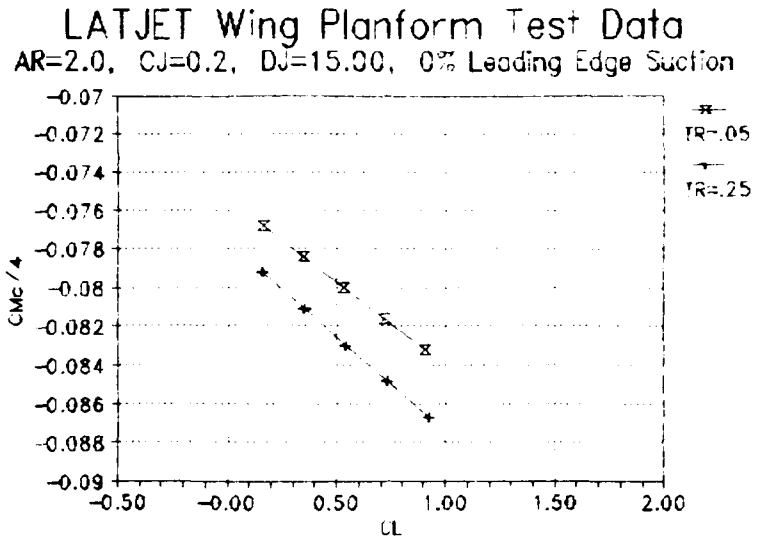

Figure 32 Moment Variation with Respect to λ

VI. Conclusions and Recommendations

The results of this study have shown unequivocal influence of the high aspect ratio nozzles on the aerodynamic characteristics of the Wright Lab b.10JF-B fighter configuration.

Raising the blowing coefficient showed positive shifts in the lift curve and increases in $C_{L\alpha}$. Pitching moments moved in the nose down direction and the static margin increased. The drag polars showed that induced drag increases at low C_L due to the disruption of the smooth spanwise lift distribution. As C_L increased, the drag penalty disappeared, and the curves crossed over the unblown case, exhibiting an induced drag reduction.

Variation of both the lift and moment curves with respect to δ_j was very similar to the C_J cases. However, the slopes of both curves varied with respect to the cosine of δ_j. The drag polar also behaved similarly with regarding δ_j. An induced drag penalty at low C_L transitions to a benefit at high C_L as the curve for a specific δ_j crosses over the undeflected case. This suggests that an optimal flap setting exists for a given blowing condition and lift condition. These conditions correspond to the power setting and weight of the aircraft respectively.

Removal of the canard for the stability and control study resulted in a larger, positive static margin, and indicated a rearward shift in the aerodynamic center.

All in all, the impact on the design can be summed up in the following points. The nozzle shows induced drag reduction at fixed power setting and optimum flap deflection. Drag reduction will be minimal at the partial power settings typical to cruise (Low C_J) and the relatively low C_L values required. Trim drag as the result of countering the extreme pitching moment may overwhelm any drag reduction realized.

The true benefits of the jet flap lie in the high lift region. This makes it most suitable for reducing take-off and landing distance and increasing sustained and instantaneous turn performance. However, this all hinges upon developing an effective way to counter the extreme pitching moments.

Other aspects not included in this study must be accounted for prior to making any final decisions on design feasibility. Potentially, the high aspect ratio nozzle can reduce separation over the aft end. It may also cut down on the infra red signature of the exhaust plume. Nevertheless, production cost, weight and/or complexity may be prohibitive. The only complete answer will be the result of of a full blown multi-variate optimization study.

Bibliography

1. Abbott, I. H. and A. E. Von Doenhoff. Theory of Wing Sections. New York: Dover Publications, 1958, pp 558-559.

2. Kohlman, David L. Introduction to V/STOL Airplanes. Ames, Iowa: University of Iowa Press, 1981.

3. Bertin, John J. and Micheal L. Smith. Aerodynamics for Engineers. Englewood Cliffs, New Jersey: Prentice-Hall, Inc., 1979.

4. Bonner, E., W. Clever, and K. Dunn. "Aerodynamic Preliminary Analysis System, Part I Theory." Contract NAS1-14686, Los Angeles: Rockwell International Corporation, April 1978, (NASA Contractor Report 145284).

5. Crawford, Donald R. Airplane Design. Torrance, California: Crawford Aviation, 1986.

6. Engler, Robert J. and Robert M. Williams. "Design of a Circulation Control Stern Plane for Submarine Applications." Bethesda, Maryland: Naval Ship Research and Development Center, March 1971, (AD-901 198)

7. Ferraro, Drew T. "Users Guide for the Vortex-Lattice Camber Inputs." Unpublished report, ASD/XRH, August 1984.

8. Fredette, Raymond. Unpublished notes, 1991

9. Hemmerly, Rodney A. "Subsonic Investigation of a Semispan Jet Flapped Wing Designed Primarily for High Speed Flight." Bethesda, Maryland: David W. Taylor Naval Ship Research and Development Center, June 1975 (AD-A024 798).

10. Hough, Gary R. "Lattice Arrangement for Rapid Convergence." Vortex Lattice Utilization. NASA SP-405, 325-342, Washington D.C.: National Aeronautics ans Space Administration, 1976.

11. ----- "Remarks on Vortex-Lattice Methods." J. Aircraft, Vol. 10, No. 5, 1973, pp 314-317, (May 1973).

12. Lan, Edward C. and James F. Campbell. "Theoretical Aerodynamics of Upper-Surface-Blowing Jet-Wing

Interactions. Washington D.C.: National Aeronautics and Space Administration, Nov 1975, (NASA TN D-7936).

13. Lopez, M. L. and C. C. Shen. "Recent Developments in Jet Flapped Theory and Application to STOL Aerodynamic Analysis." 4th Fluid and Plasma Dynamics Conference, Paper No. 71-578. New York: American Institute of Aeronautics and Astronautics, July 1971.

14. McCormick, Barnes W., Jr. Aerodynamics of V/STOL Flight. Orlando, Florida: Academic Press, Inc., 1967.

15. Mondey, David, Ed. The International Encyclopedia of Aviation. New York: Crown Publishers, Inc., 1977.

16. Richardson, Doug. Stealth. New York: Crown Publishers, Inc., 1989, pp 50-51.

17. Spence, D. A. "The Lift Coefficient of a Thin Jet Flapped Wing." Process Royal Society, A238, 46-68, 1956.

18. Snyder, James R. LATJET Vortex Lattice Computer Code. May 1991.

19. ----- Unpublished Notes, 1991.

Appendix A: Philosophy of Designer

The Wright Laboratory Configuration b.10JF-B is a baseline layout for a future multi-role fighter design possibility. This single place, single engine concept incorporates a high aspect ratio jet flap type nozzle at the base of a wide, flat body. The design philosophy employed here is that the jet flap may upgrade the trimmed drag polars of low aspect ratio wings to the extent that its additional propulsion and integration weights can be offset by the reduced structural weight of the wings, canard and tails for a net reduction in weight empty, which will thereby improve the fuel load. The viability of this approach resides in the amount of aerodynamic improvement that can be derived from jet flap effects.

Inspection of the 2 view drawing of the b.10JF-B layout, Figure 1, and data sheet shows a design combining very high thrust and moderate wing loading. Highly favorable effects may make it possible to reduce both engine size and wing area in the interest of increasing fuel fraction. If the benefits allow changes in maneuvering wing loading to the region of 80 psf and a thrust-to-weight ratio of approximately 1.5, then the fuel fraction of a 30,000 lb fighter could be boosted 35% above the baseline case typified by the b.10JF-B.

Table VII b.10JF-B Dimensions and Weight

Takeoff Gross Weight(lbs)	30,000
Thrust to Weight Ratio	1.7066
Wing Loading, takeoff (psf)	62.35
Wing Loading, maneuver (psf)	57.00
Overall Length (ft)	60.625
Span (ft)	31.573
Maximum Body Width (ft) at FS 654.281	14.543
Body Width at c/2 wing (ft) at FS 557.292	13.413
Body Depth at FS 375 (ft)	5.333
Overall Height, gear up (ft)	10.167
Nominal C.G. at FS 451	

Raymond Fredette
Senior Design Engineer
WL/XPAD

Appendix B: b.10JF-B Aerodynamic Data

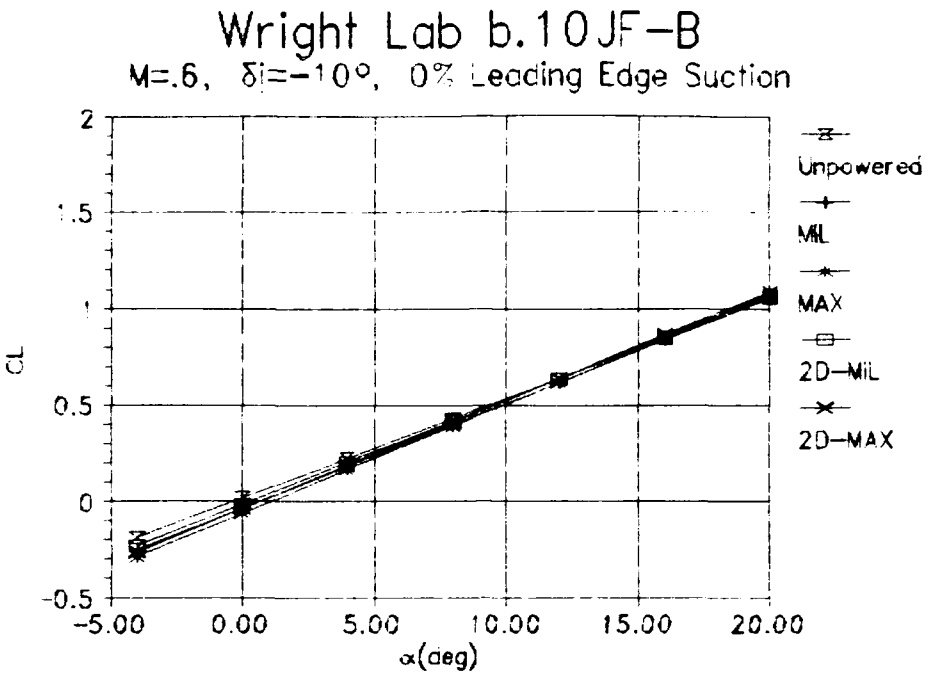

Figure 33 Lift Curve for δ_j=-10°

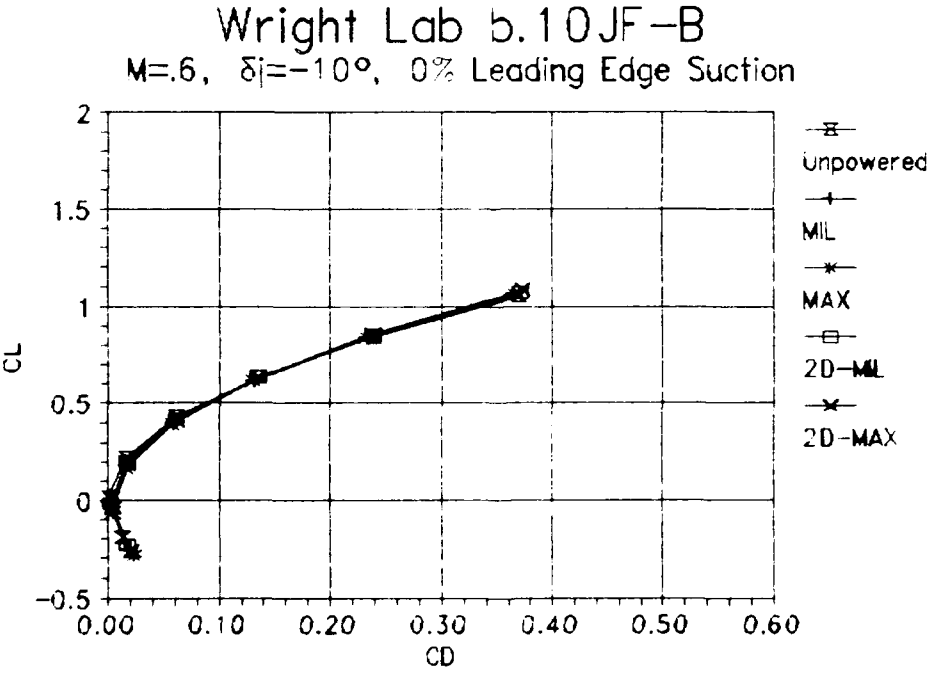

Figure 34 Drag Polar for δ_j=-10°

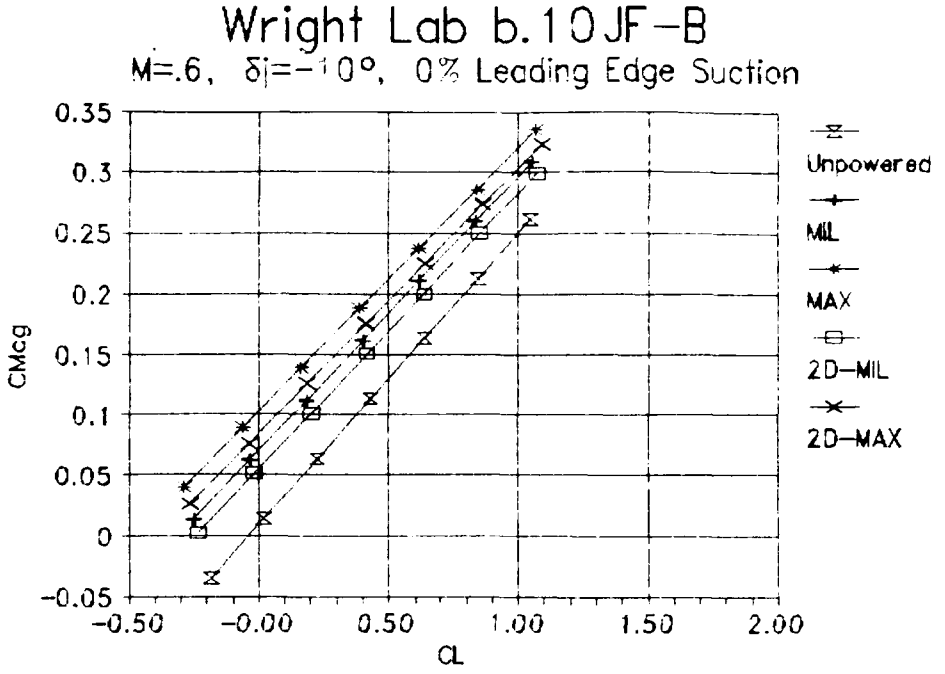

Figure 35 Pitching Moment About the CG for δ_j=-10°

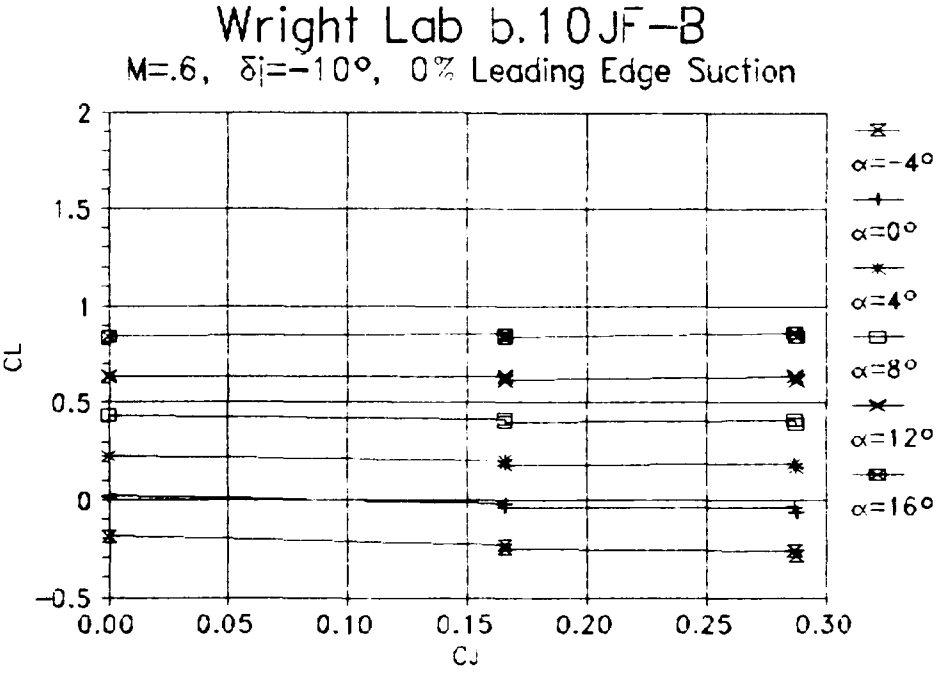

Figure 36 Lift Variation Due to C_J for δ_j=-10°

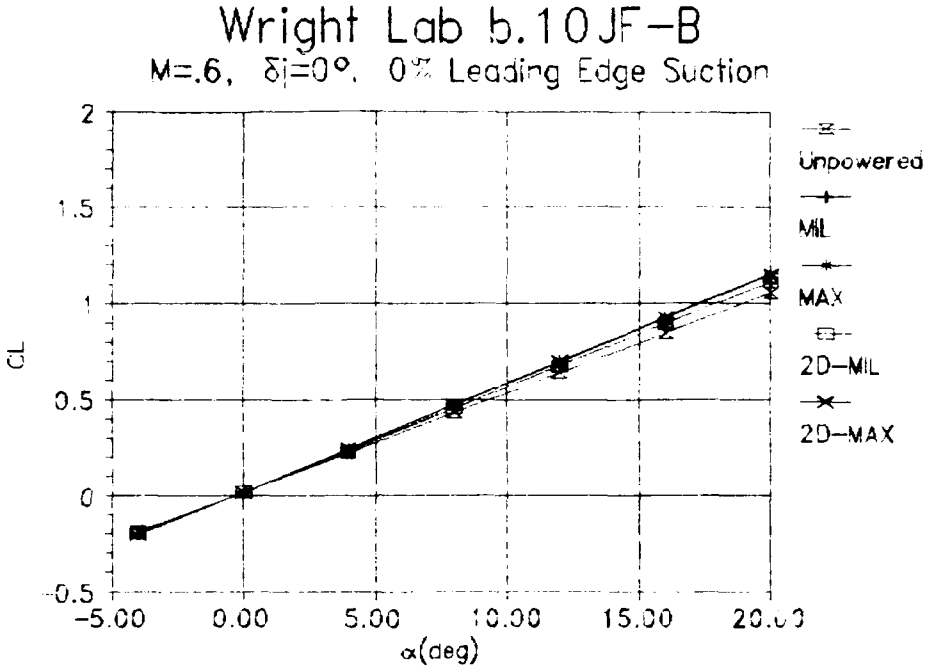

Figure 37 Lift Curve for δ_j=0°

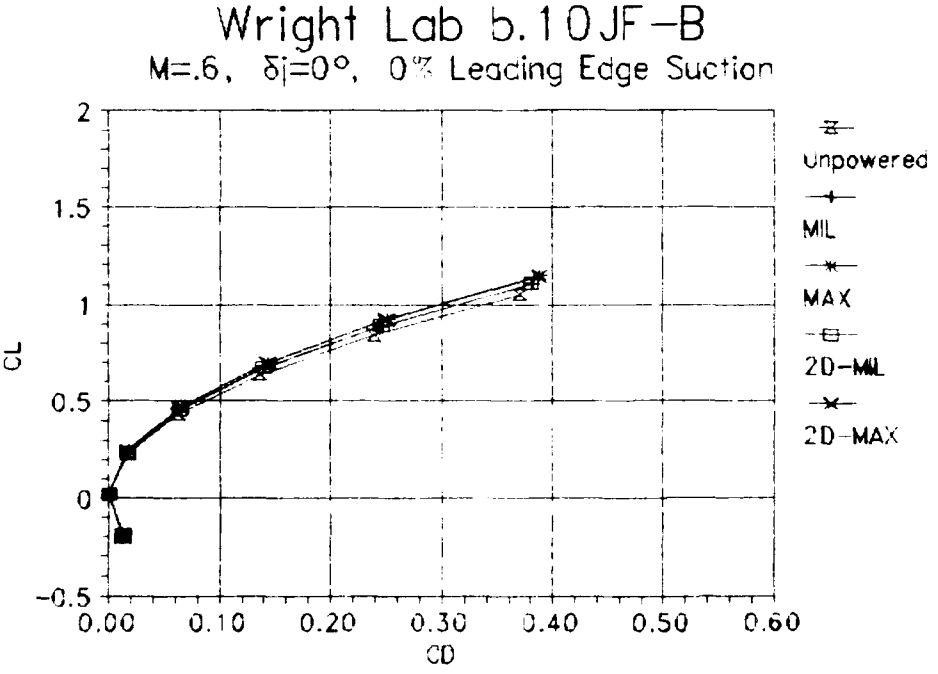

Figure 38 Drag Polar for δ_j=0°

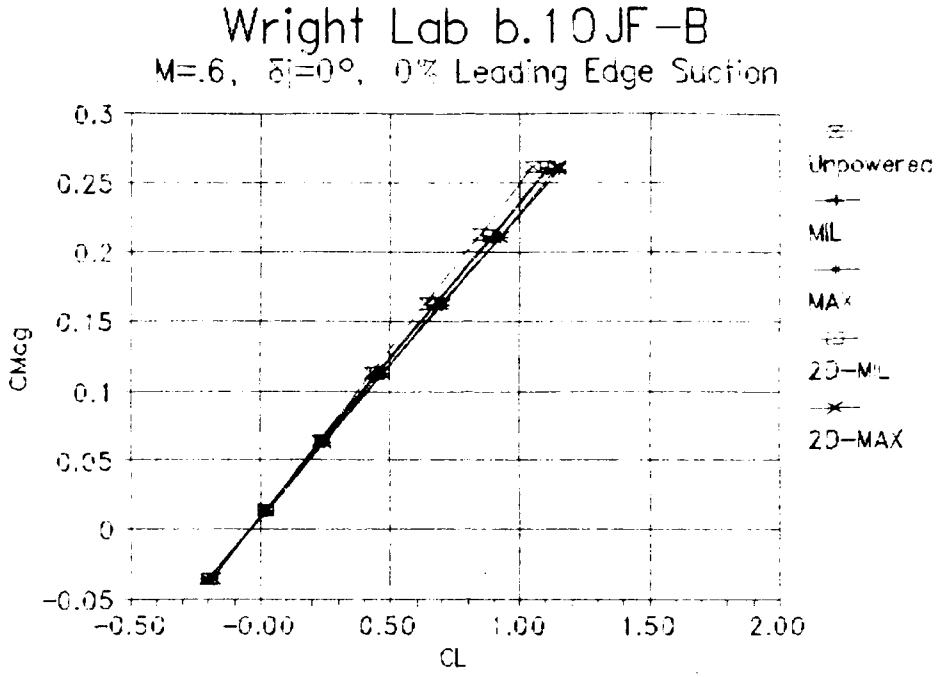

Figure 39 Pitching Moment About the CG for δ_j=0°

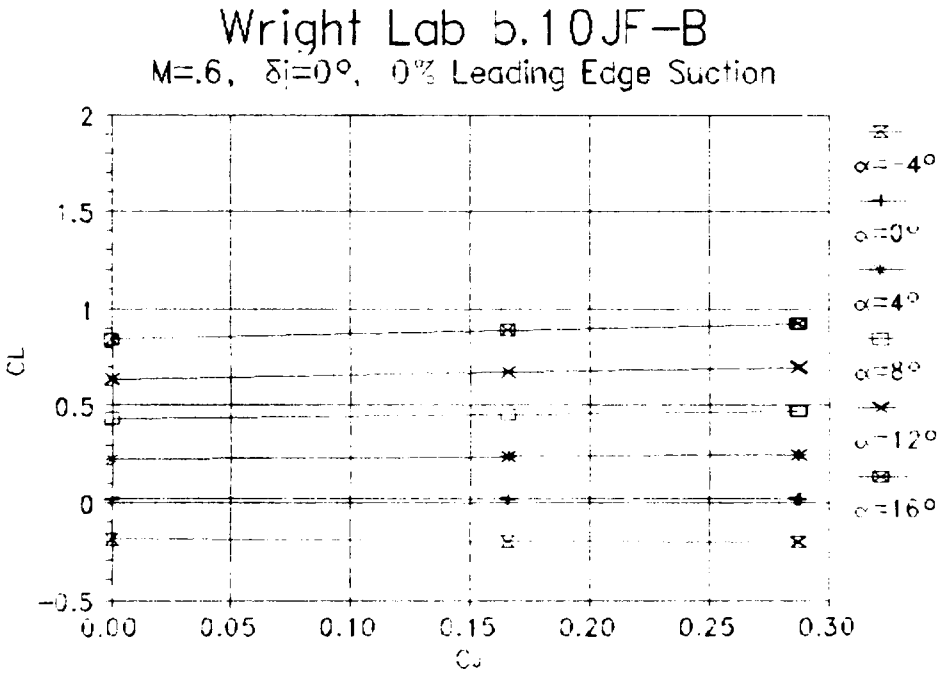

Figure 40 Lift Variation Due to C_μ for δ_j=0°

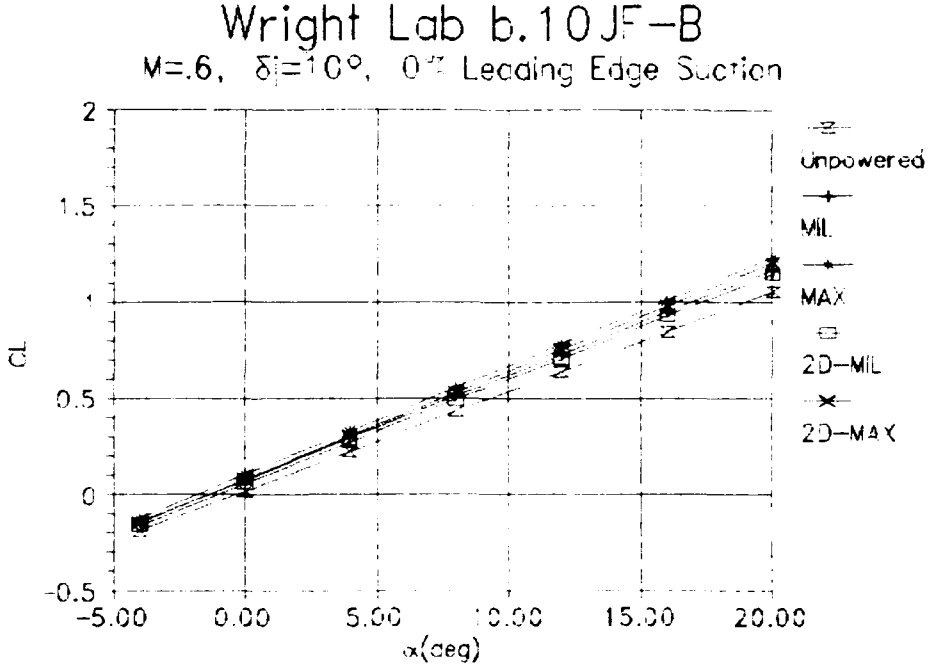

Figure 41 Lift Curve for δ_j=10°

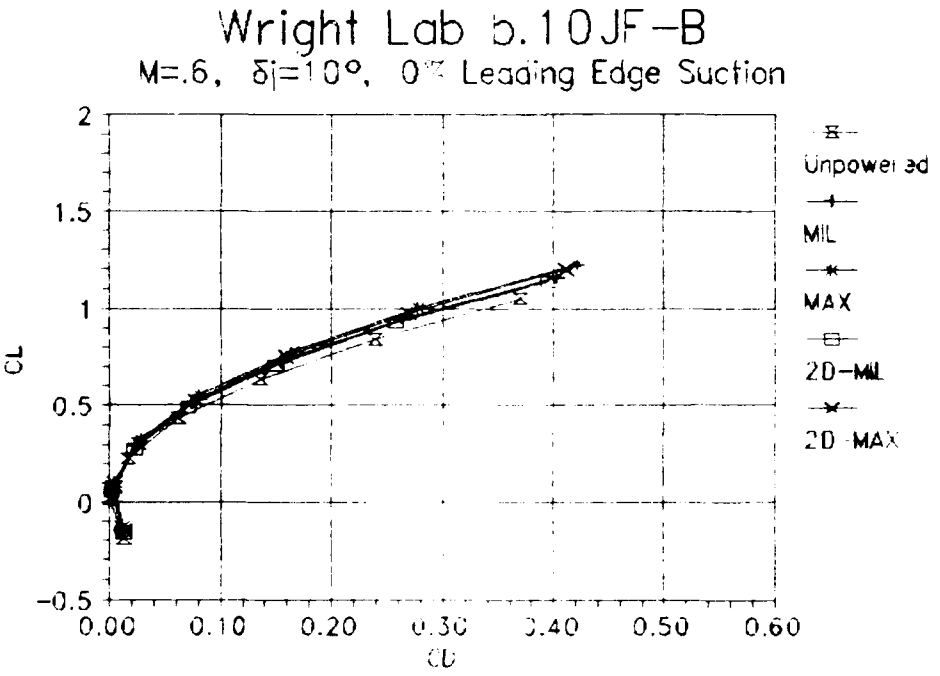

Figure 42 Drag Polar for δ_j=10°

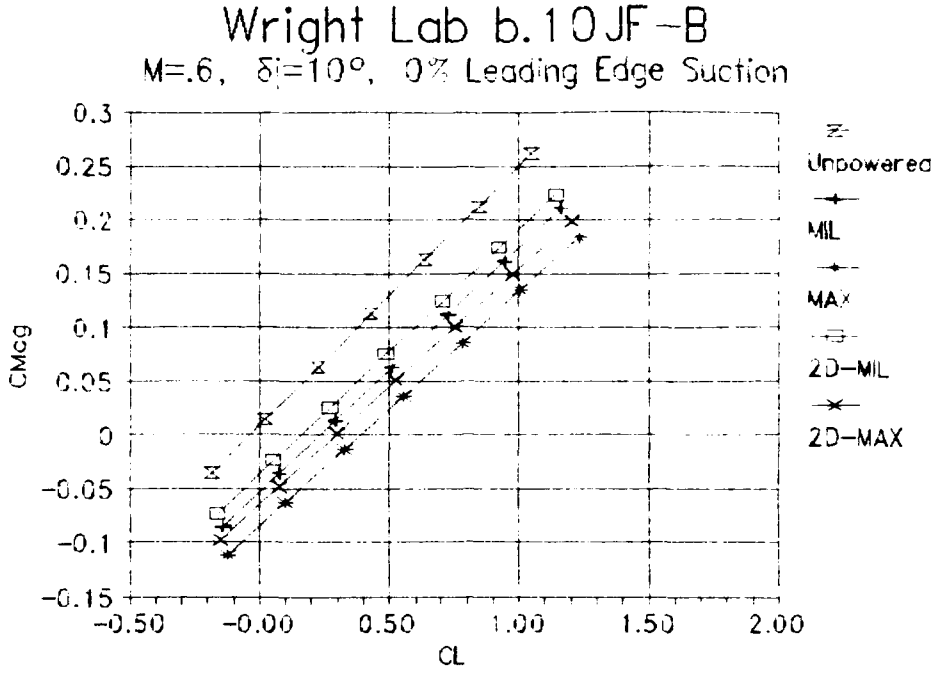

Figure 43 Pitching Moment About the CG for δ_j=10°

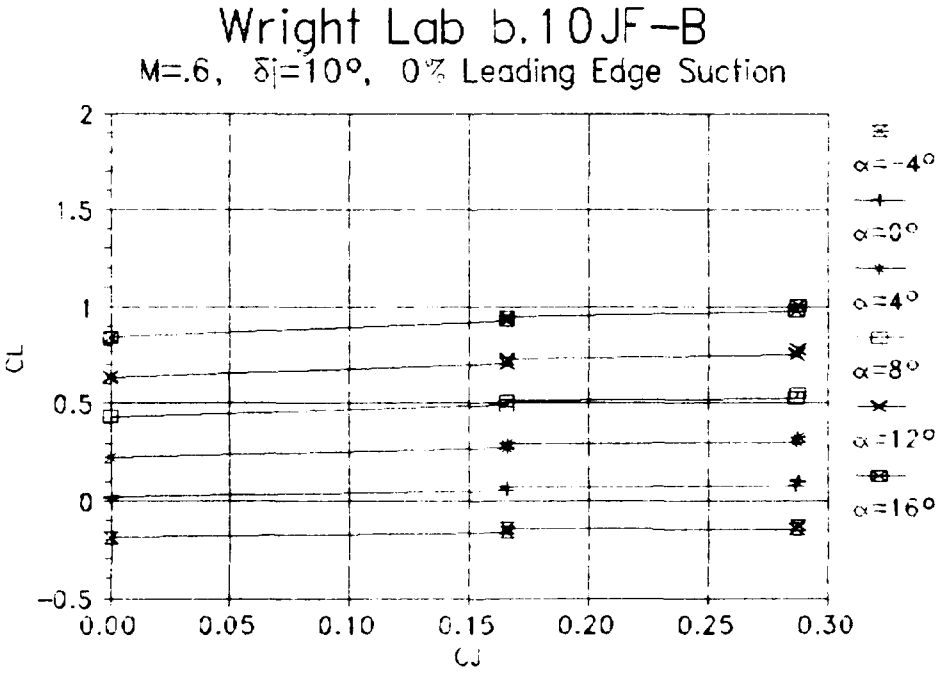

Figure 44 Lift Variation Due to C_J for δ_j=10°

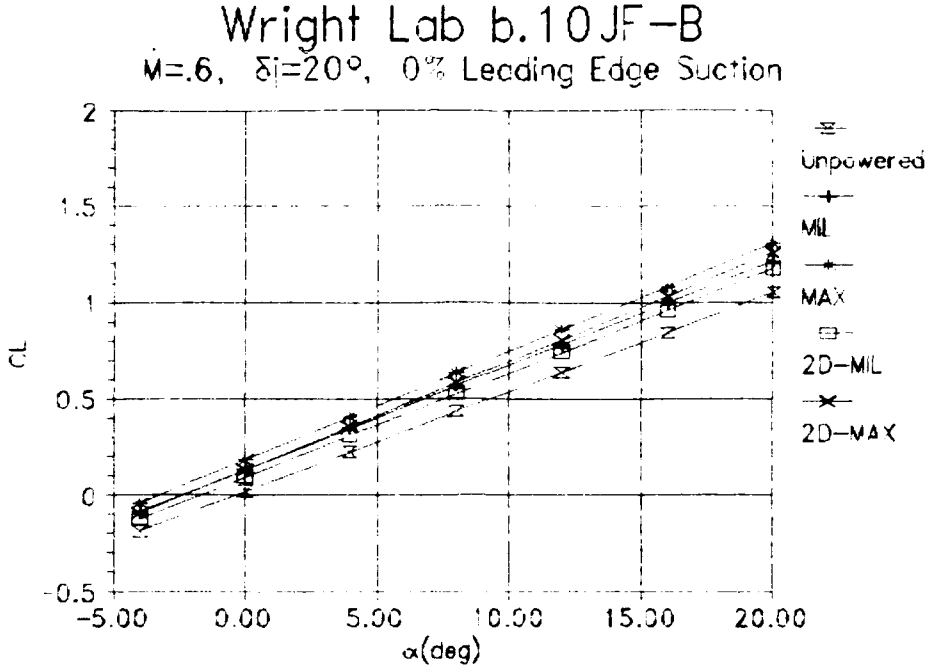

Figure 45 Lift Curve for δ_j=20°

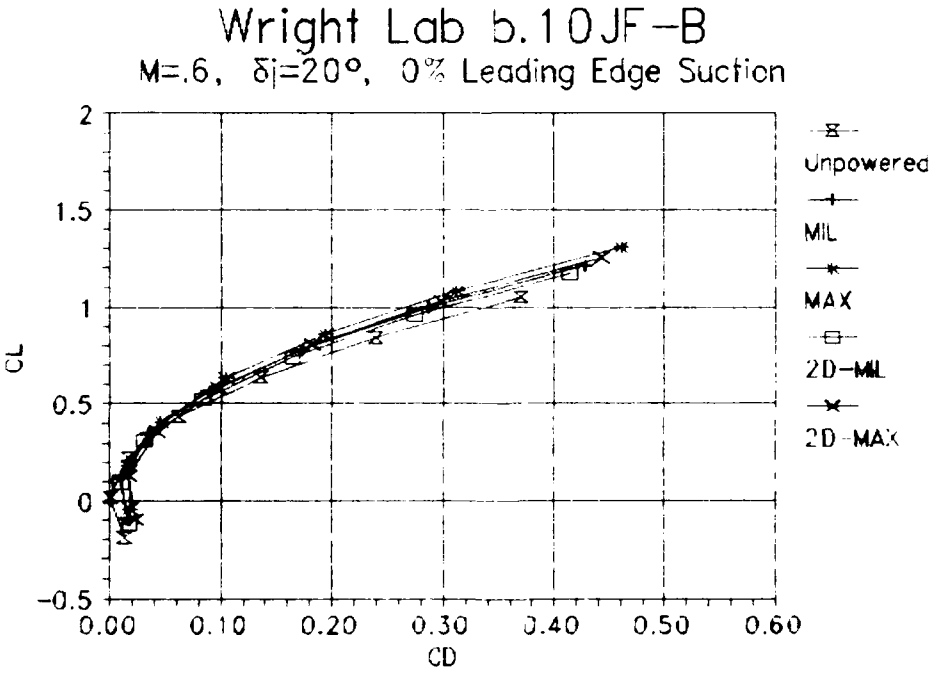

Figure 46 Drag Polar for δ_j=20°

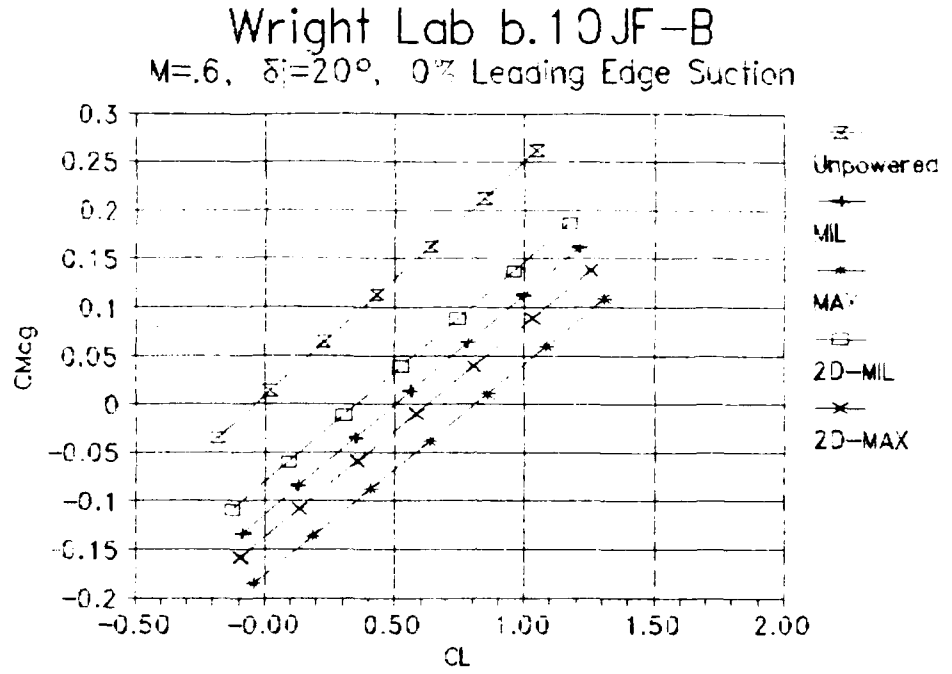

Figure 47 Pitching Moment About the CG for δ_j=20°

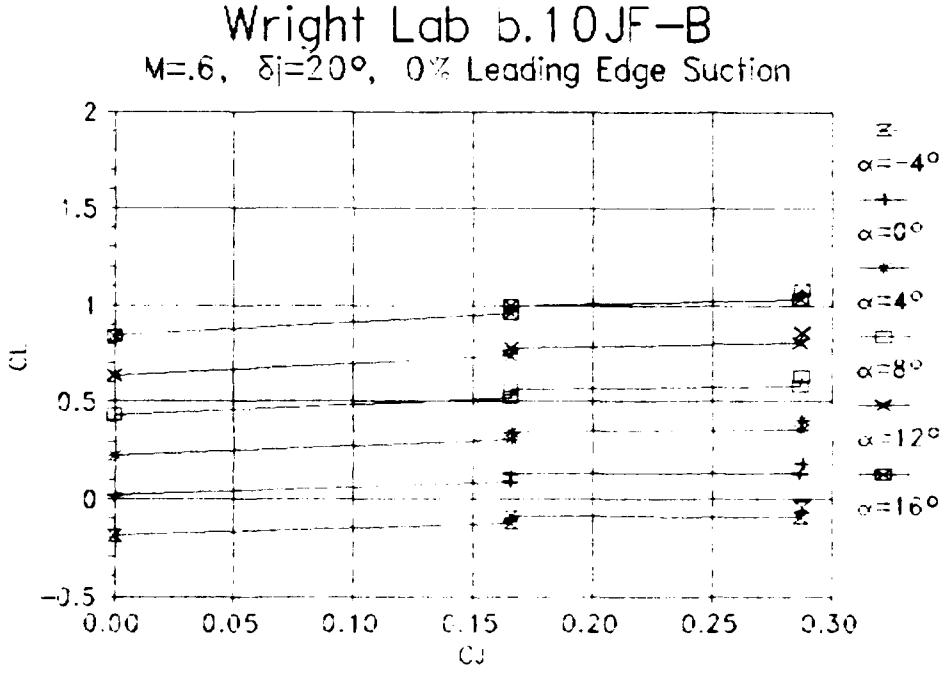

Figure 48 Lift Variation Due to C_J for δ_j=20°

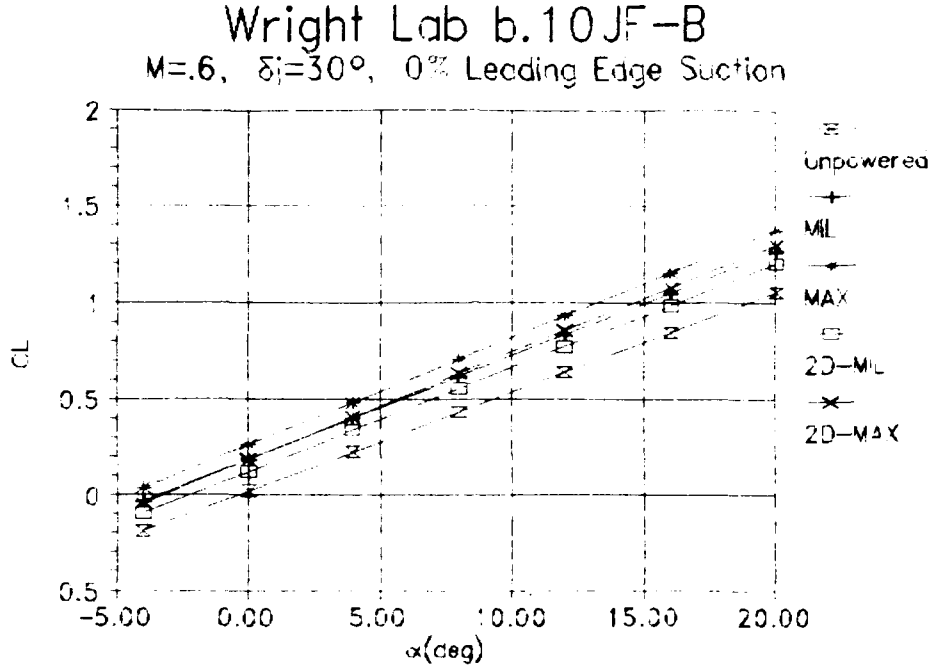

Figure 49 Lift Curve for δ_j=30°

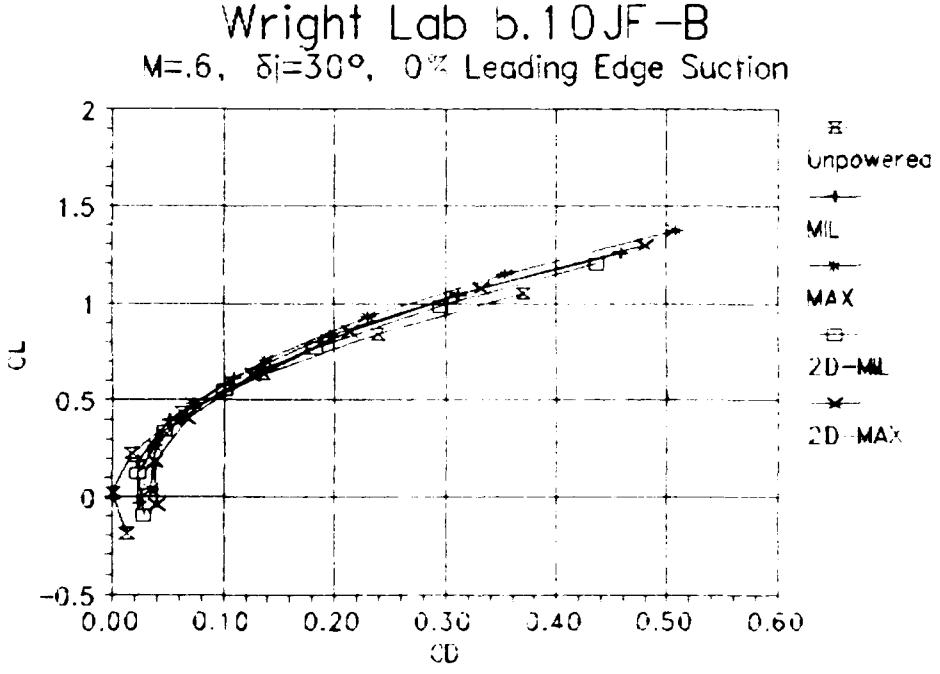

Figure 50 Drag Polar for δ_j=30°

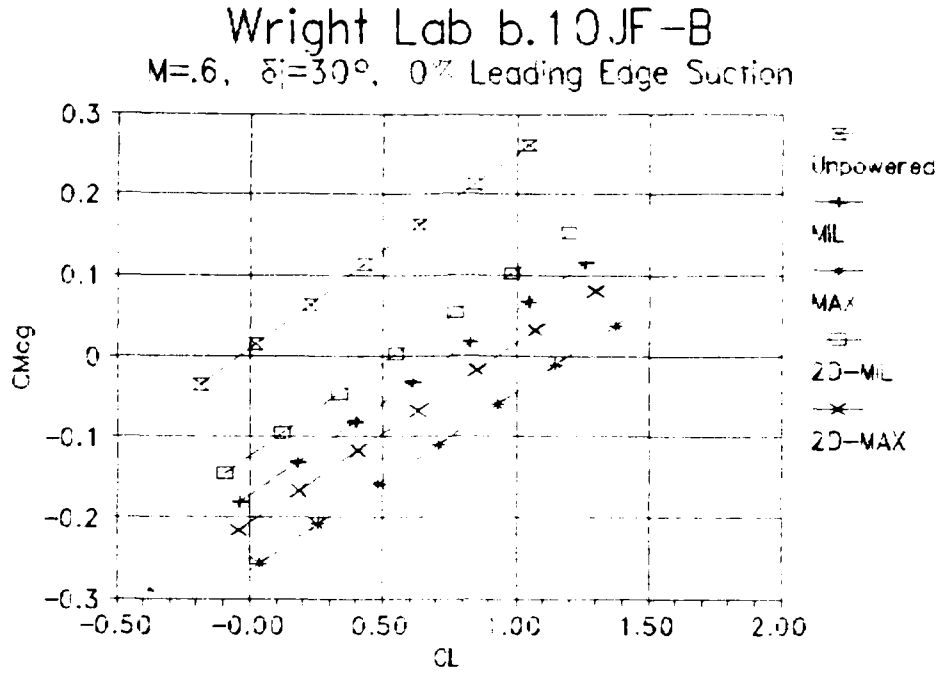

Figure 51 Pitching Moment About the CG for δ_j=30°

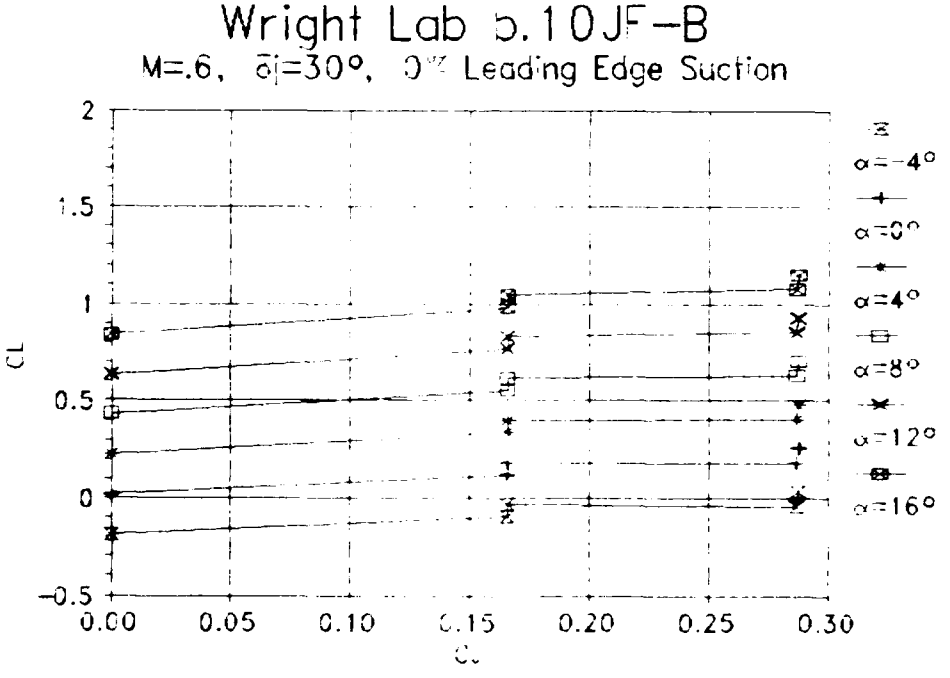

Figure 52 Lift Variation Due to C_μ for δ_j=30°

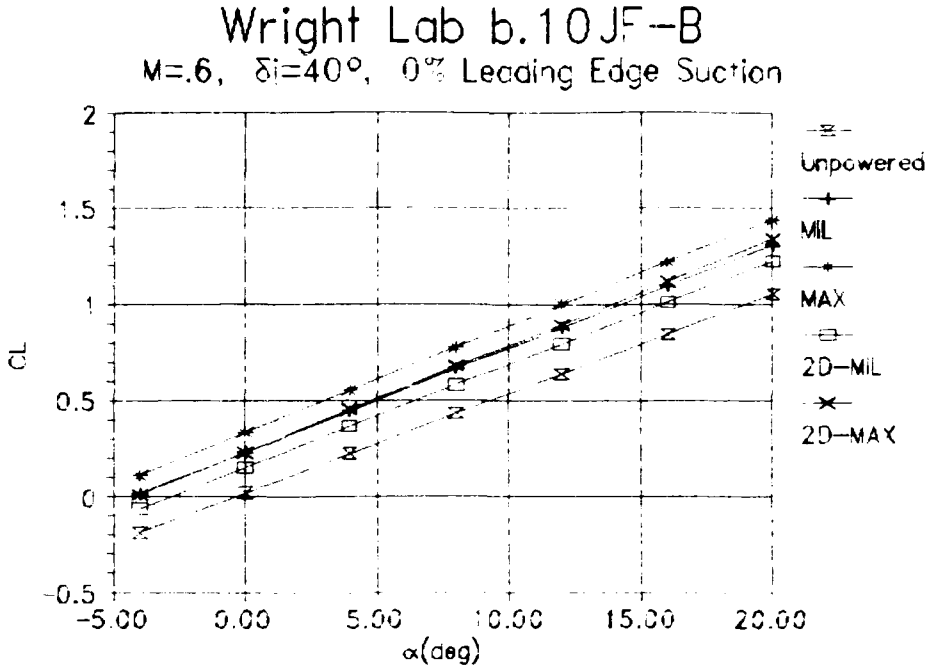

Figure 53 Lift Curve for δ_j=40°

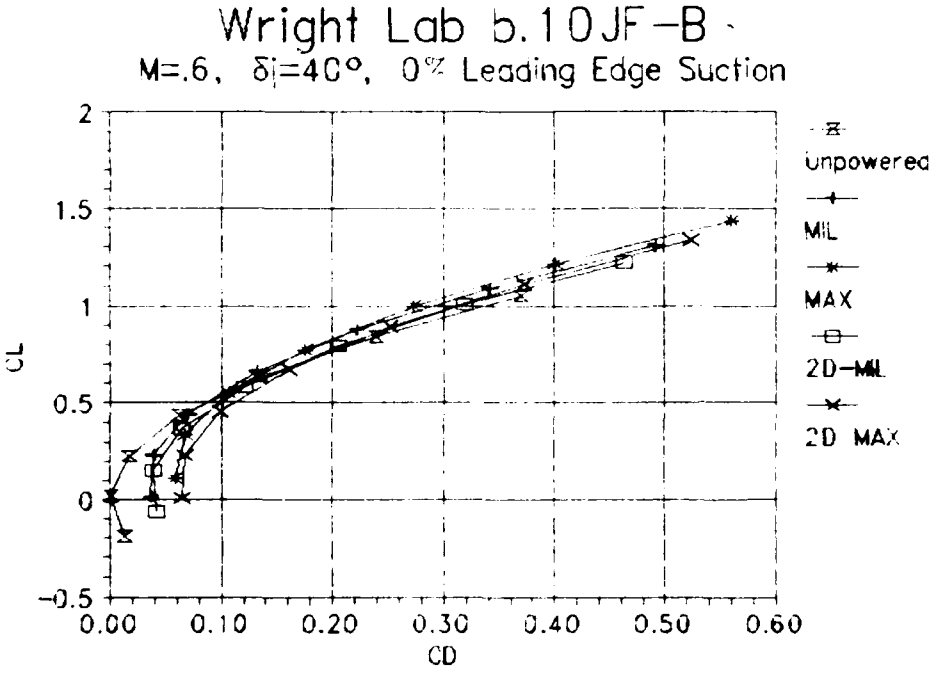

Figure 54 Drag Polar for δ_j=40°

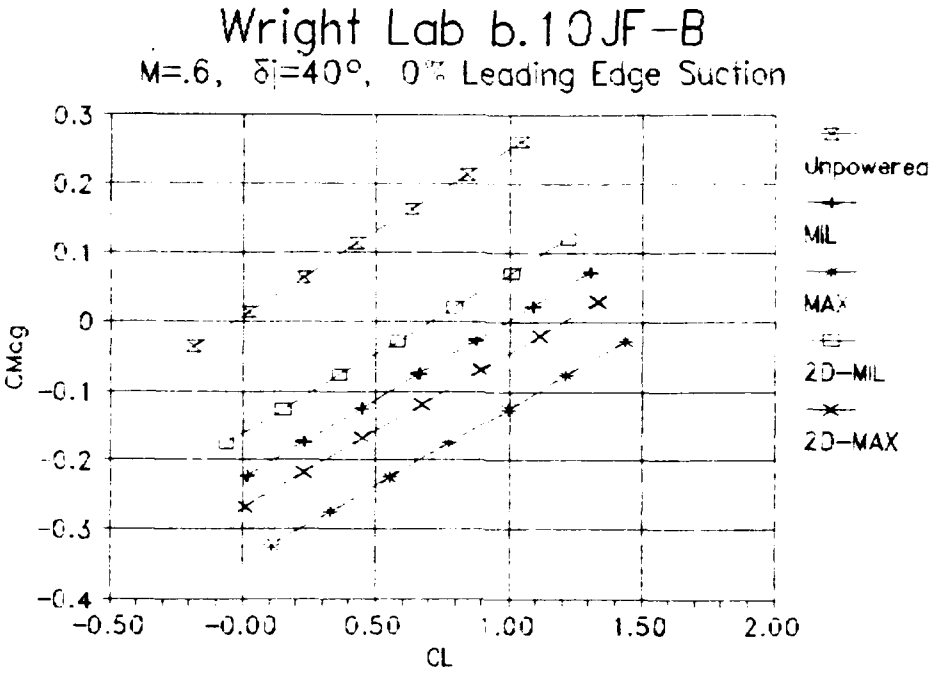

Figure 55 Pitching Moment About the CG for δ_j=40°

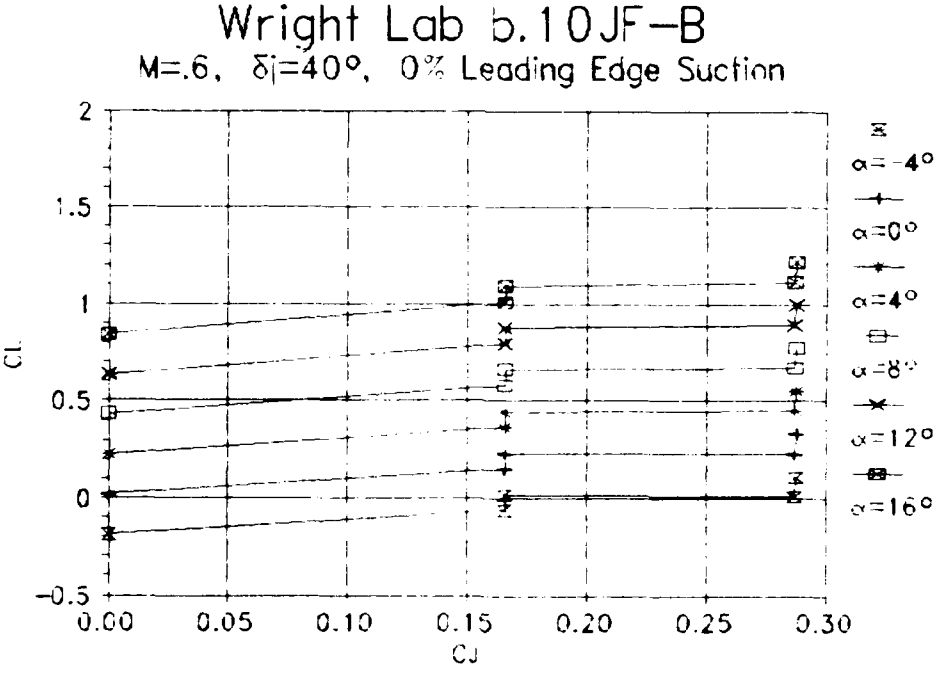

Figure 56 Lift Variation Due to C_J for δ_j=40°

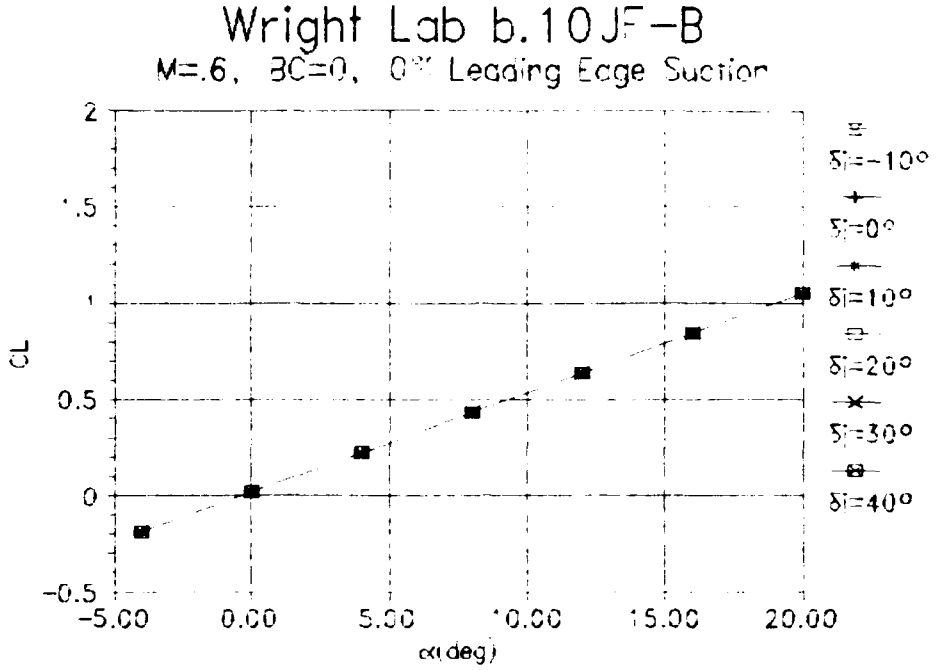

Figure 57 Lift Curve for BC=0

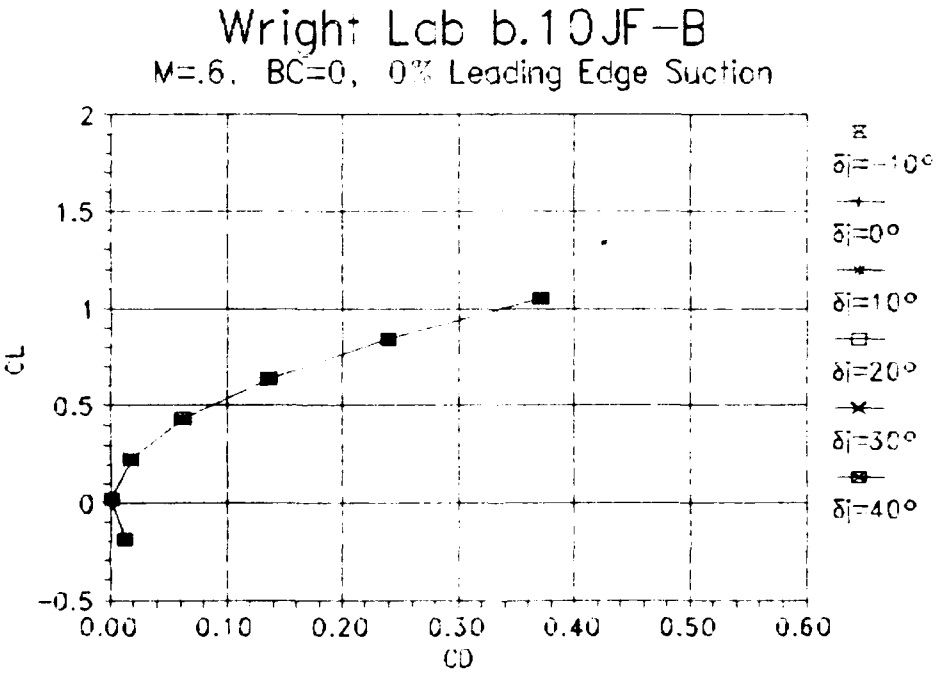

Figure 58 Drag Polar for BC=0

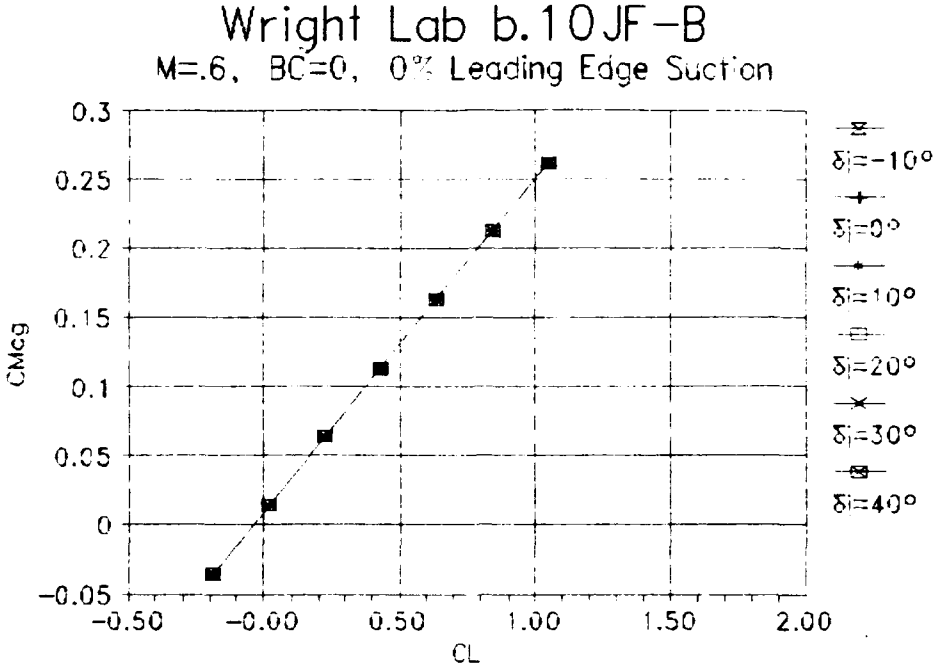

Figure 59 Pitching Moment About the CG for BC=0

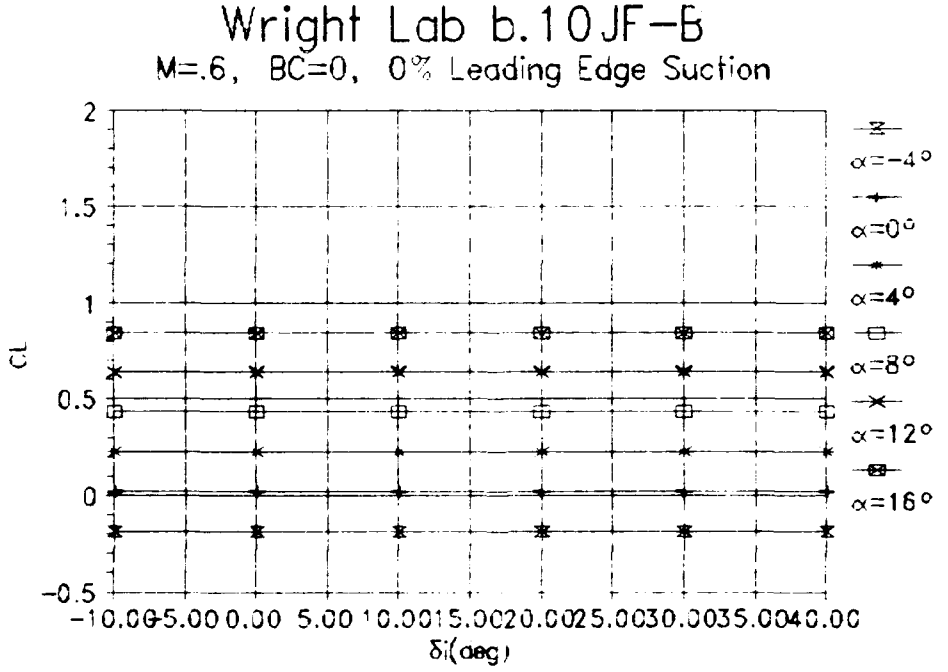

Figure 60 Lift Variation Due to δ_j for BC=0

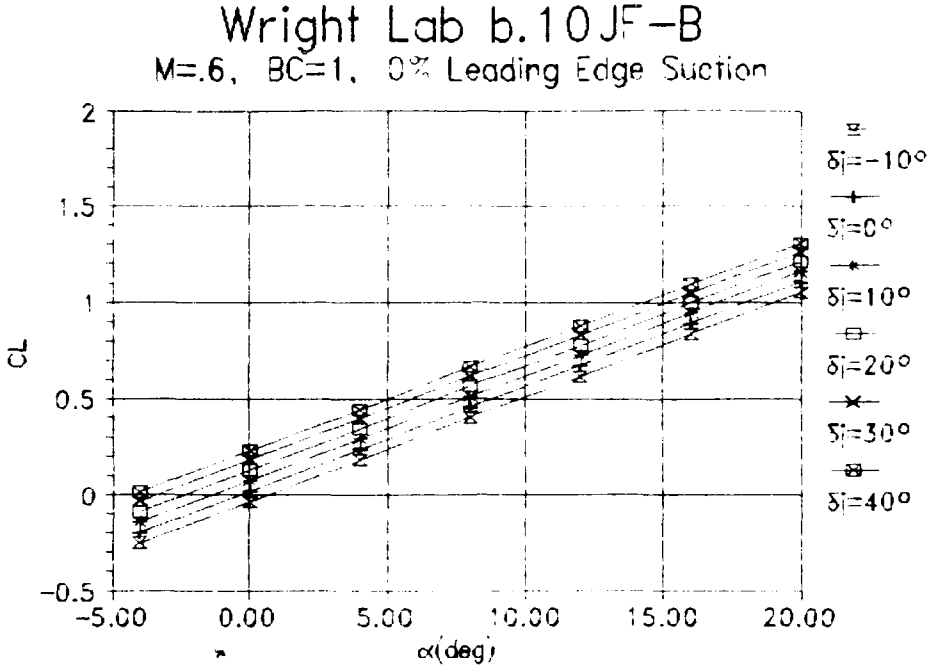

Figure 61 Lift Curve for BC=1

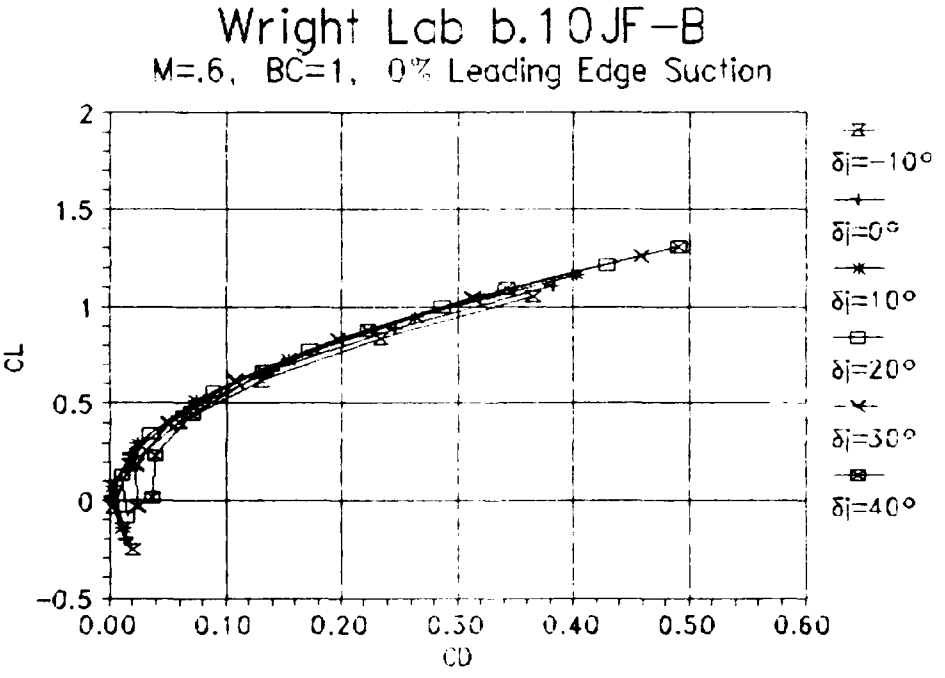

Figure 62 Drag Polar for BC=1

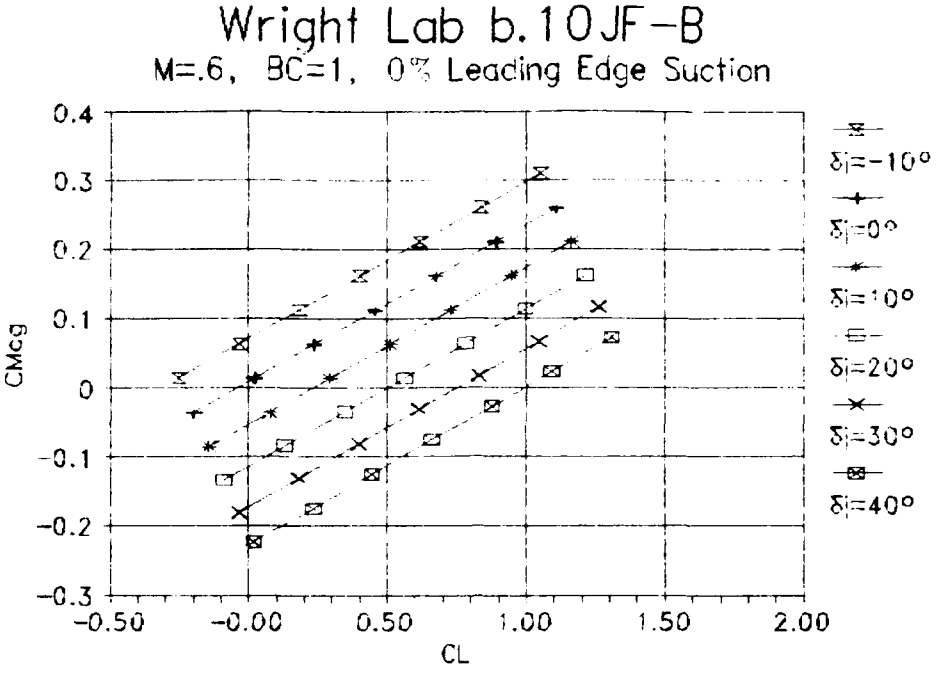

Figure 63 Pitching Moment About the CG for BC=1

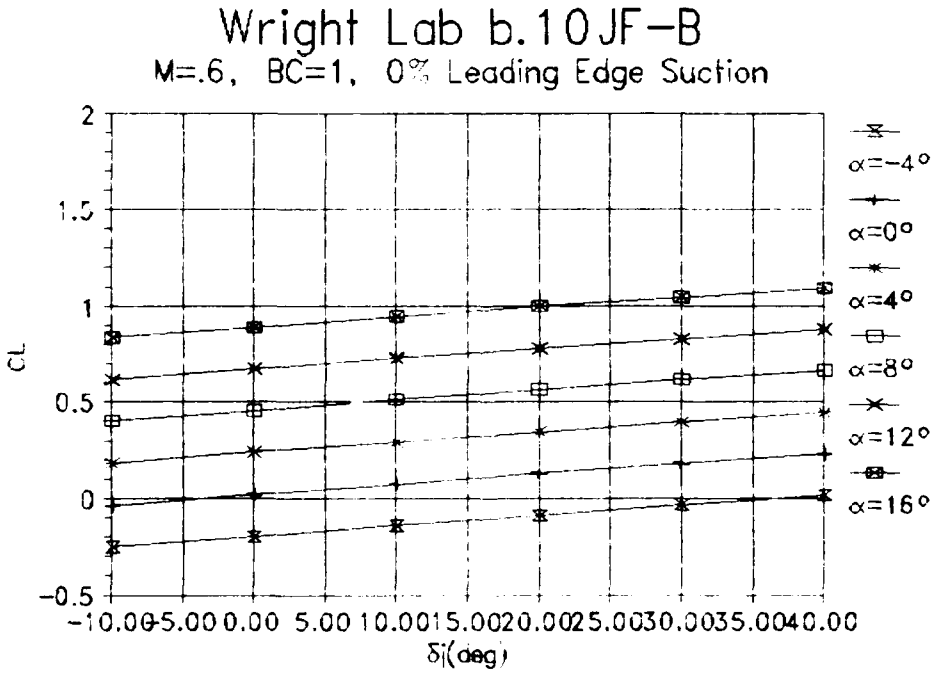

Figure 64 Lift Variation Due to δ_j for BC=1

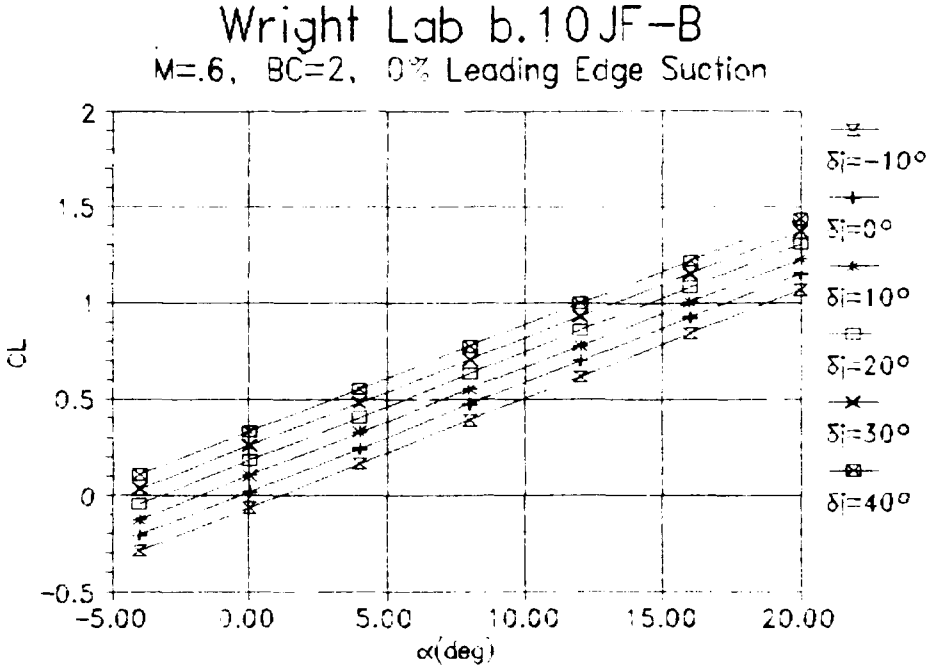

Figure 65 Lift Curve for BC=2

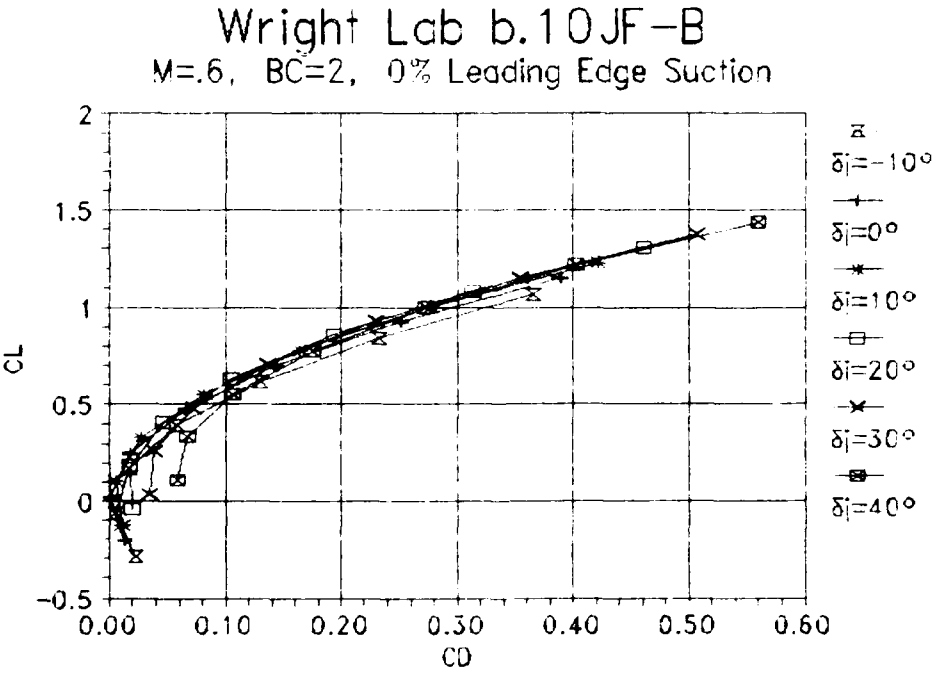

Figure 66 Drag Polar for BC=2

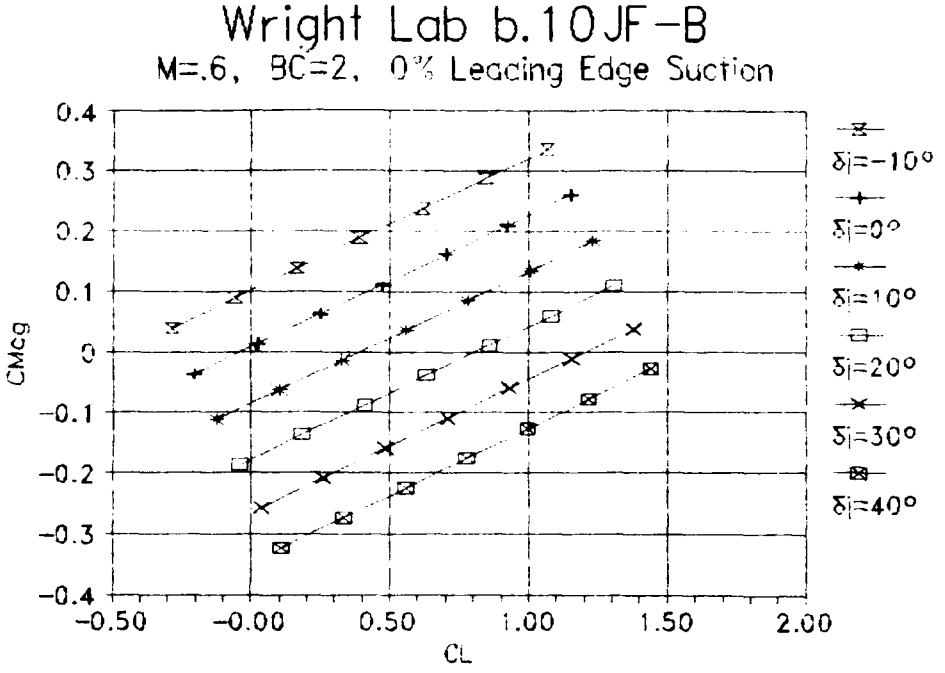

Figure 67 Pitching Moment About the CG for BC=2

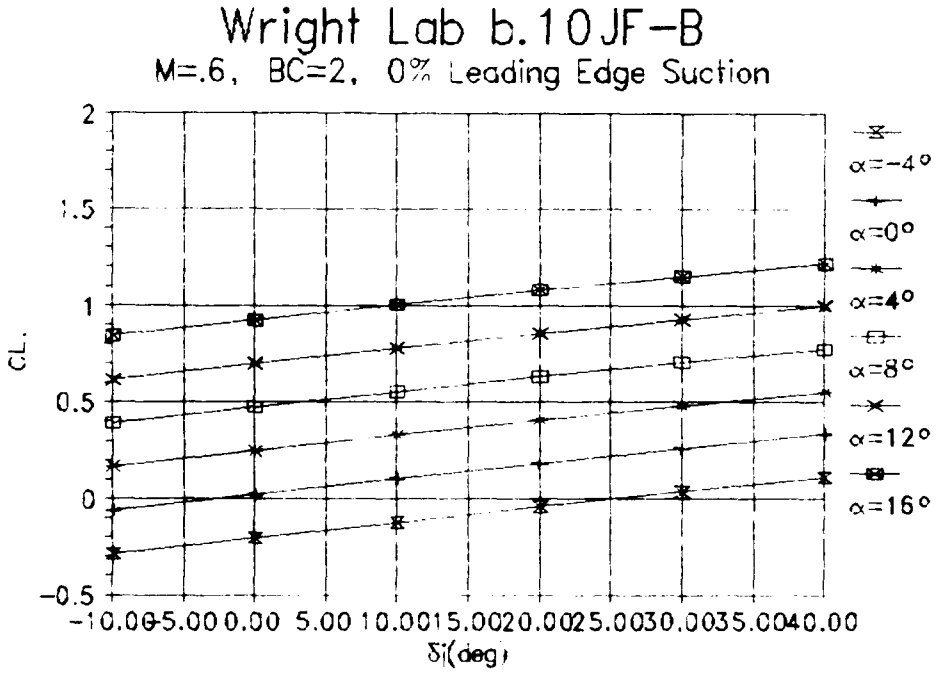

Figure 68 Lift Variation Due to δ_j for BC=2

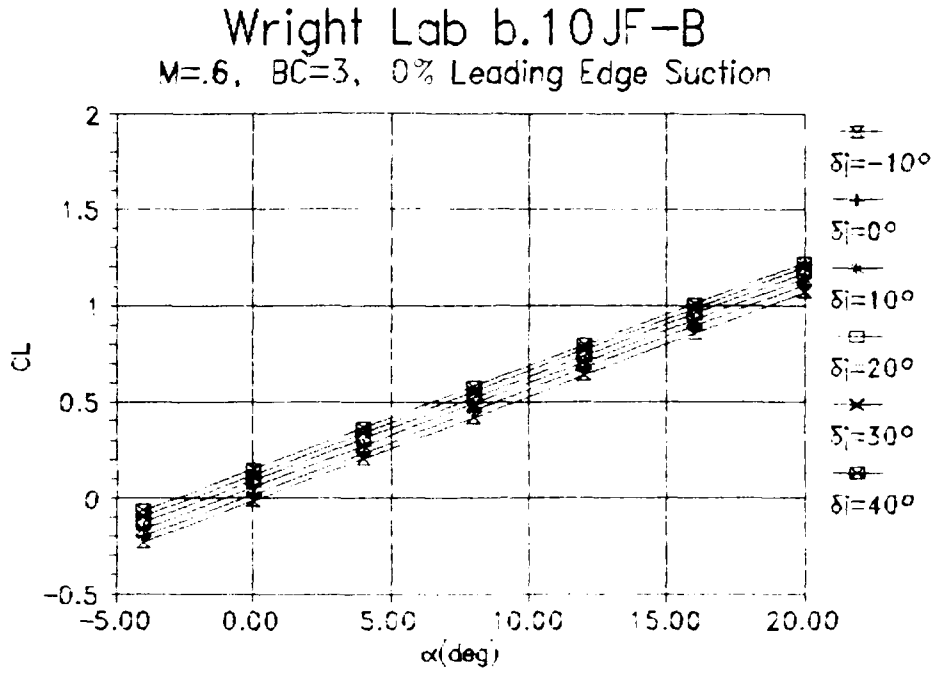

Figure 69 Lift Curve for BC=3

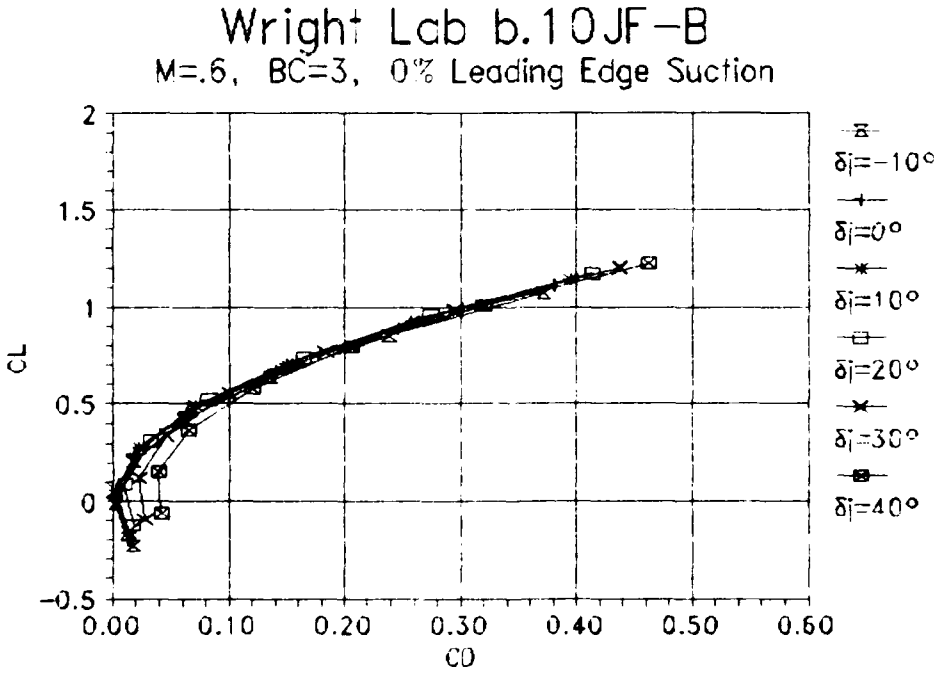

Figure 70 Drag Polar for BC=3

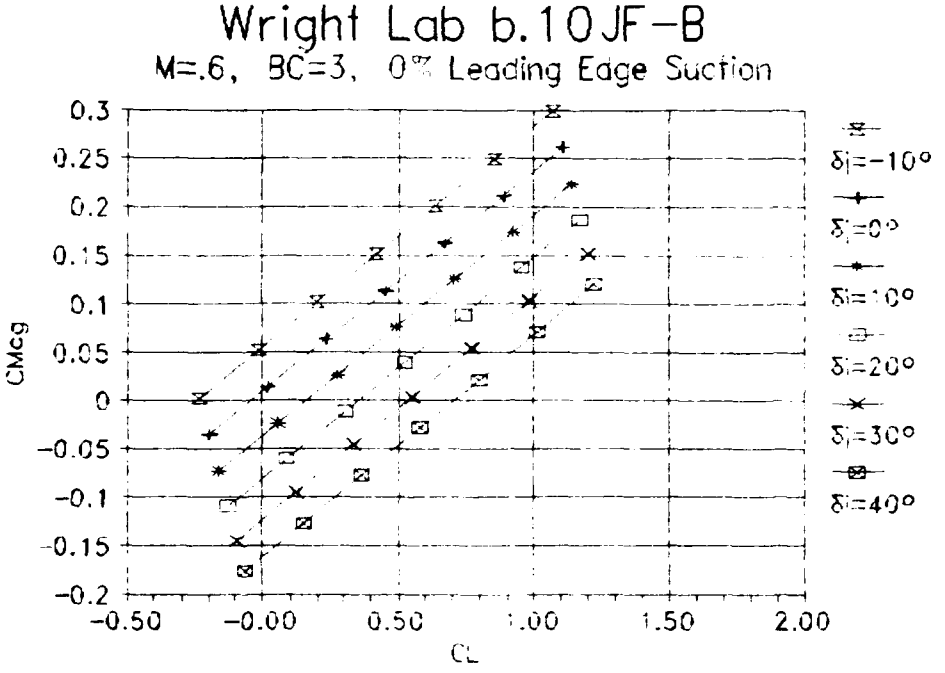

Figure 71 Pitching Moment About the CG for BC=3

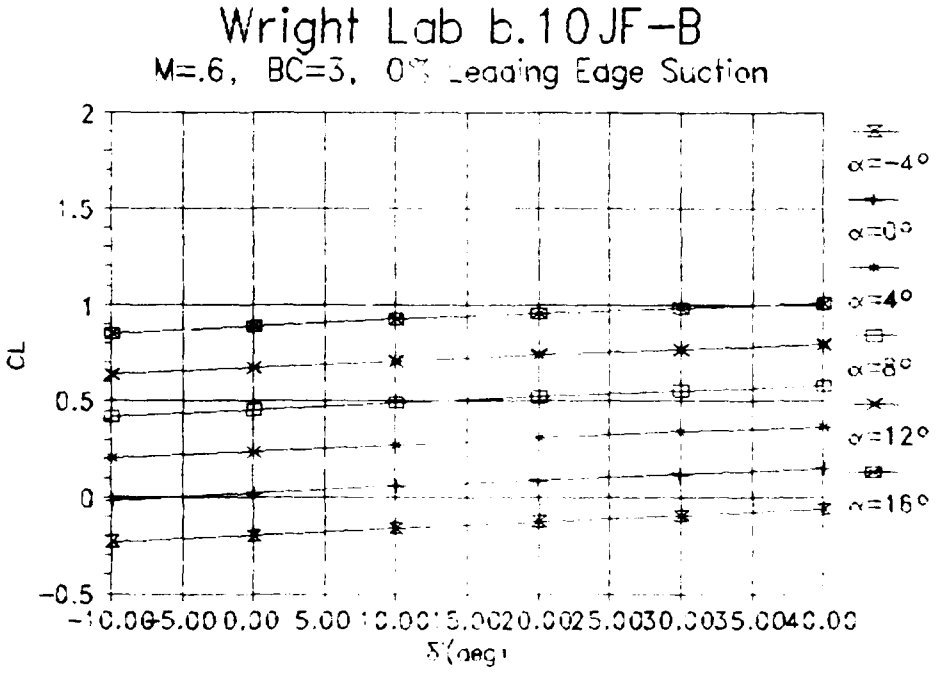

Figure 72 Lift Variation Due to δ_j for BC=3

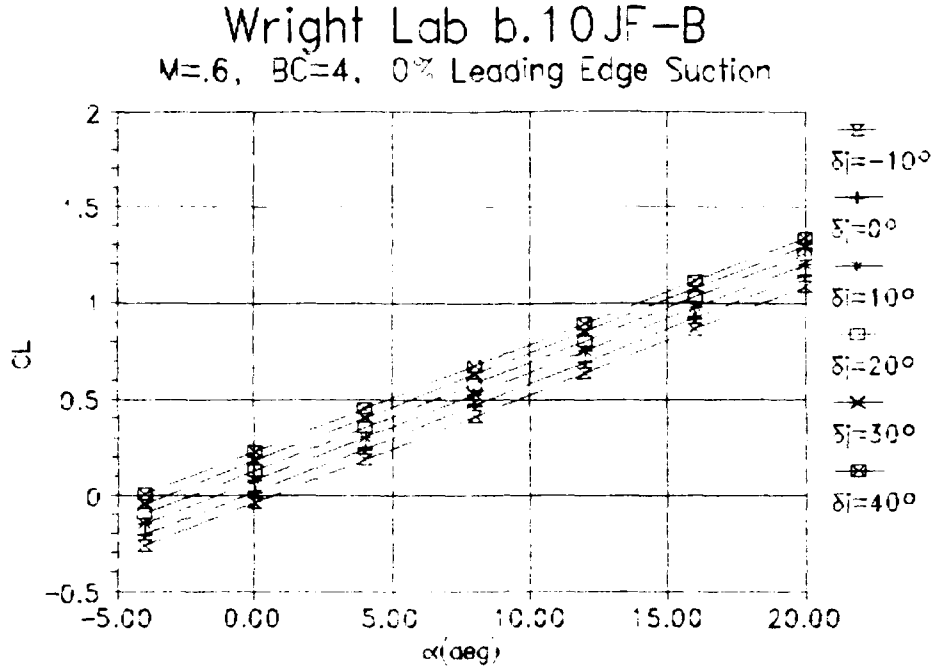

Figure 73 Lift Curve for BC=4

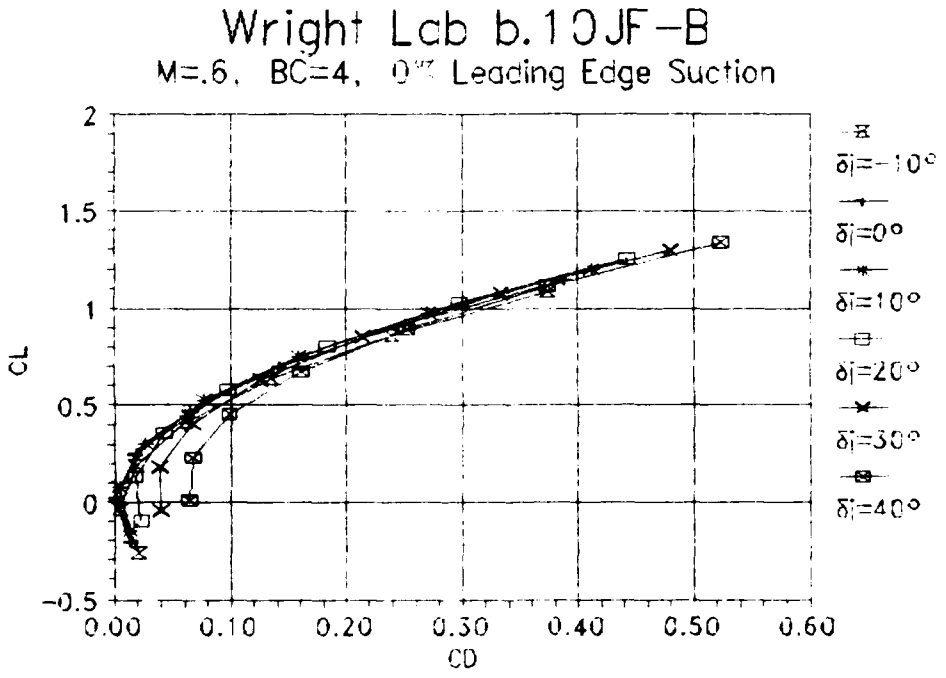

Figure 74 Drag Polar for BC=4

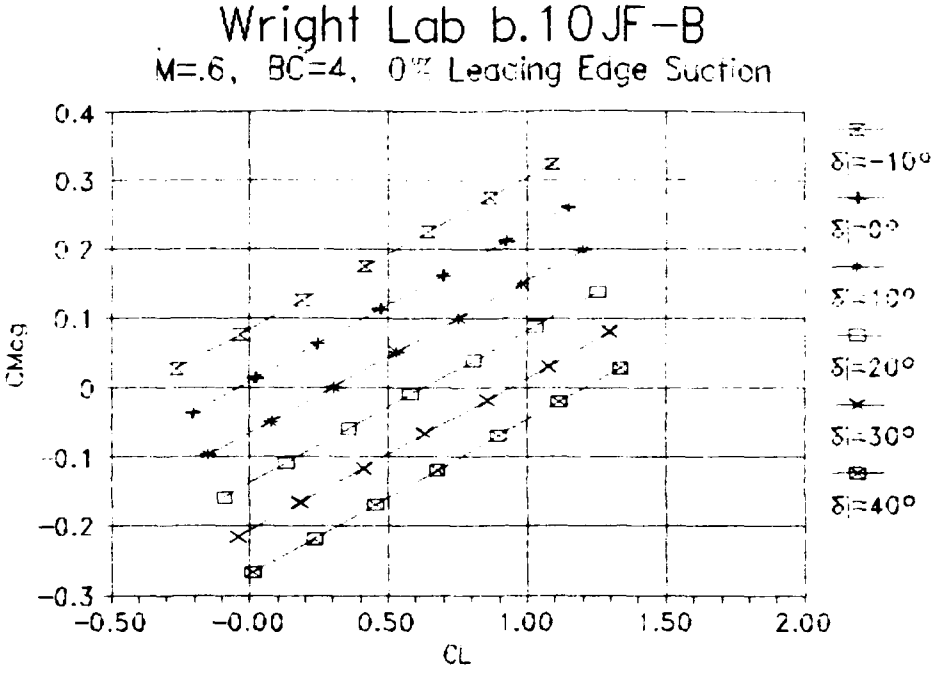

Figure 75 Pitching Moment About the CG for BC=4

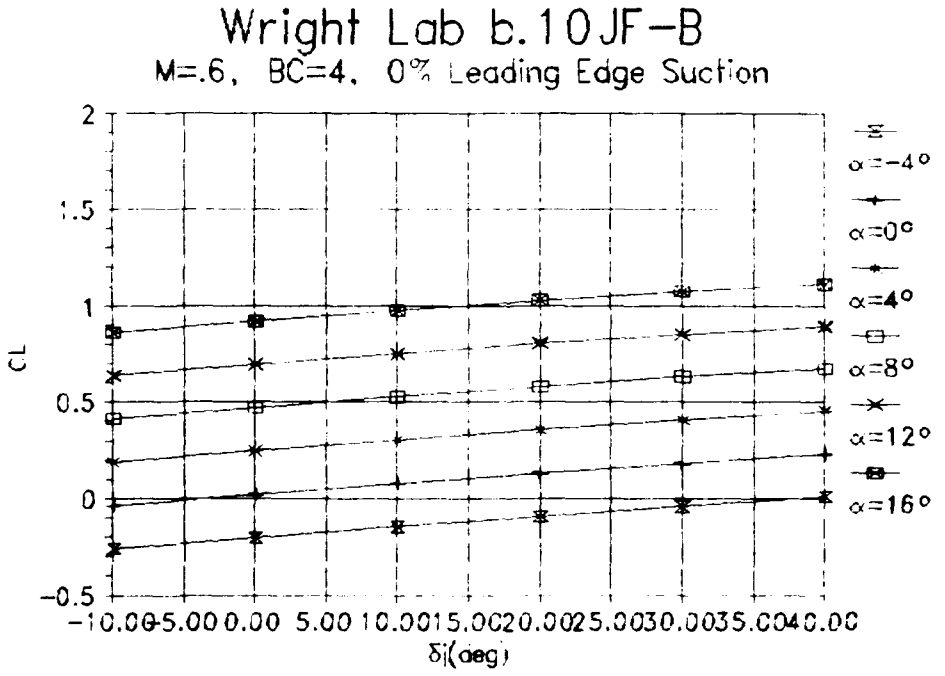

Figure 76 Lift Variation Due to δ_j for BC=4

Appendix C: Stability and Control Data

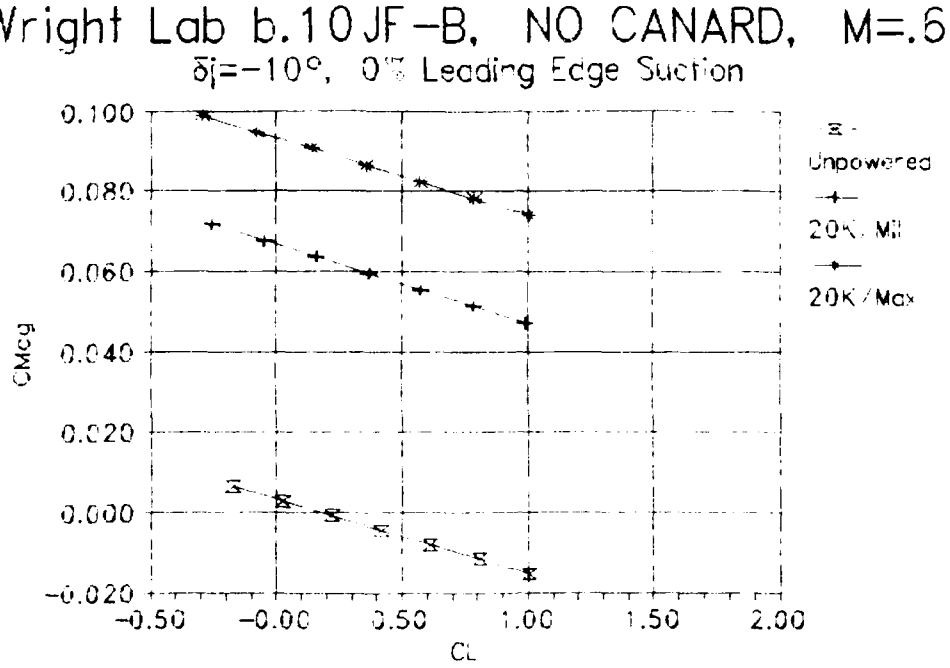

Figure 77 Pitching Moment About CG, δj=-10°, No Canard

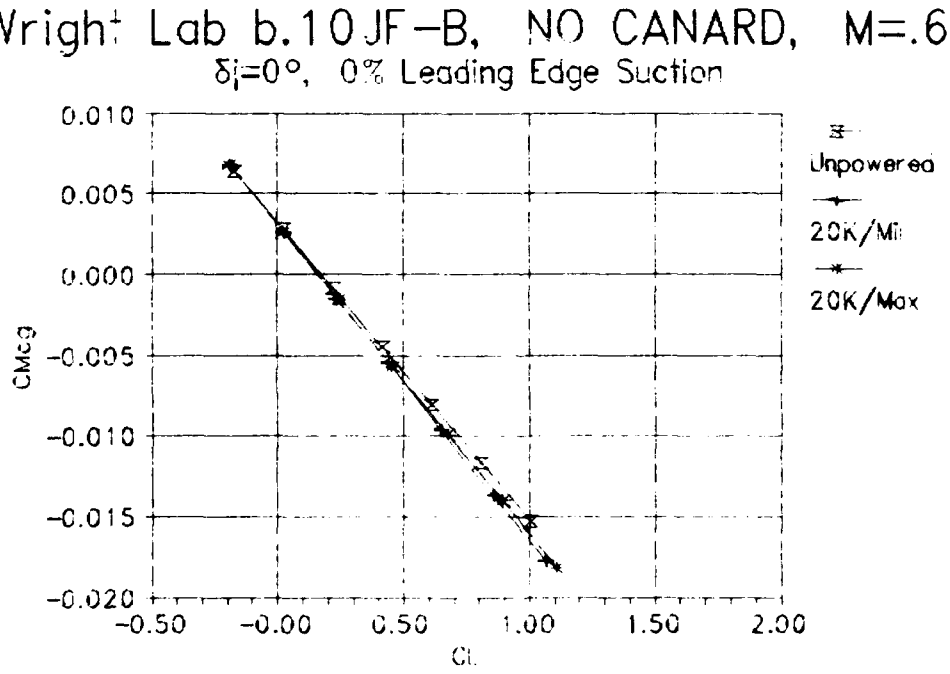

Figure 78 Pitching Moment About CG, δj=0°, No Canard

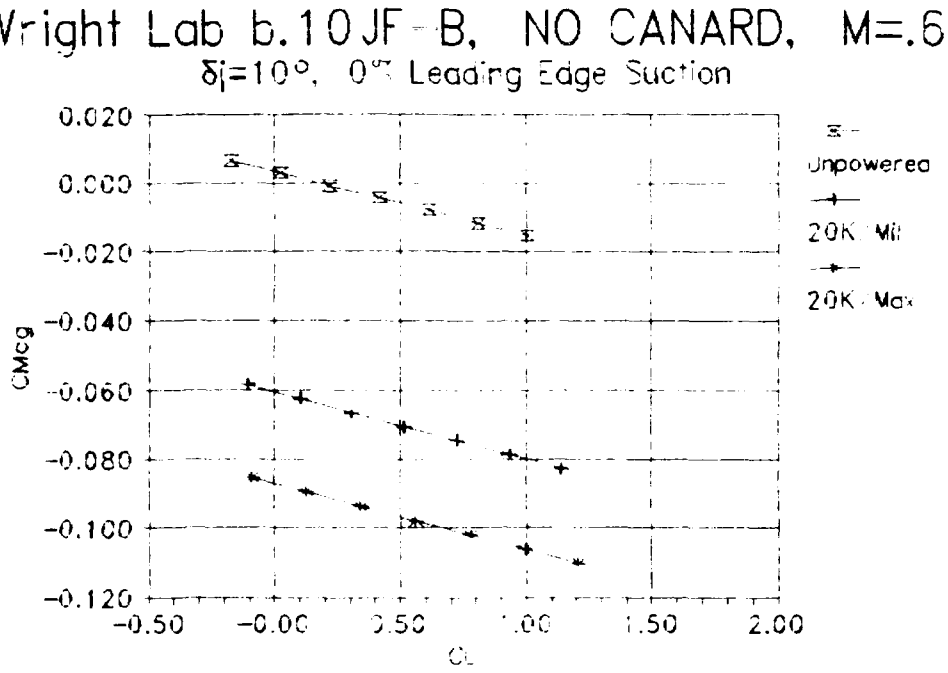

Figure 79 Pitching Moment About CG, δj=10°, No Canard

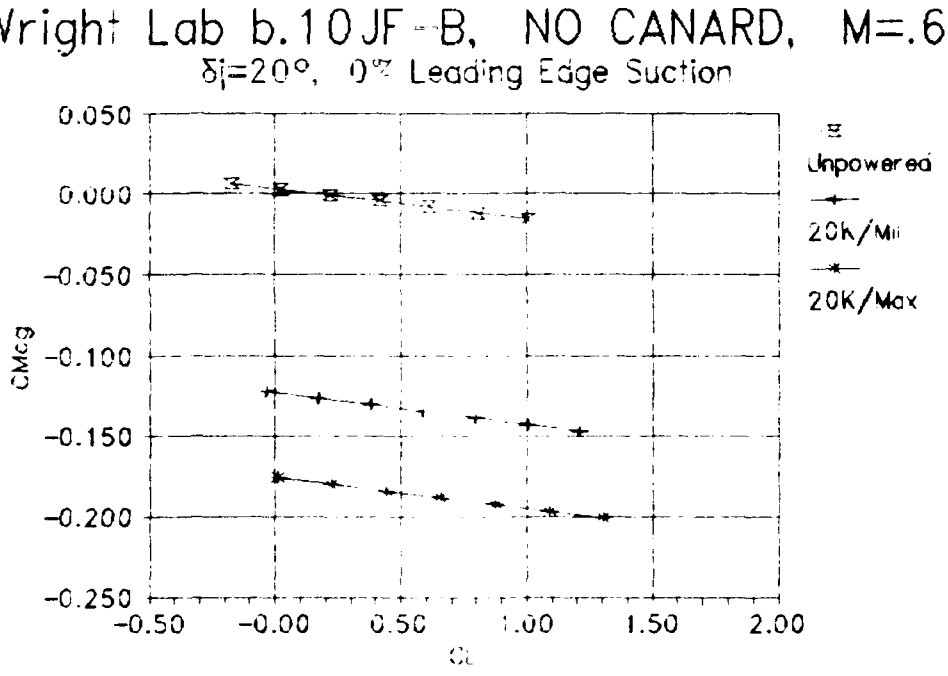

Figure 80 Pitching Moment About CG, δj=20°, No Canard

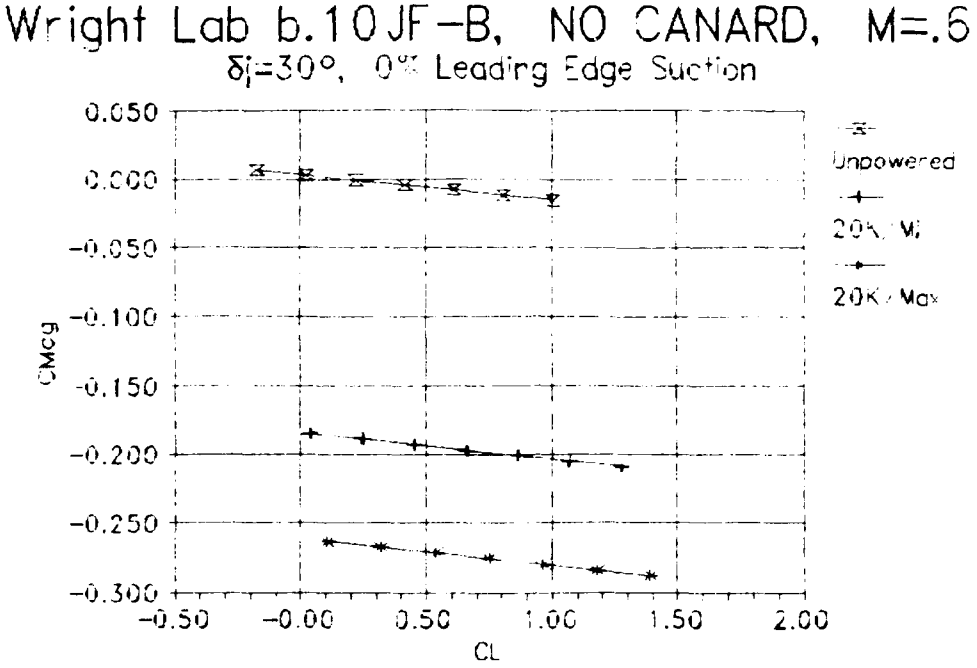

Figure 81 Pitching Moment About CG, δj=30°, No Canard

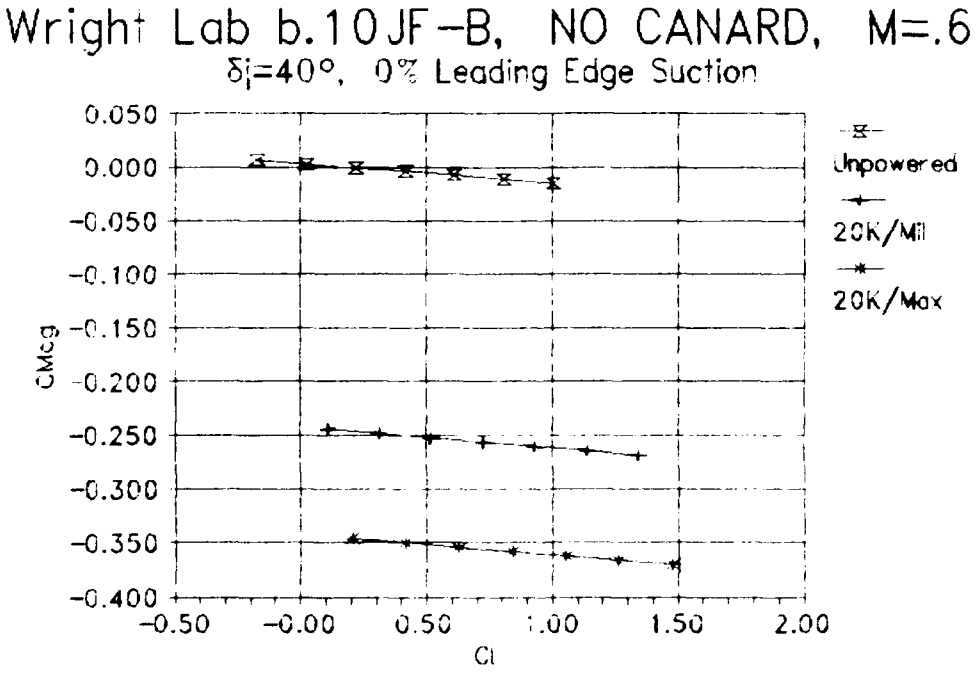

Figure 82 Pitching Moment About CG, δj=40°, No Canard

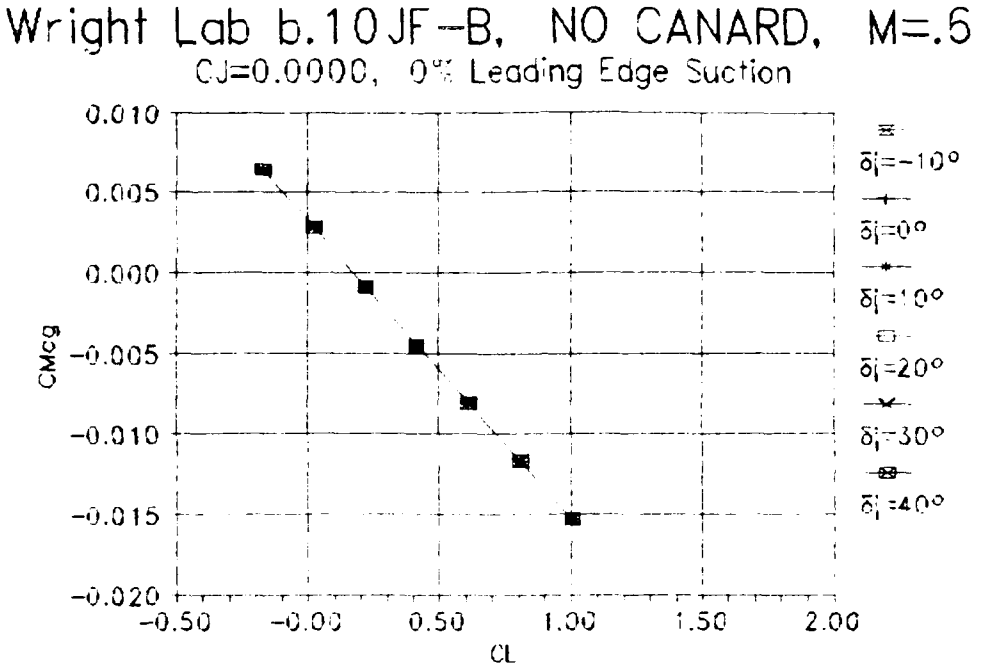

Figure 83 Pitching Moment About CG, BC=0, No Canard

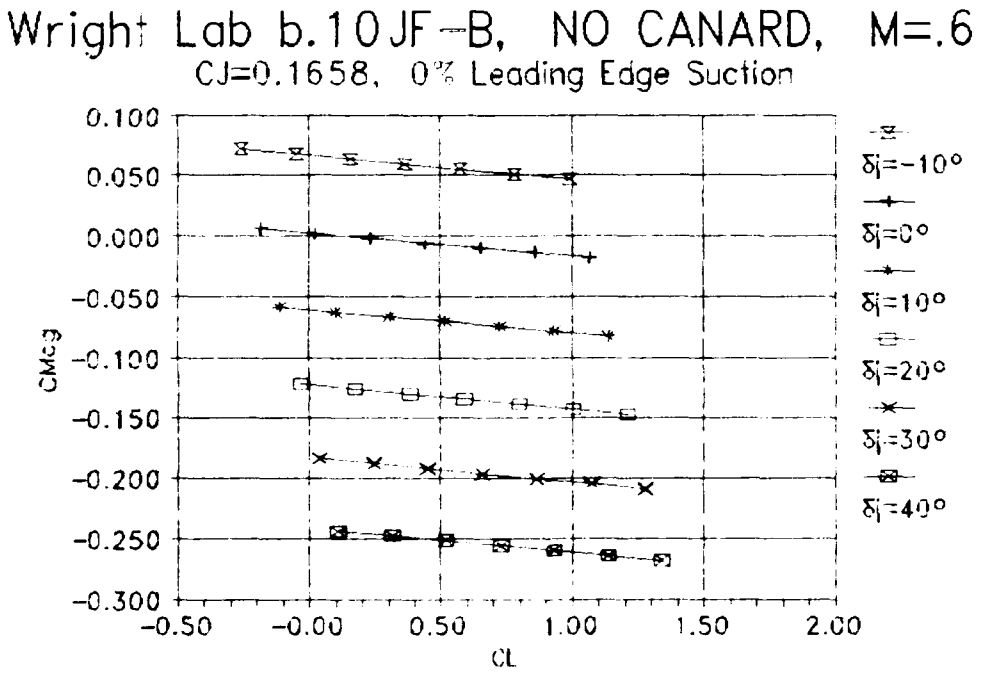

Figure 84 Pitching Moment About CG, BC=1, No Canard

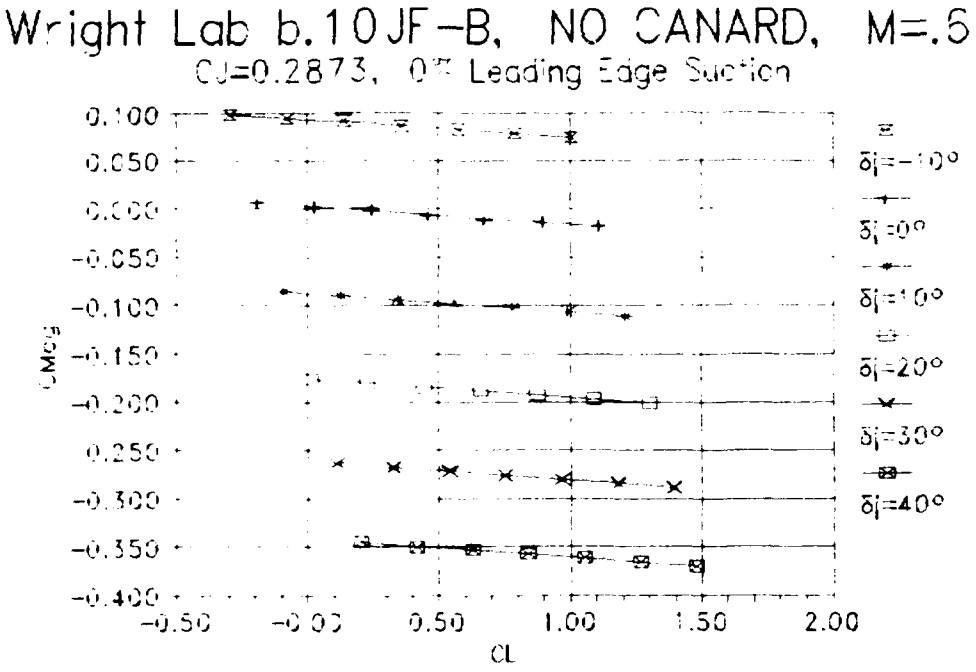

Figure 85 Pitching Moment About CG, BC=2, No Canard

Appendix D: Planform Data

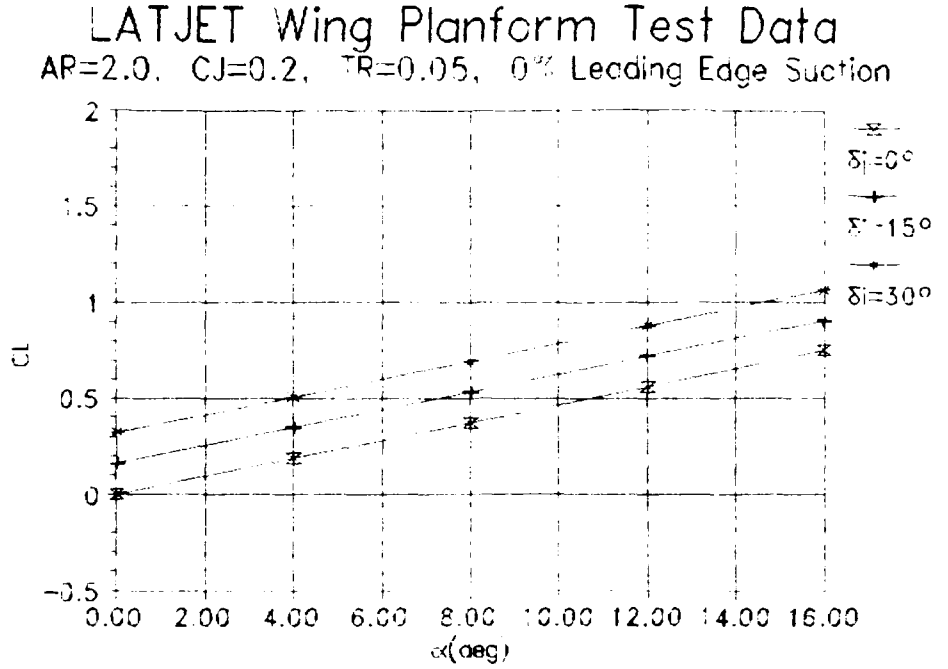

Figure 86 Lift Curve Comparison for δ_j, AR=2, λ=0.05

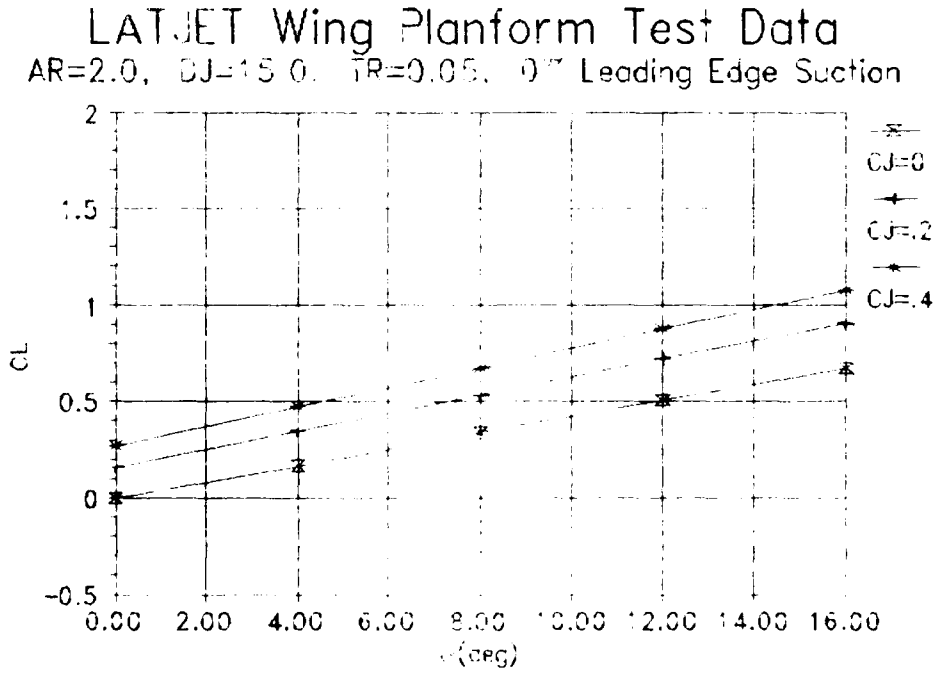

Figure 87 Lift Curve Comparison for BC, AR=2, λ=0.05

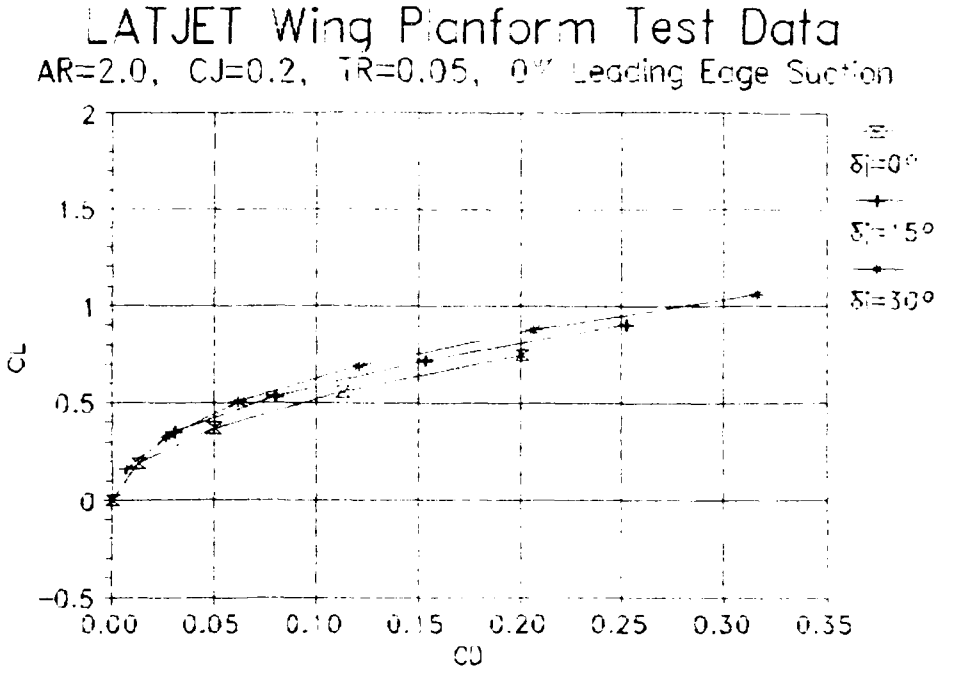

Figure 88 Drag Polar Comparison for δ_j, AR=2, λ=0.05

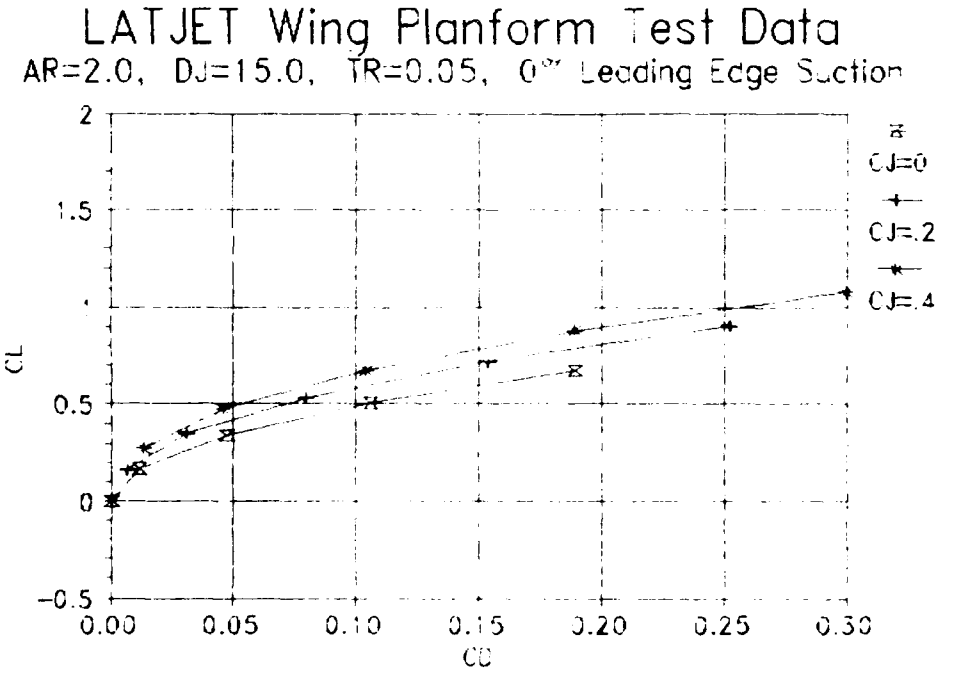

Figure 89 Drag Polar Comparison for BC, AR=2, λ=0.05

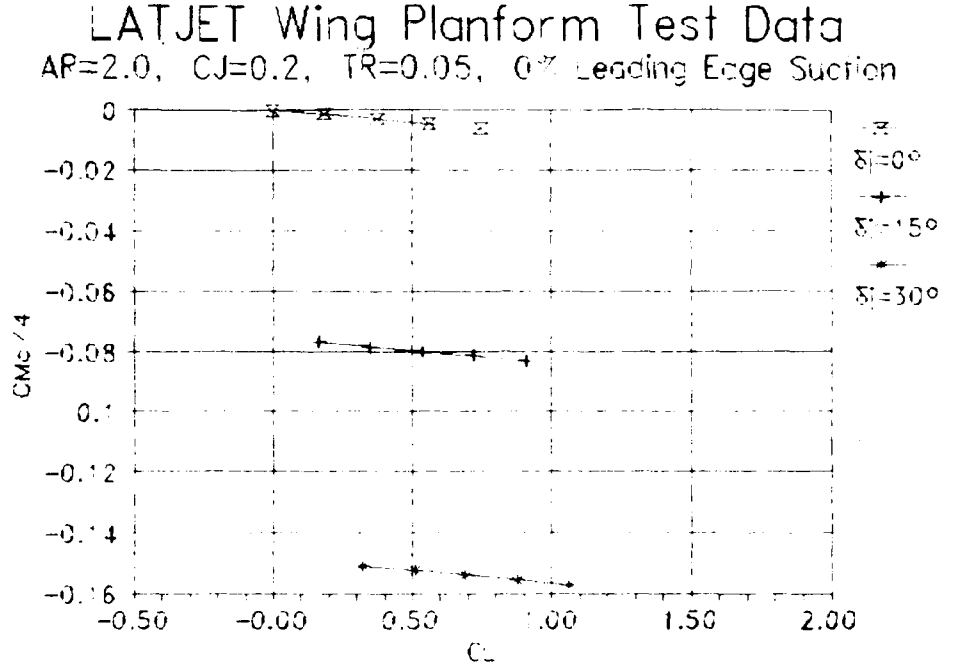

Figure 90 Moment Comparison for δj, AR=2, λ=0.05

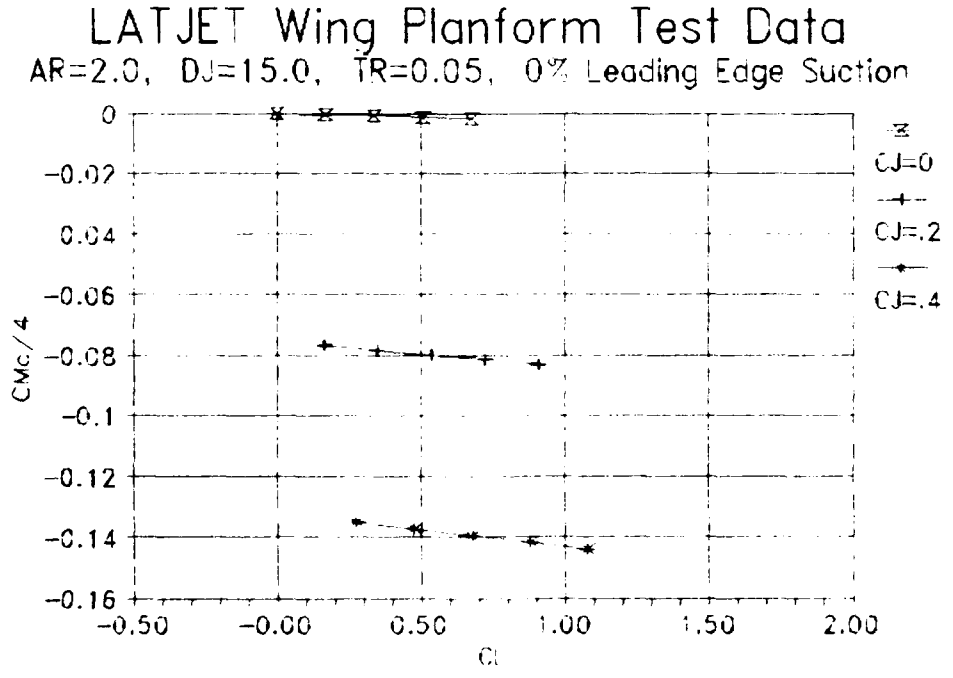

Figure 91 Moment Comparison for BC, AR=2, λ=0.05

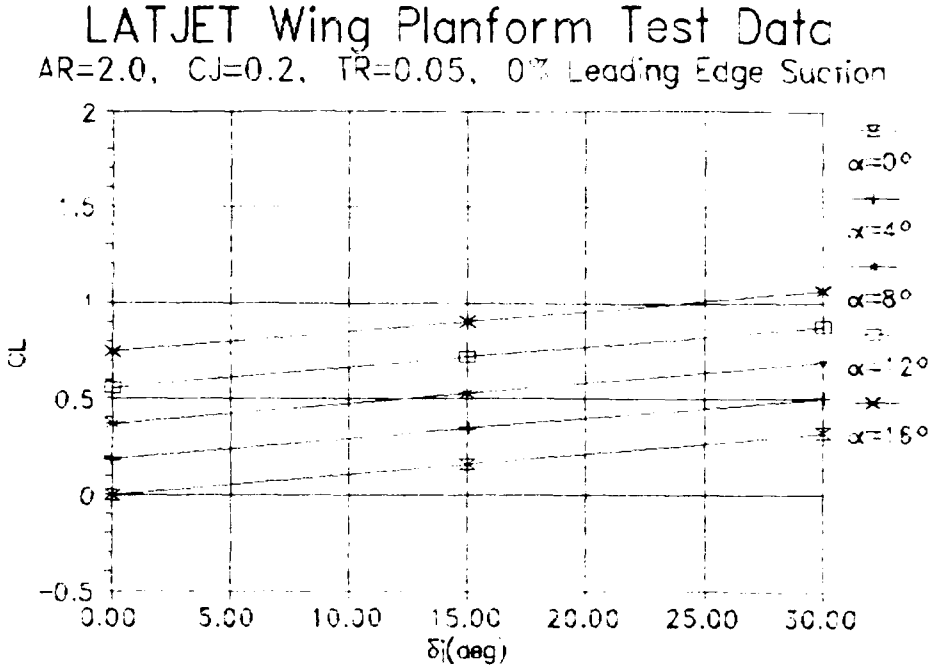

Figure 92 Lift vs δ_j, AR=2, λ=0.05

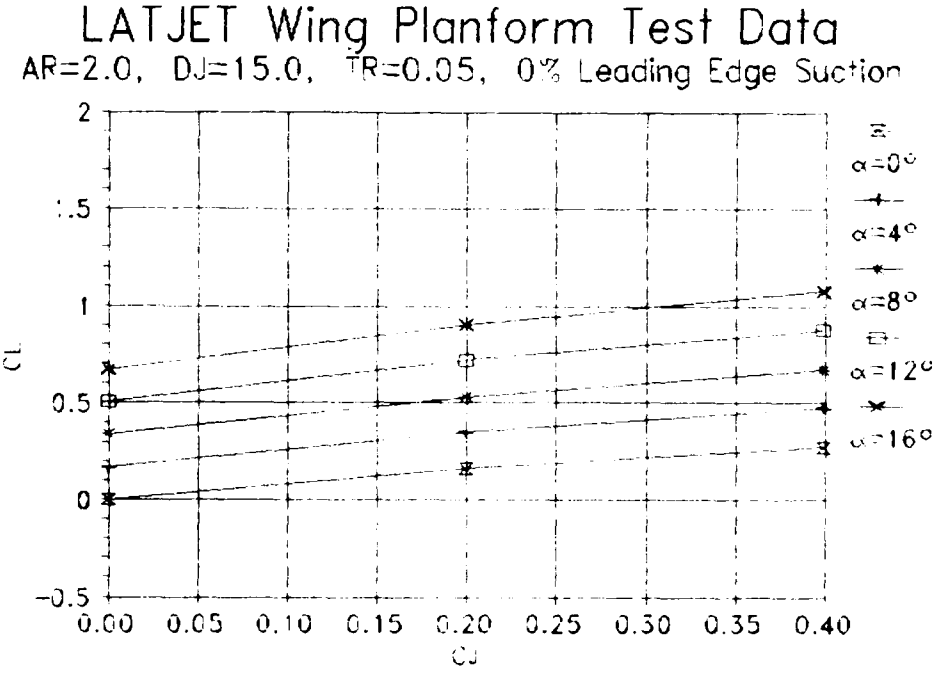

Figure 93 Lift vs C_j, AR=2, λ=0.05

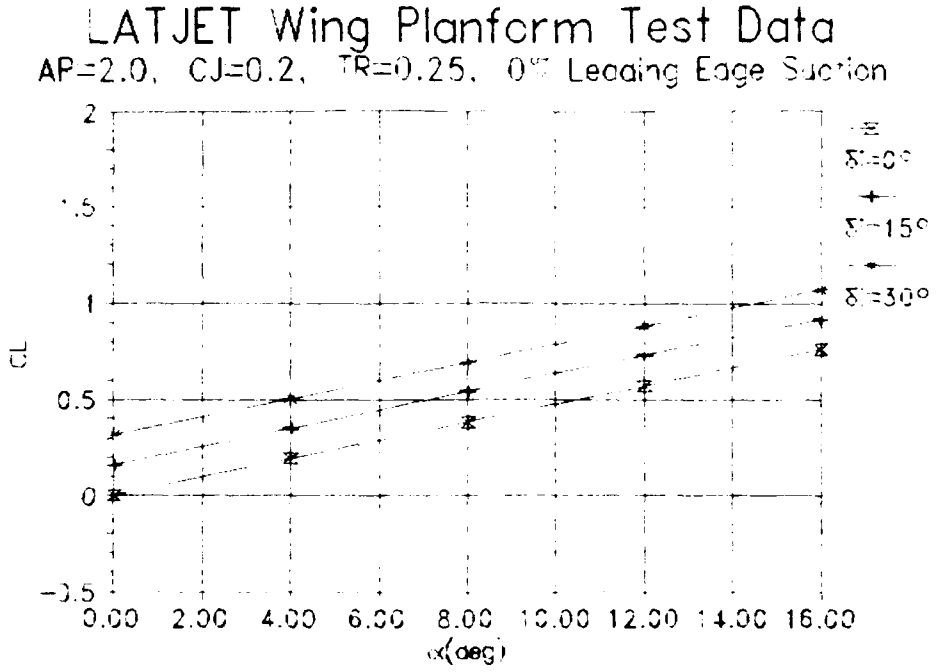

Figure 94 Lift Curve Comparison for δ_j, AR=2, λ=0.25

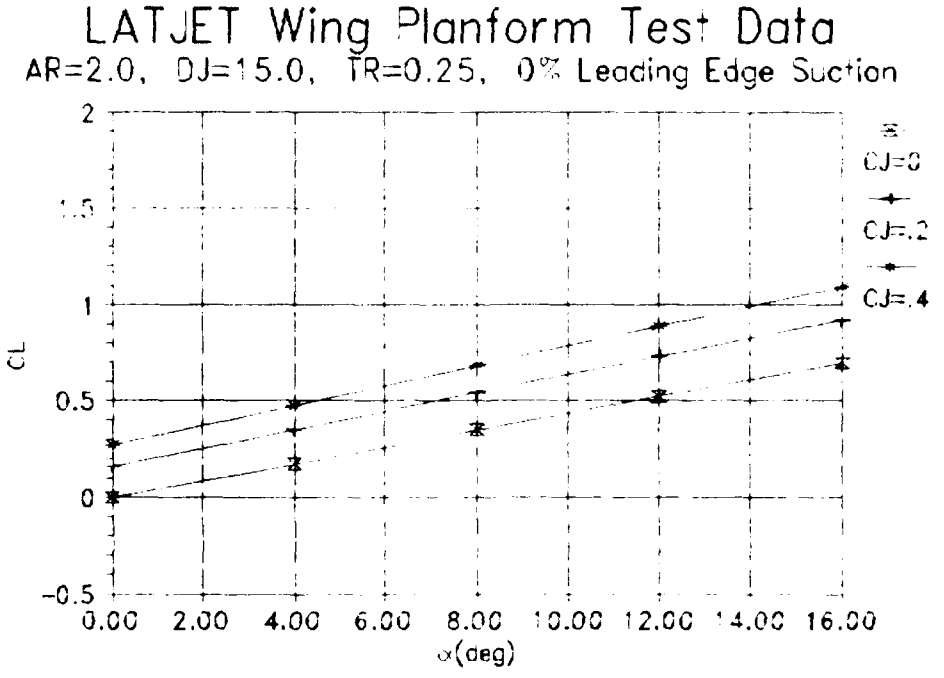

Figure 95 Lift Curve Comparison for BC, AR=2, λ=0.25

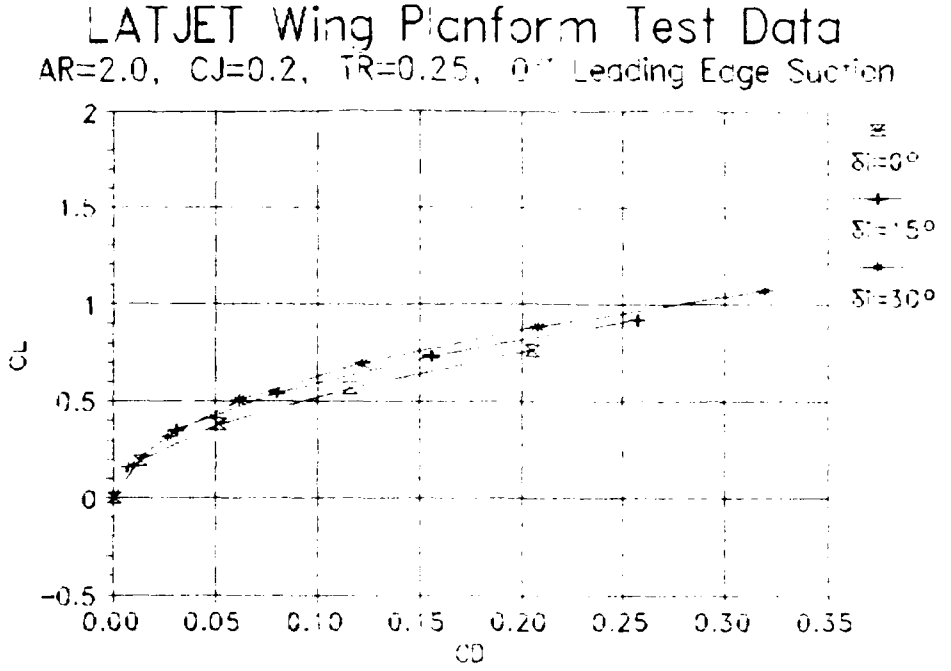

Figure 96 Drag Polar Comparison for δ_j, AR=2, λ=0.25

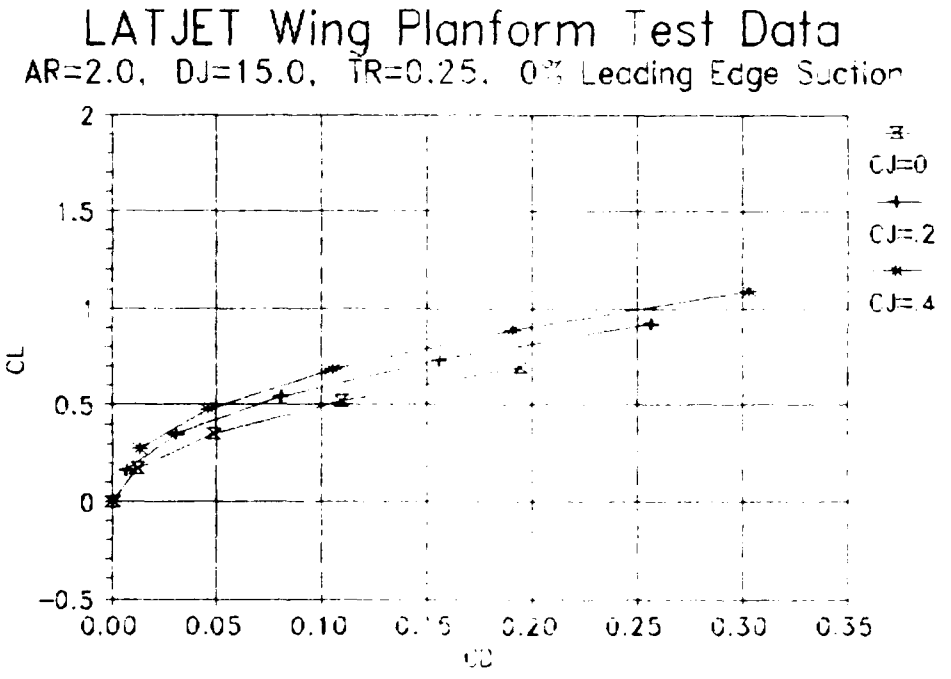

Figure 97 Drag Polar Comparison for BC, AR=2, λ=0.25

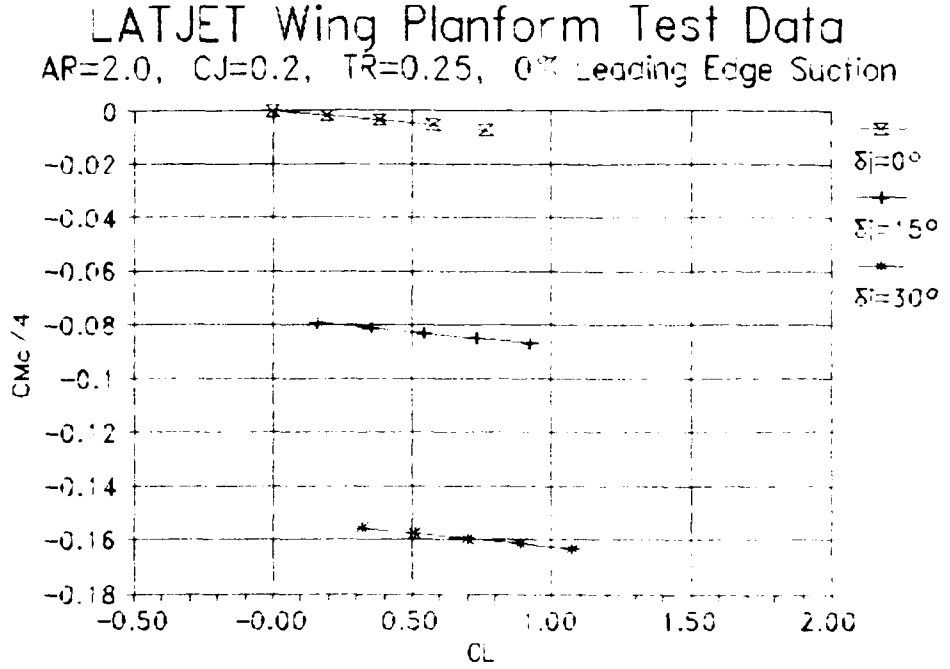

Figure 98 Moment Comparison for δj, AR=2, λ=0.25

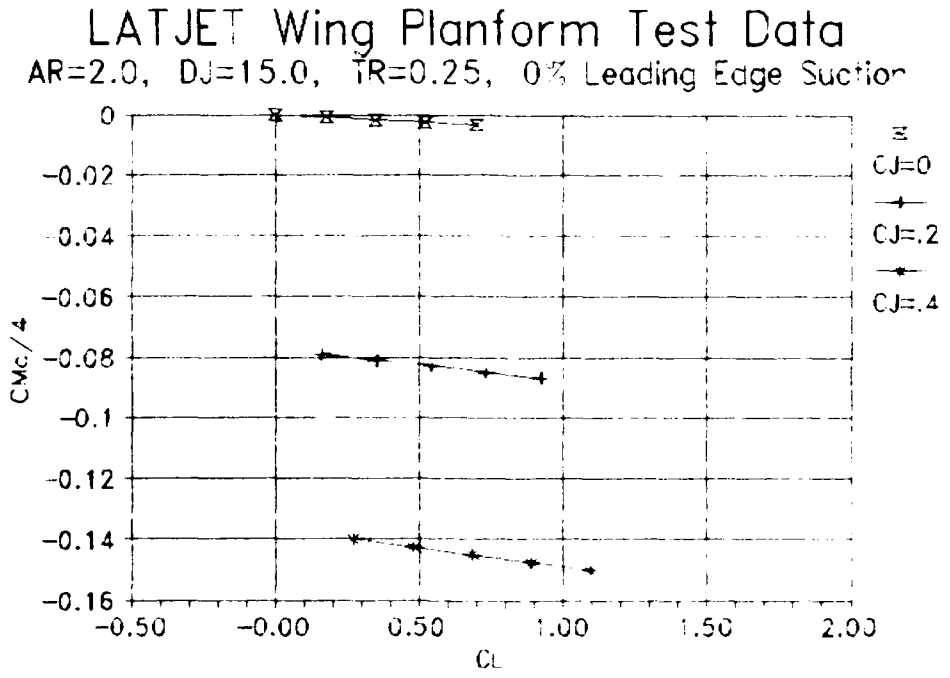

Figure 99 Moment Comparison for BC, AR=2, λ=0.25

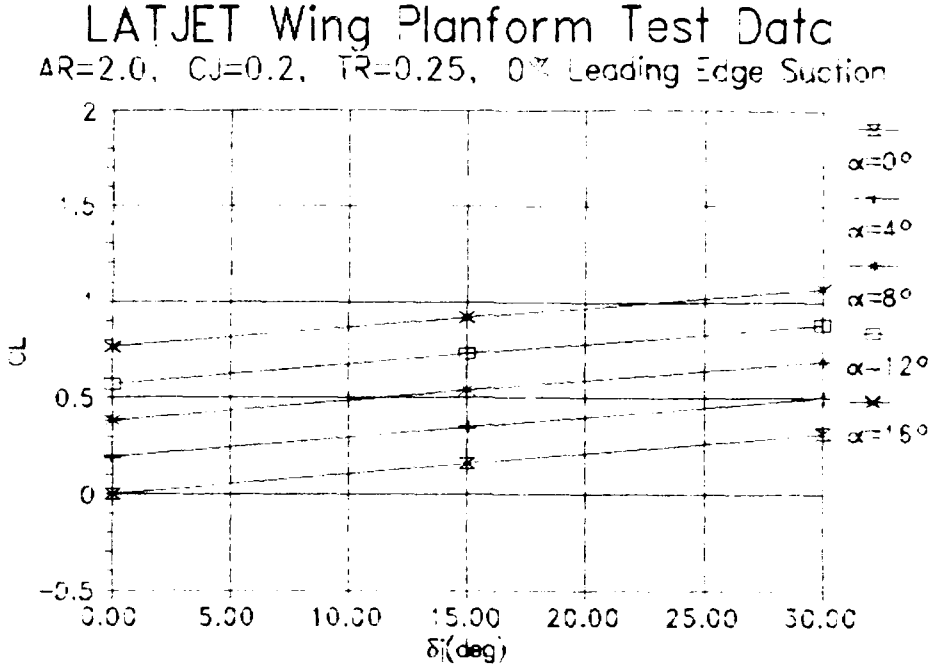

Figure 100 Lift vs δ_j, AR=2, λ=0.25

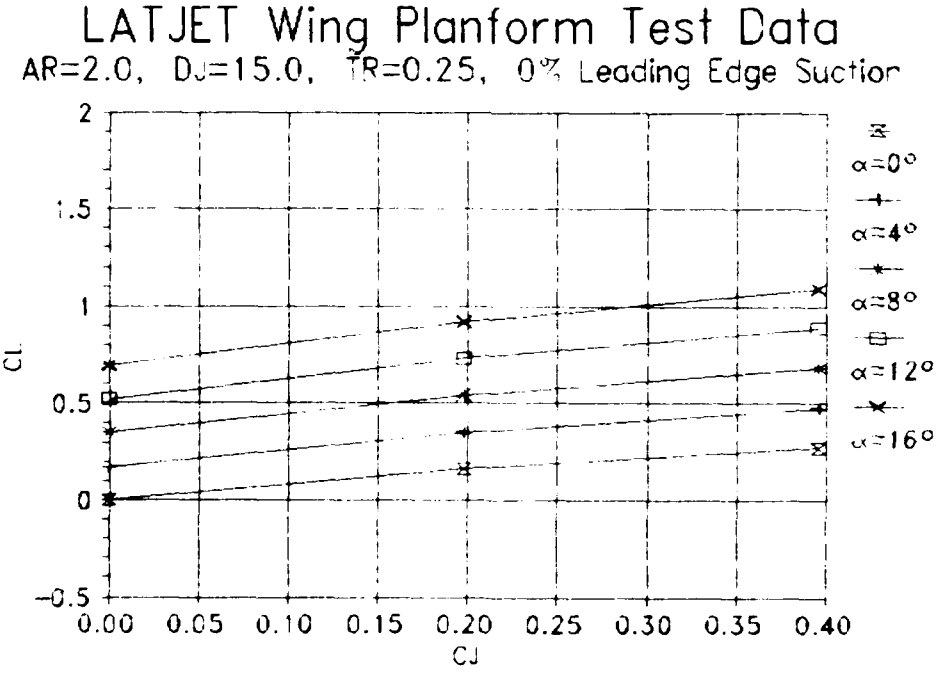

Figure 101 Lift vs C_j, AR=2, λ=0.25

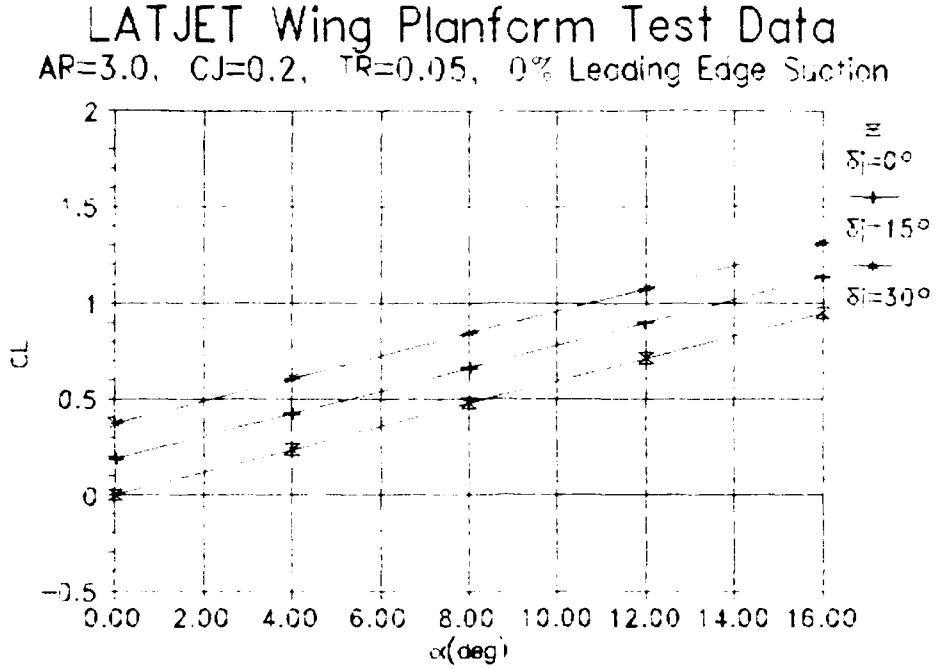

Figure 102 Lift Curve Comparison for δ_j, AR=3, λ=0.05

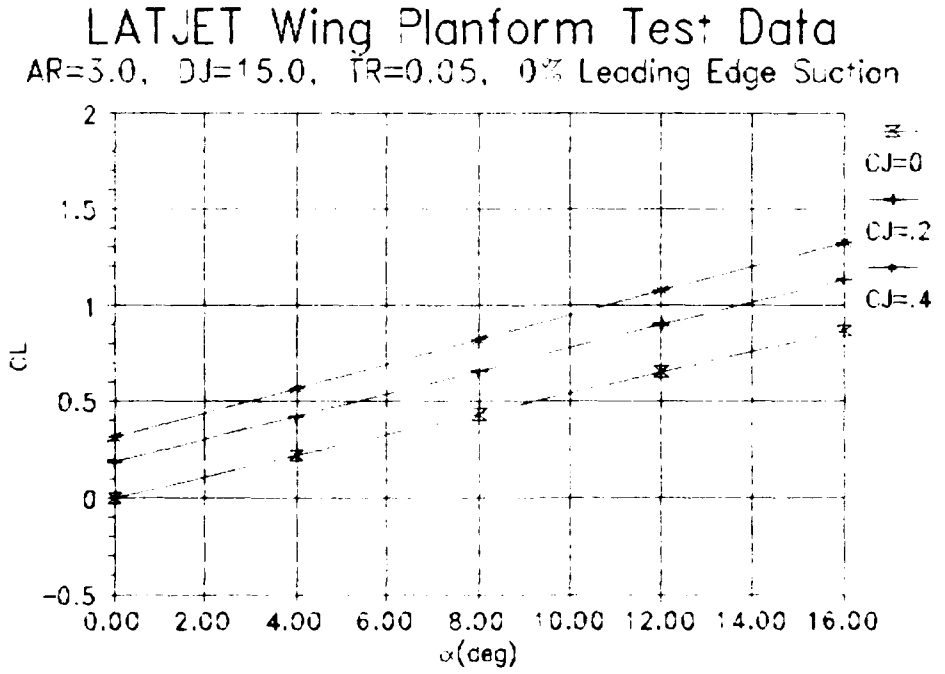

Figure 103 Lift Curve Comparison for BC, AR=3, λ=0.05

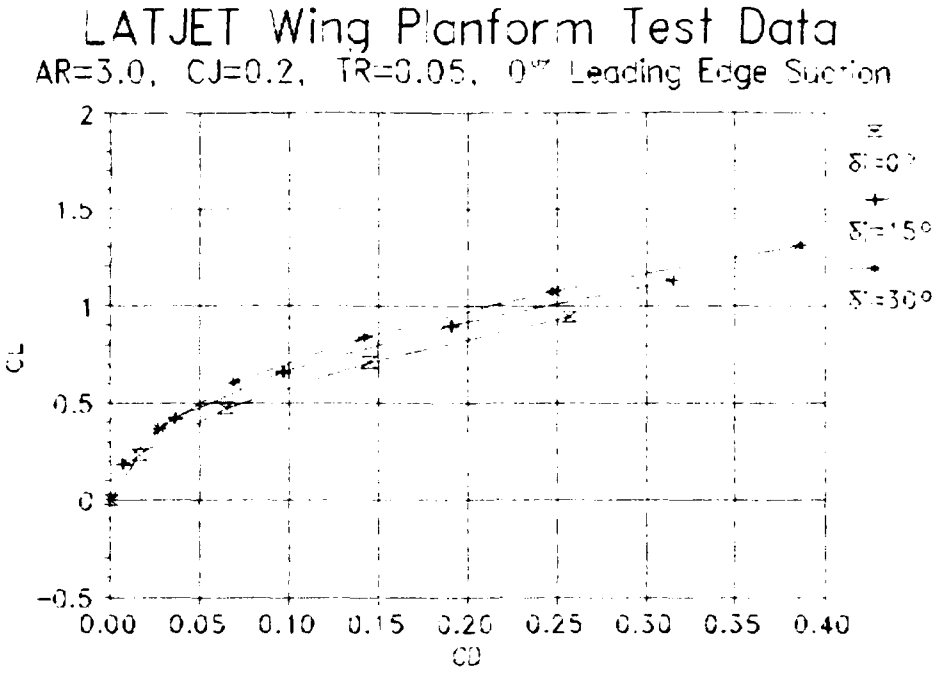

Figure 104 Drag Polar Comparison for δ_j, AR=3, λ=0.05

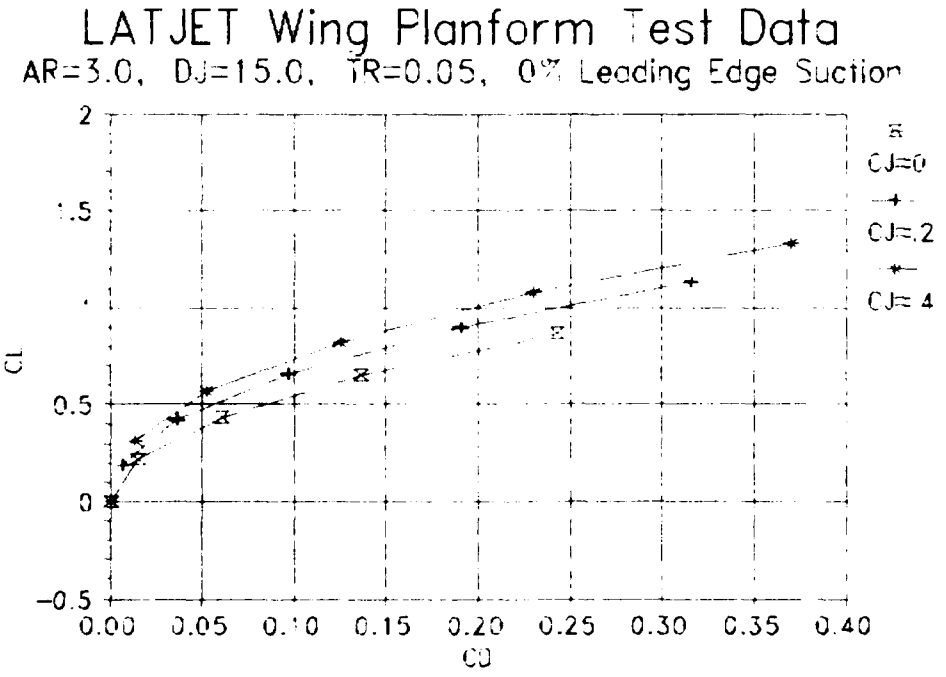

Figure 105 Drag Polar Comparison for BC, AR=3, λ=0.05

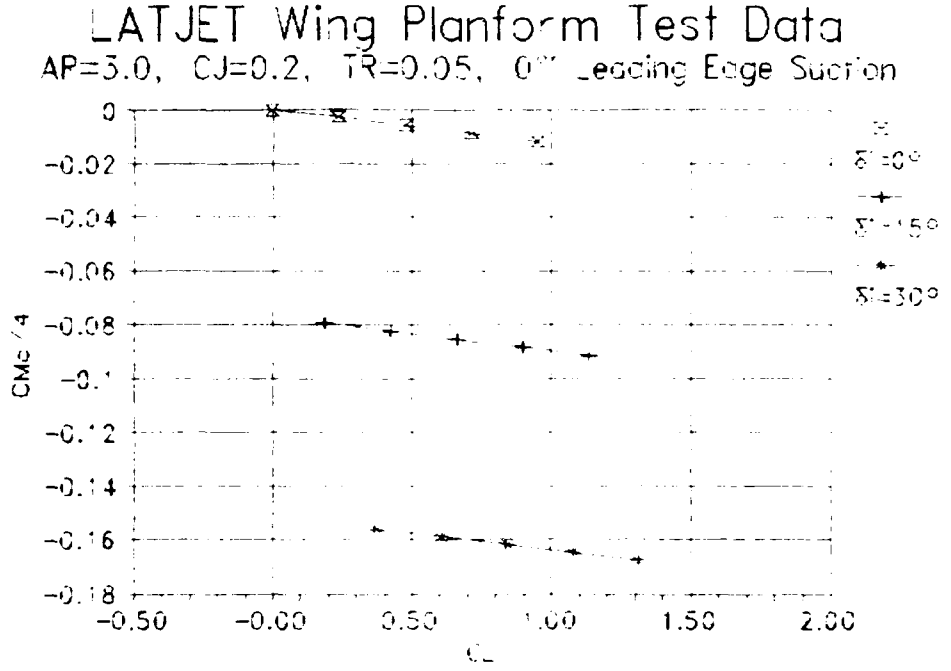

Figure 106 Moment Comparison for δj, AR=3, λ=0.05

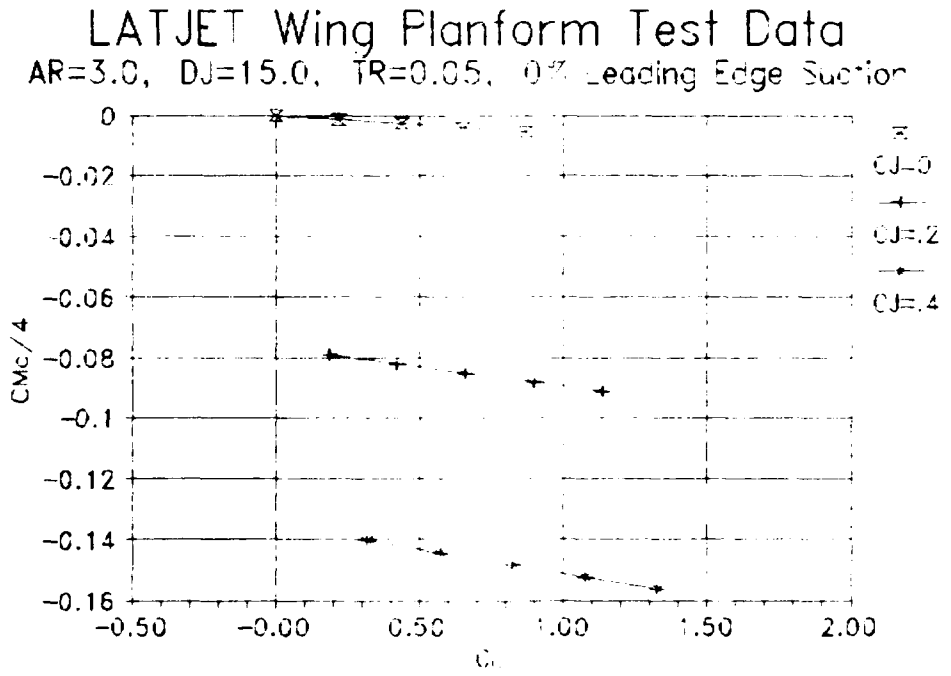

Figure 107 Moment Comparison for BC, AR=3, λ=0.05

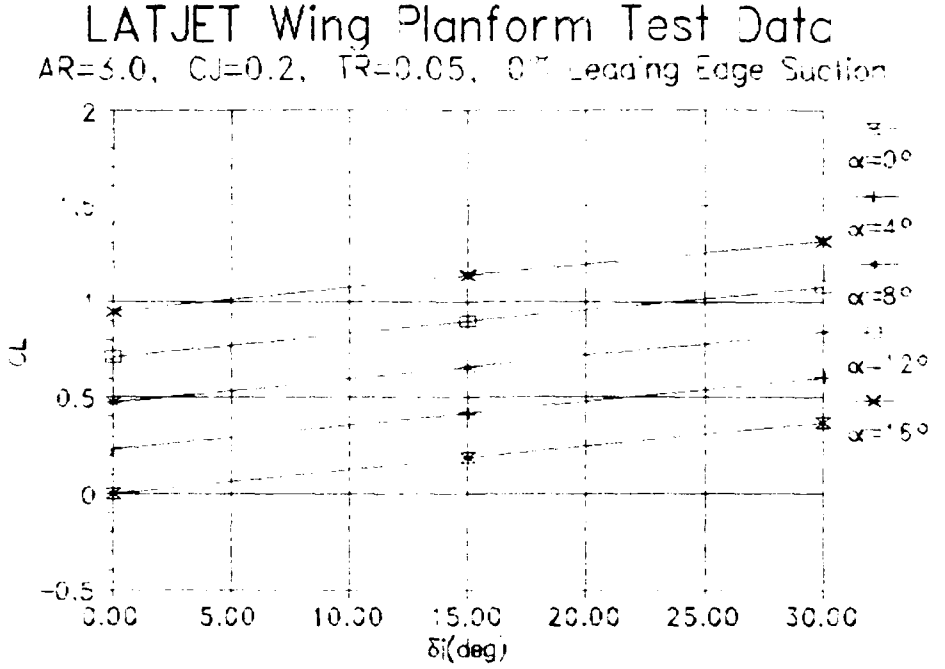

Figure 108 Lift vs δ_j, AR=3, λ=0.05

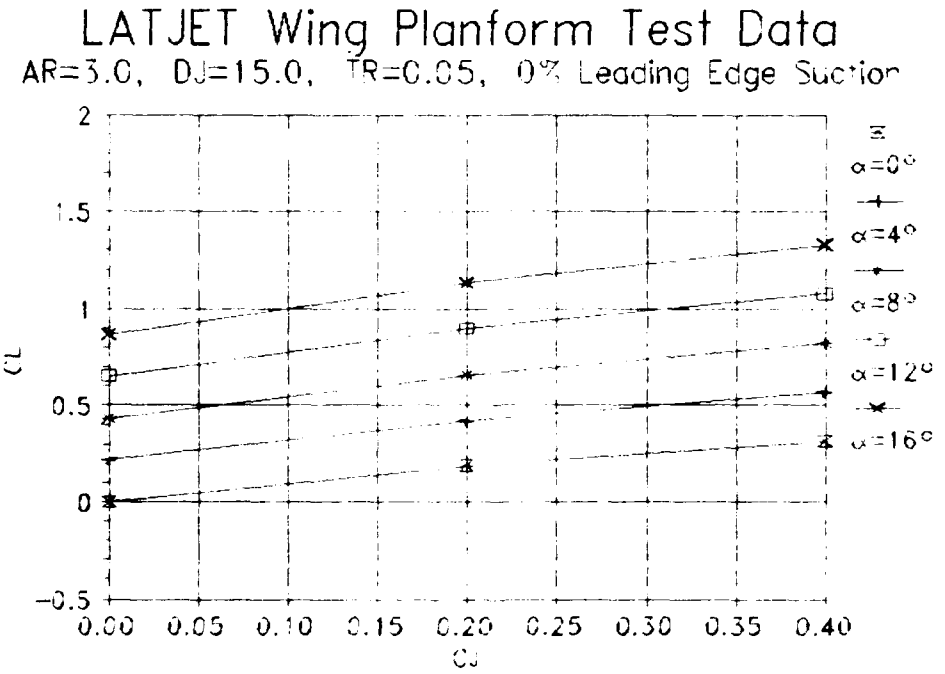

Figure 109 Lift vs C_j, AR=3, λ=0.05

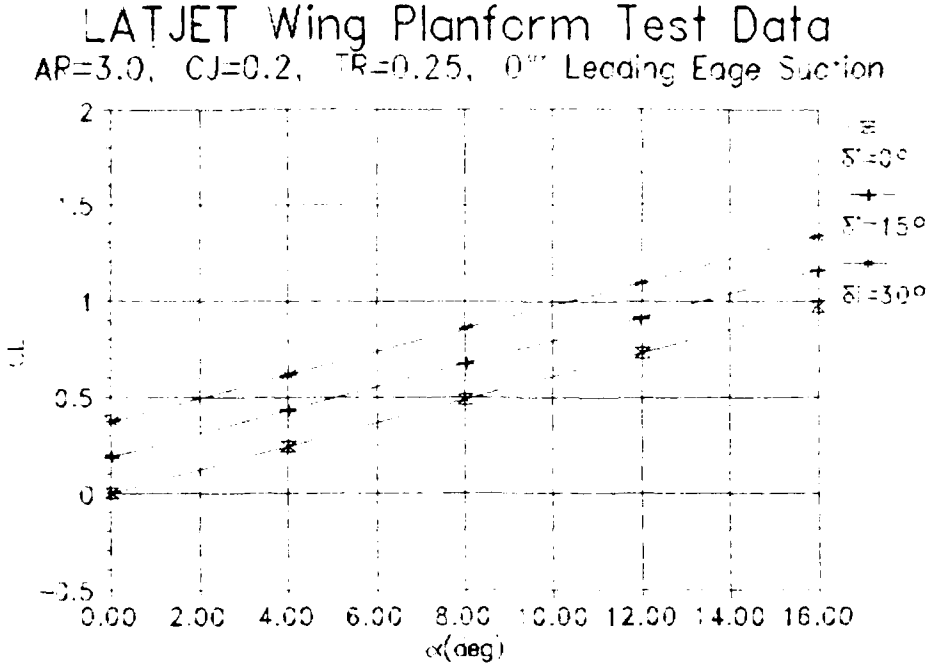

Figure 110 Lift Curve Comparison for δ_j, AR=3, λ=0.25

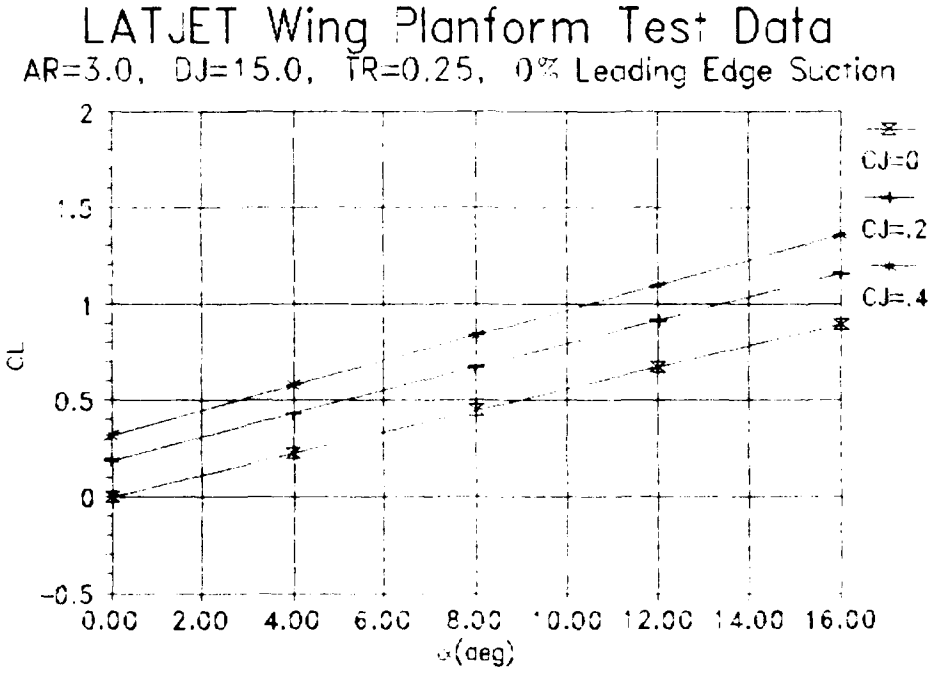

Figure 111 Lift Curve Comparison for BC, AR=3, λ=0.25

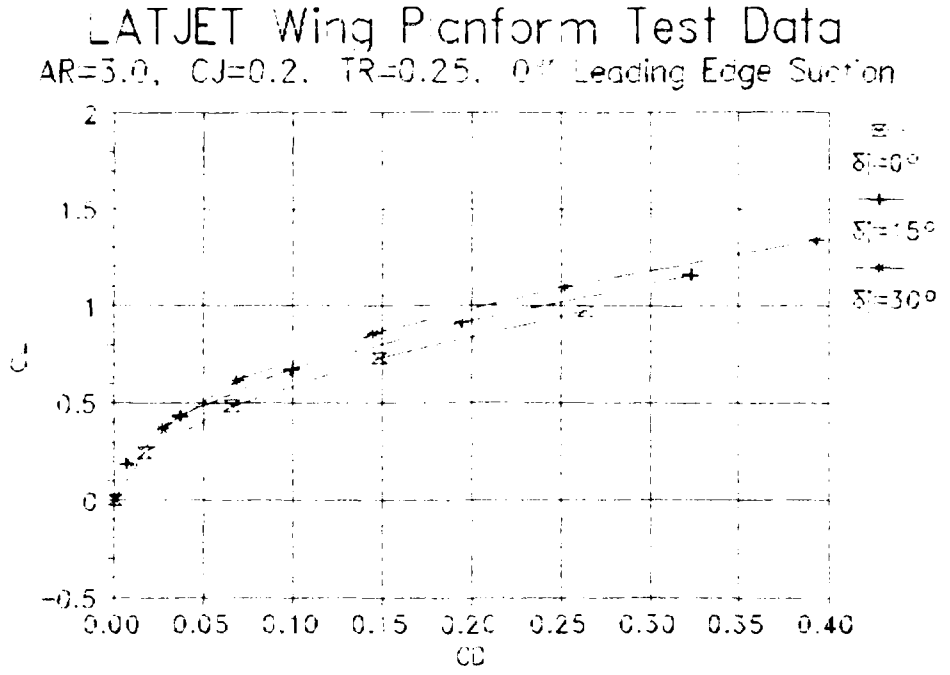

Figure 112 Drag Polar Comparison for δ_j, AR=3, λ=0.25

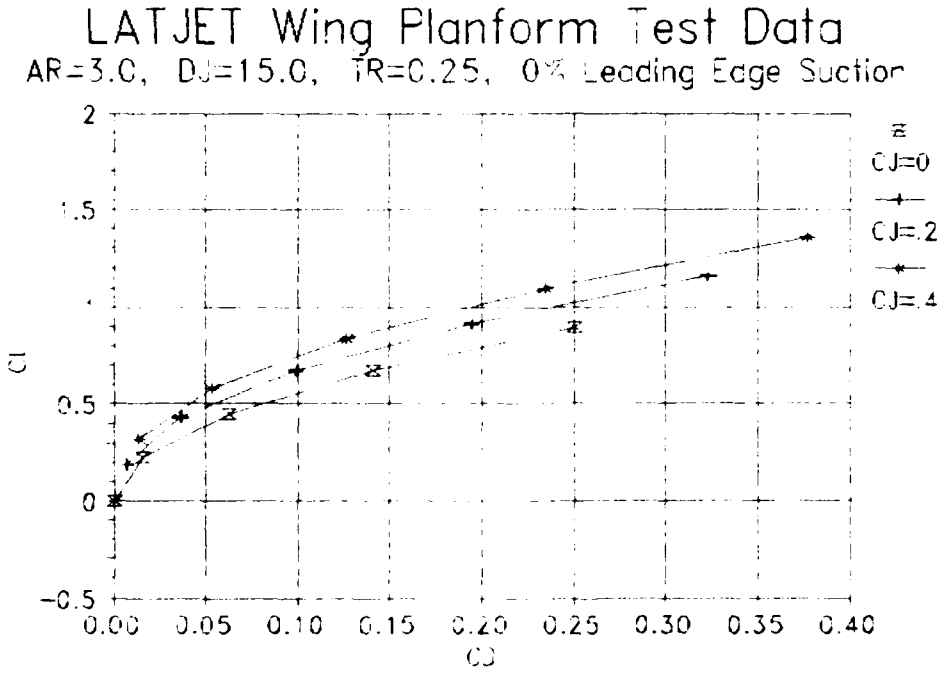

Figure 113 Drag Polar Comparison for BC, AR=3, λ=0.25

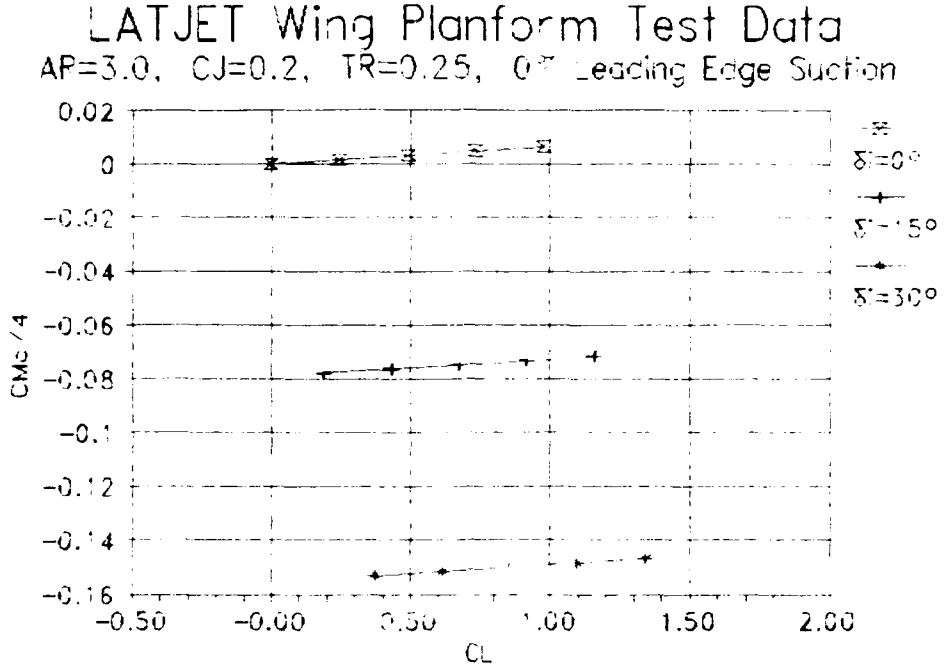

Figure 114 Moment Comparison for δj, AR=3, λ=0.25

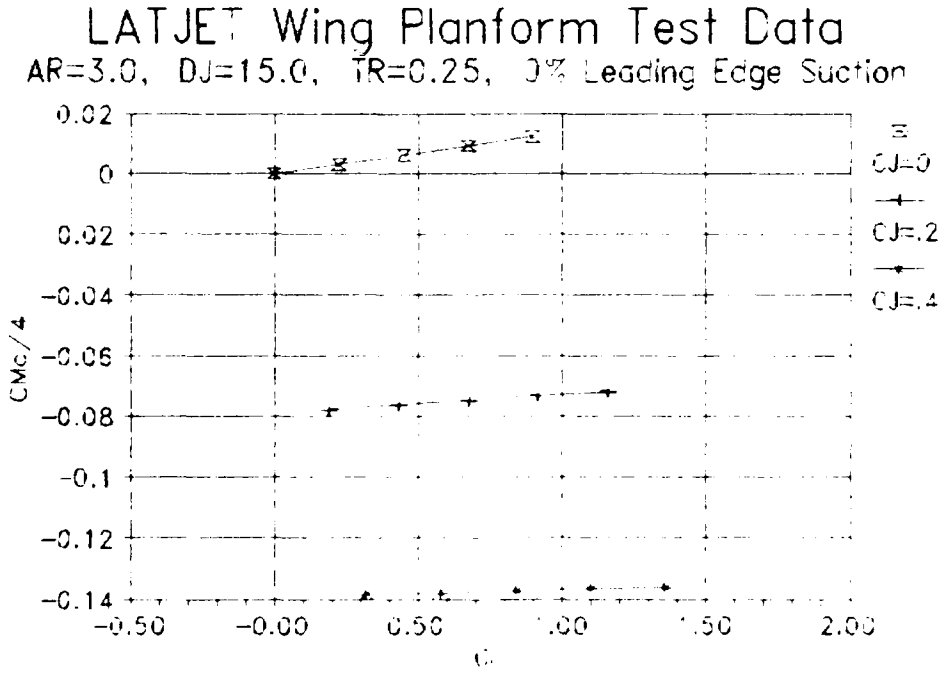

Figure 115 Moment Comparison for BC, AR=3, λ=0.25

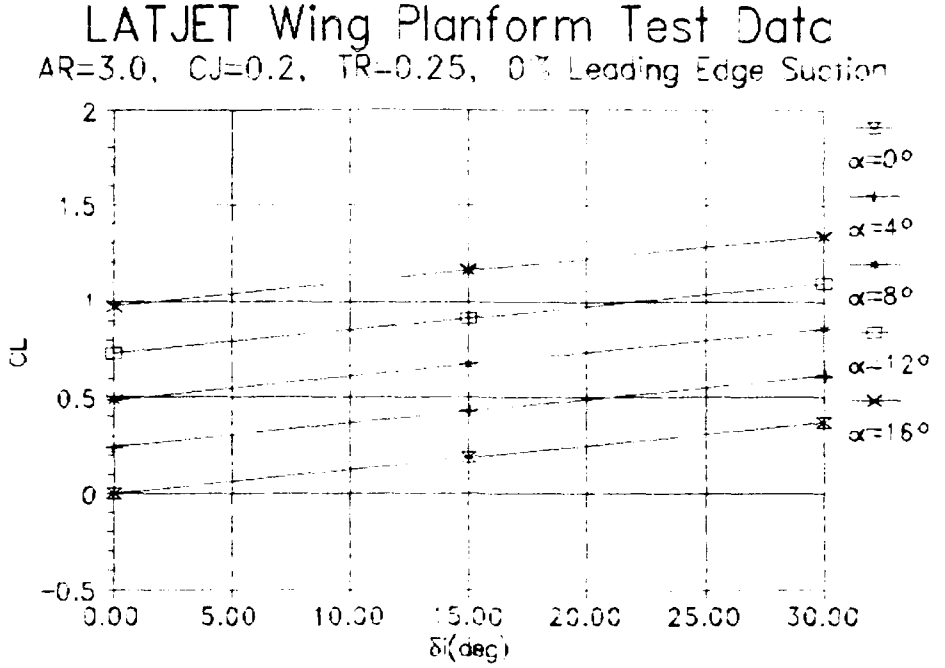

Figure 116 Lift vs δ_j, AR=3, λ=0.25

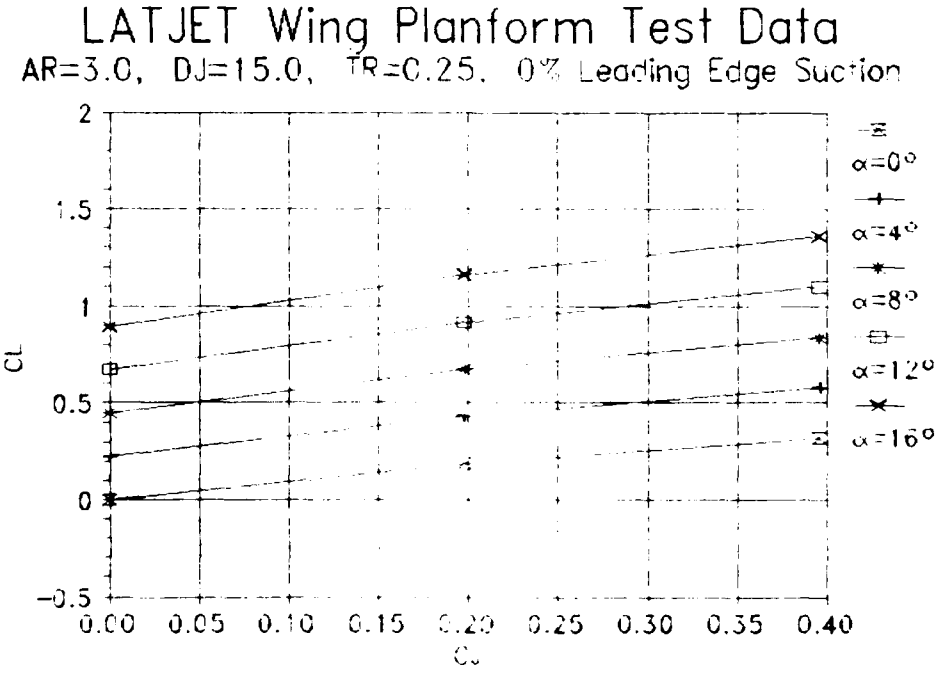

Figure 117 Lift vs C_j, AR=3, λ=0.25

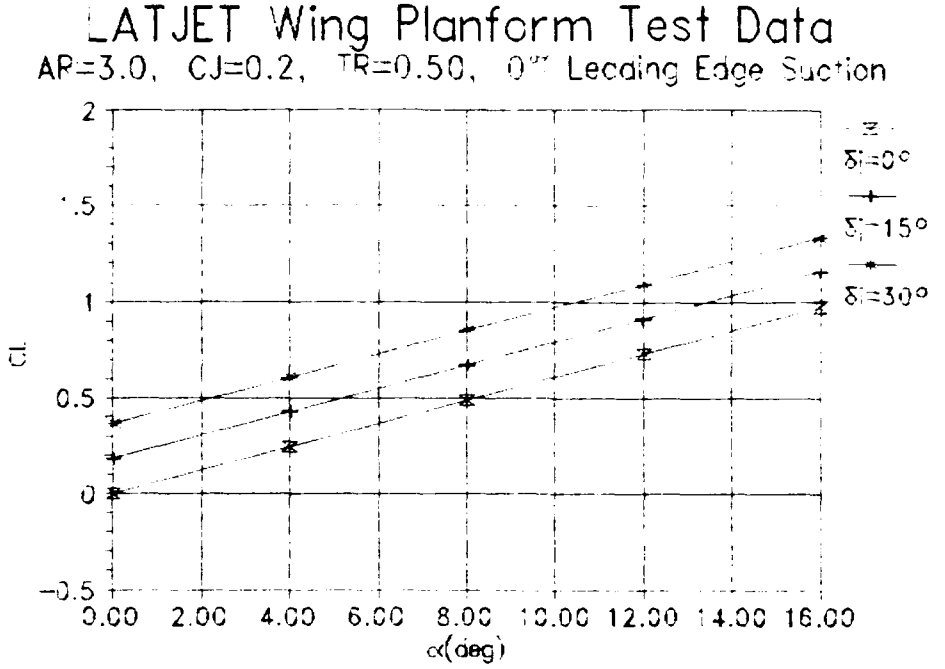

Figure 118 Lift Curve Comparison for δ_j, AR=3, λ=0.5

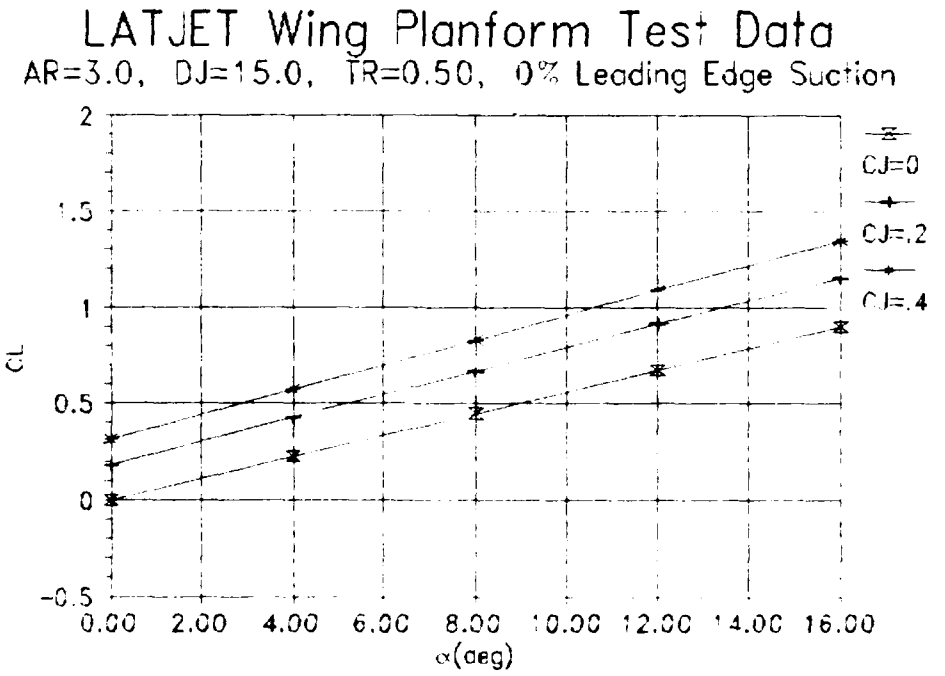

Figure 119 Lift Curve Comparison for BC, AR=3, λ=0.5

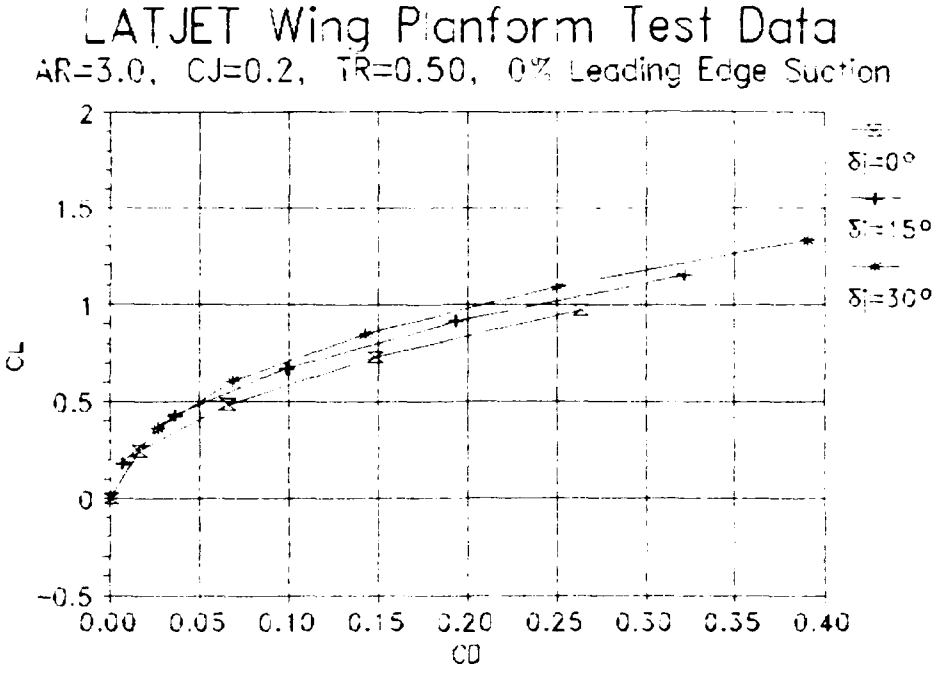

Figure 120 Drag Polar Comparison for δ_j, AR=3, λ=0.5

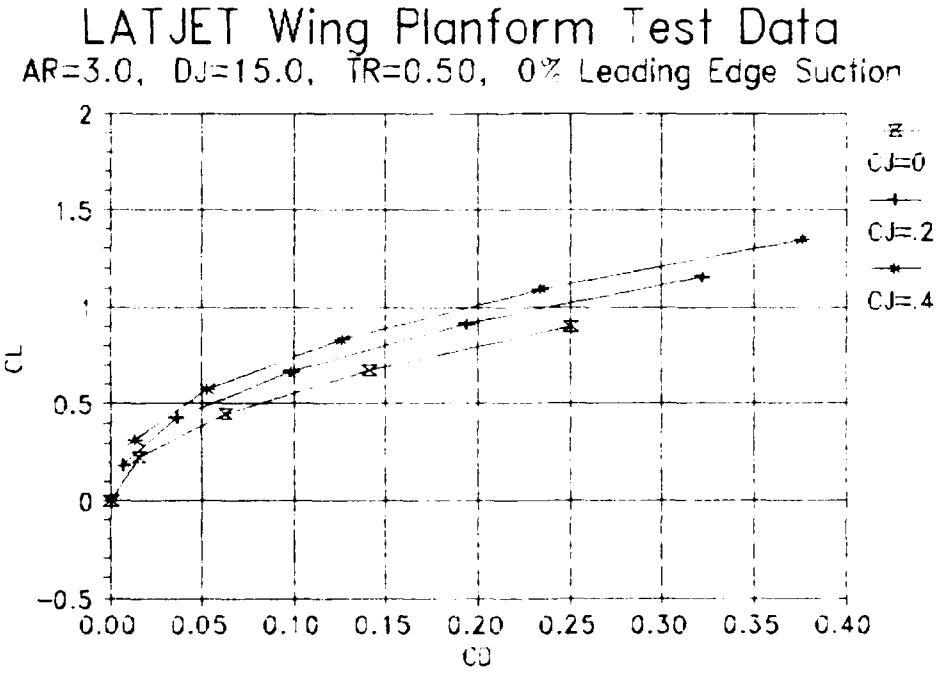

Figure 121 Drag Polar Comparison for BC, AR=3, λ=0.5

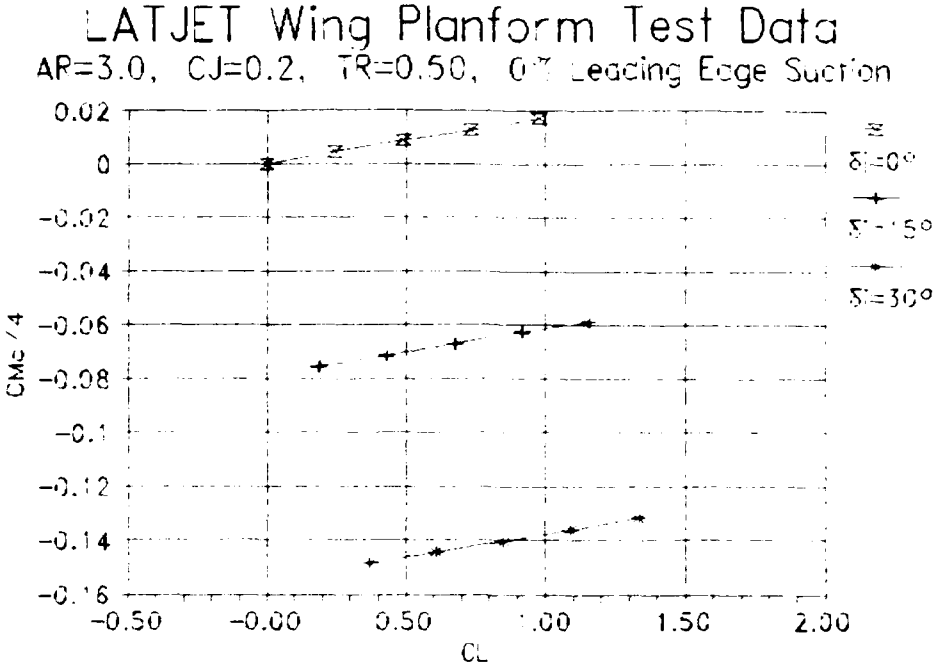

Figure 122 Moment Comparison for δj, AR=3, λ=0.5

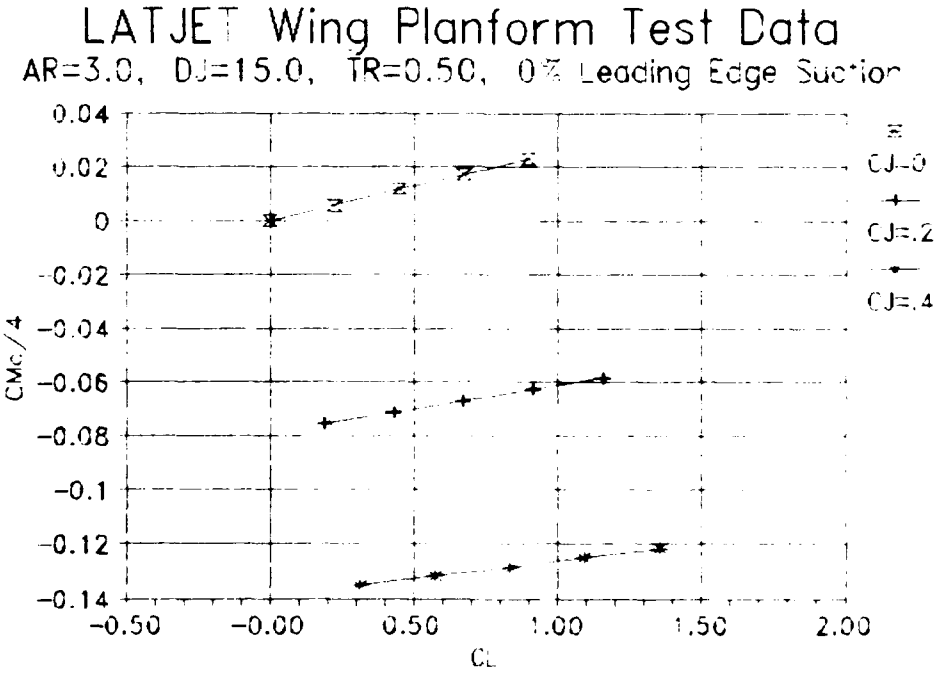

Figure 123 Moment Comparison for BC, AR=3, λ=0.5

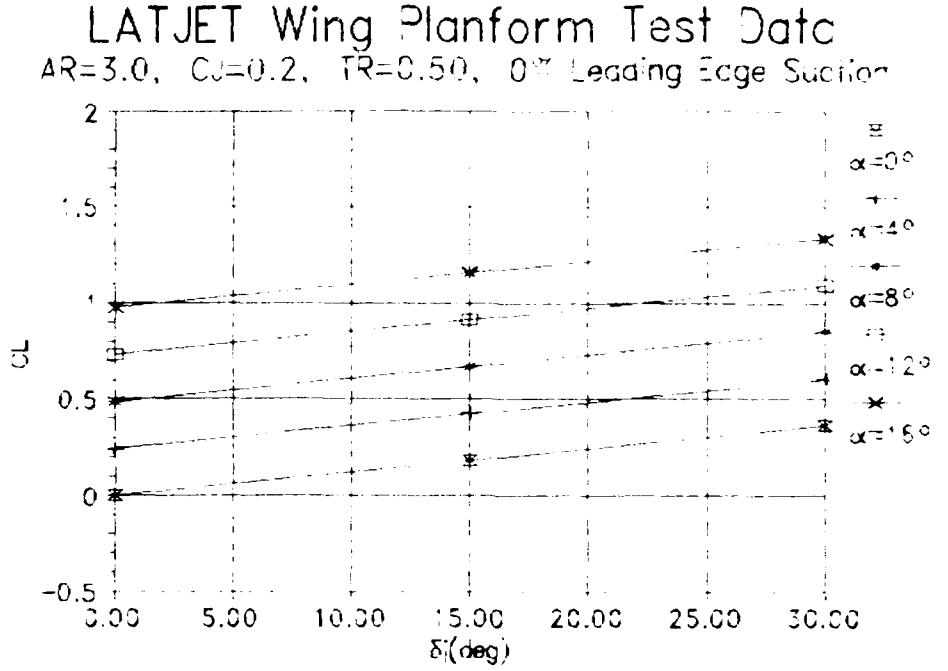

Figure 124 Lift vs δ_j, AR=3, λ=0.5

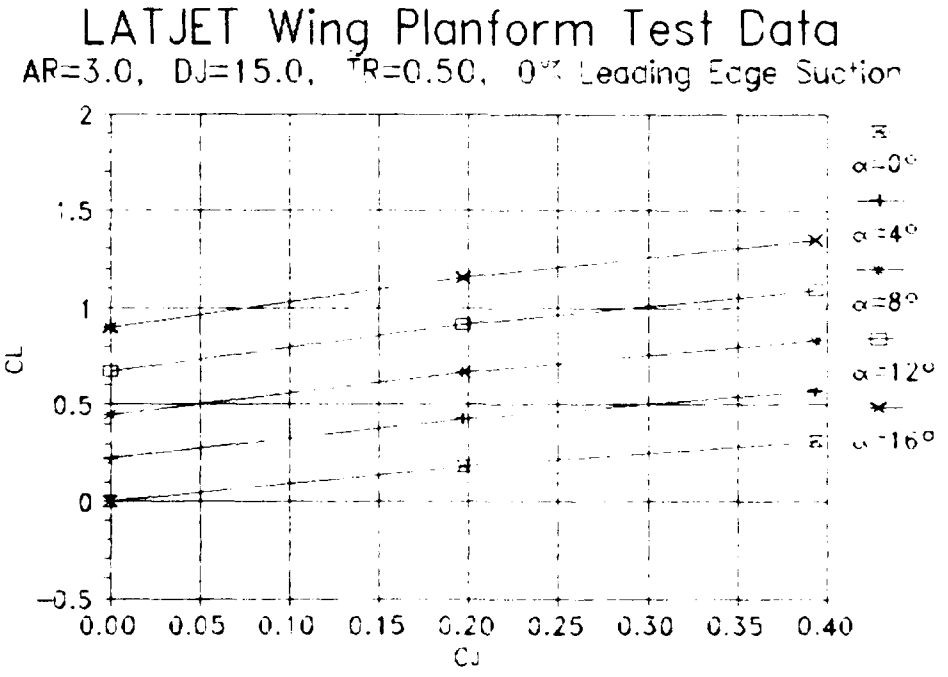

Figure 125 Lift vs C_j, AR=3, λ=0.5

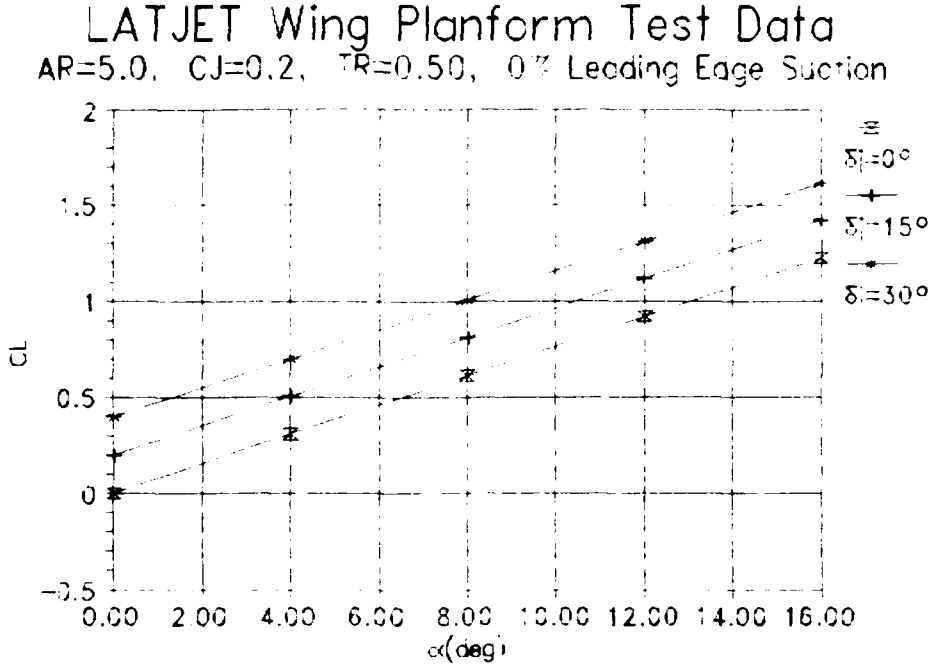

Figure 126 Lift Curve Comparison for δ_j, AR=5, λ=0.5

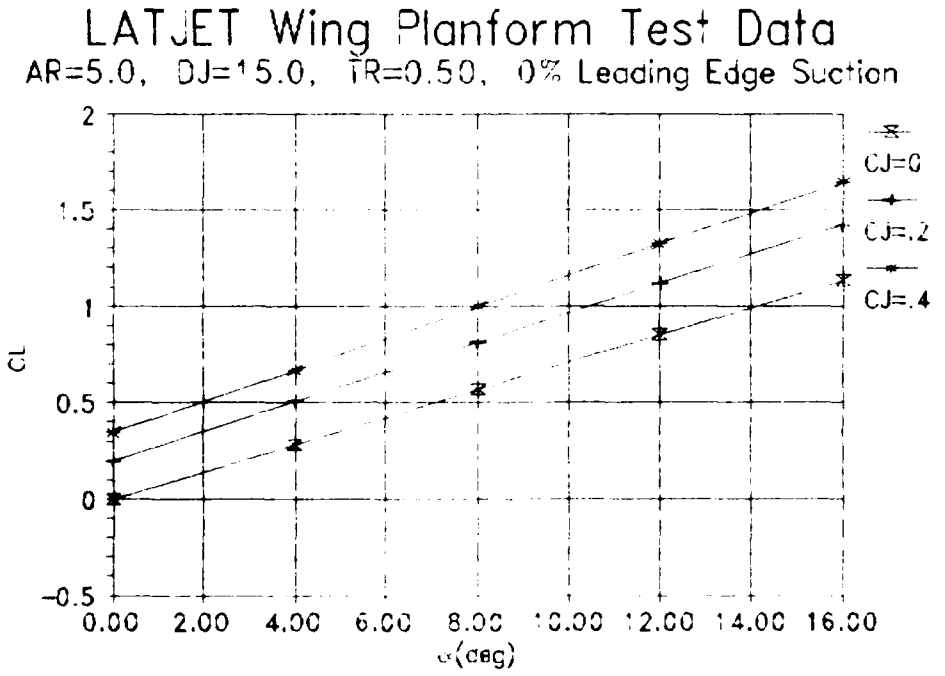

Figure 127 Lift Curve Comparison for BC, AR=5, λ=0.5

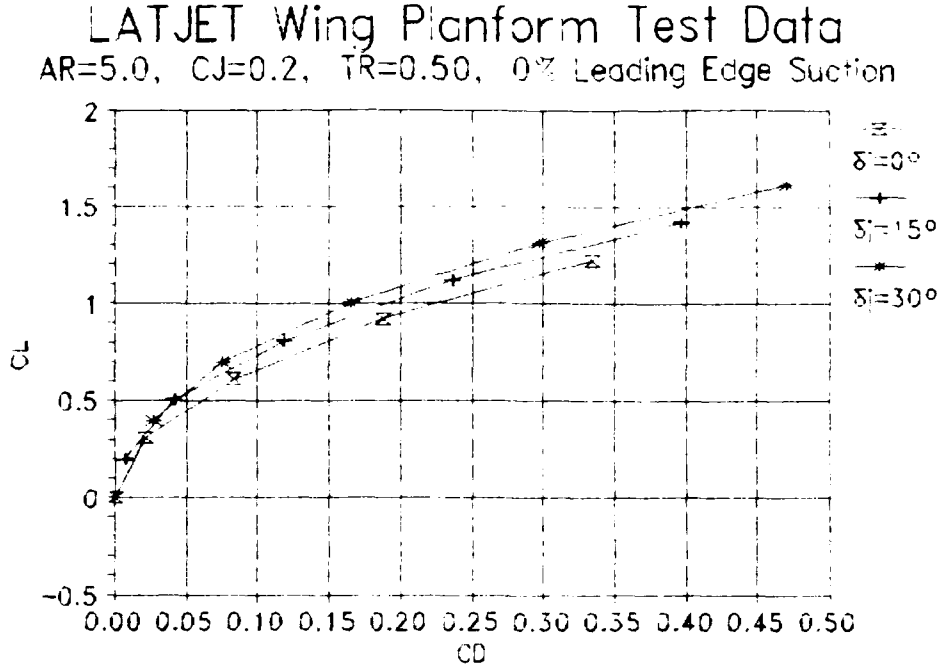

Figure 128 Drag Polar Comparison for δ_j, AR=5, λ=0.5

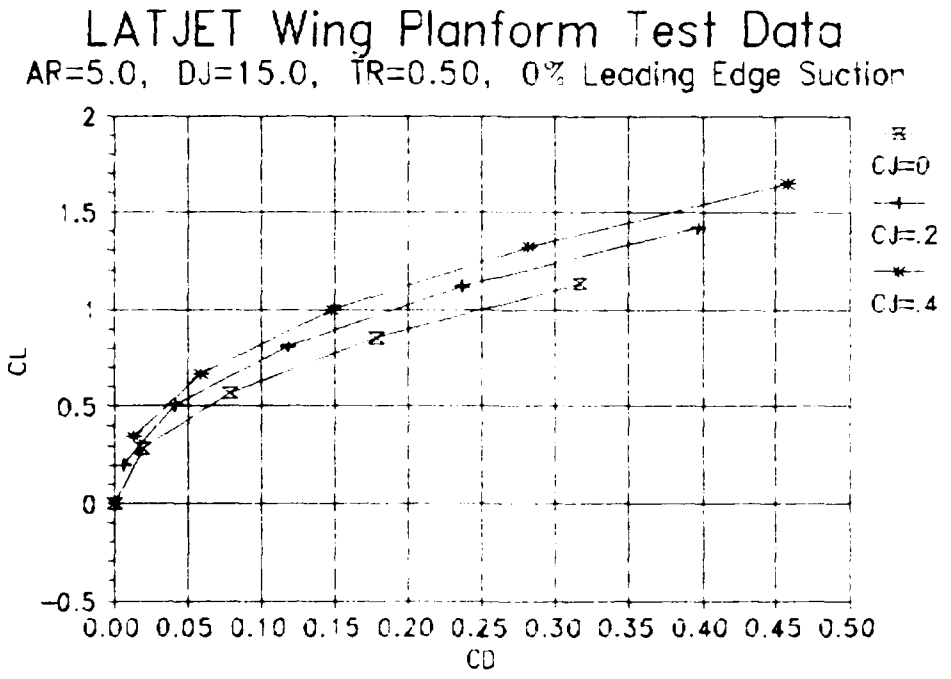

Figure 129 Drag Polar Comparison for BC, AR=5, λ=0.5

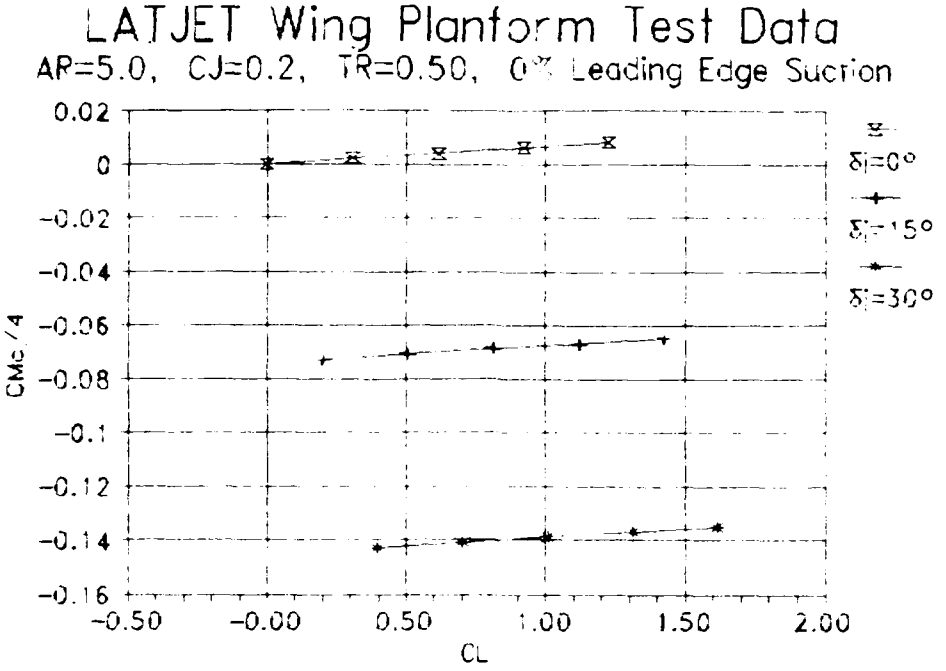

Figure 130 Moment Comparison for δj, AR=5, λ=0.5

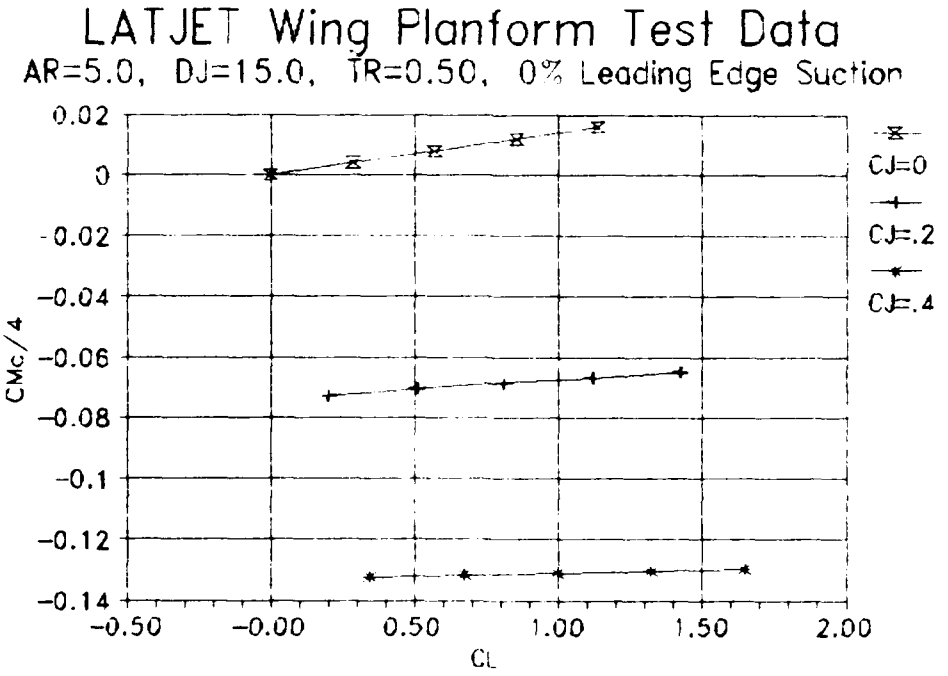

Figure 131 Moment Comparison for BC, AR=5, λ=0.5

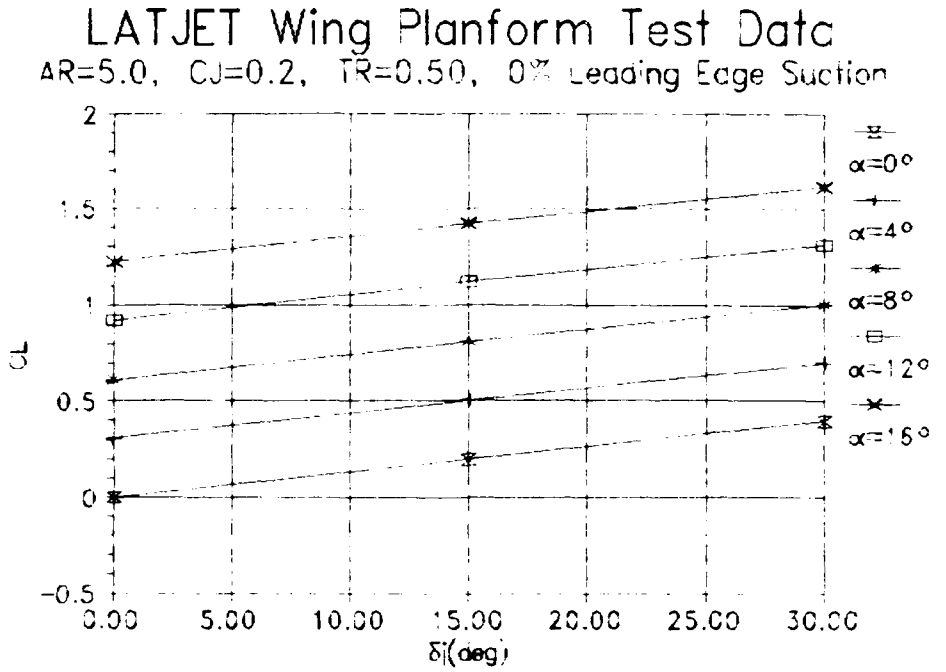

Figure 132 Lift vs δ_j, AR=5, λ=0.5

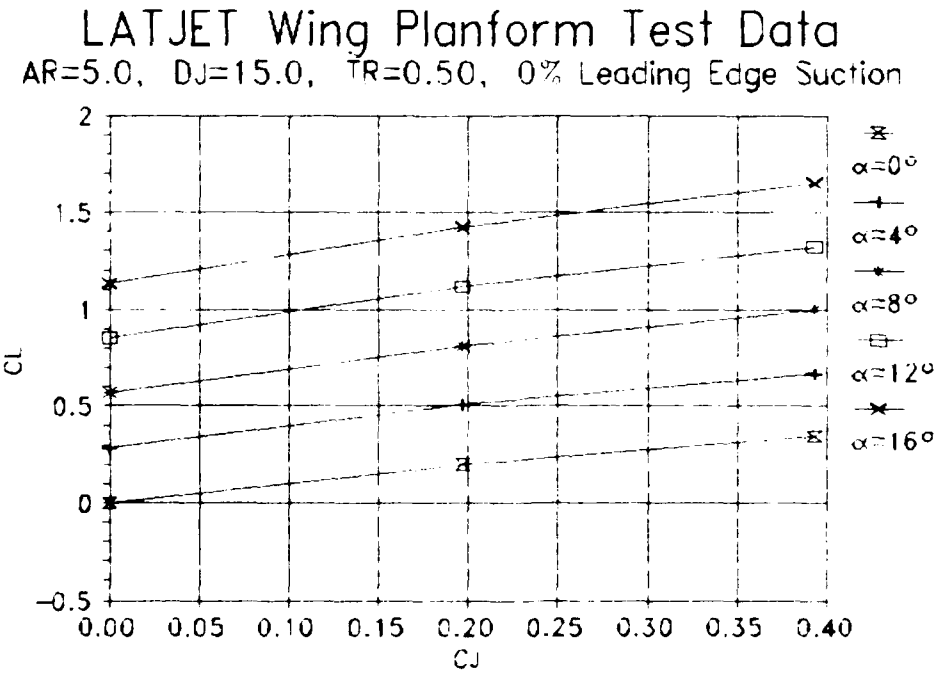

Figure 133 Lift vs C_J, AR=5, λ=0.5

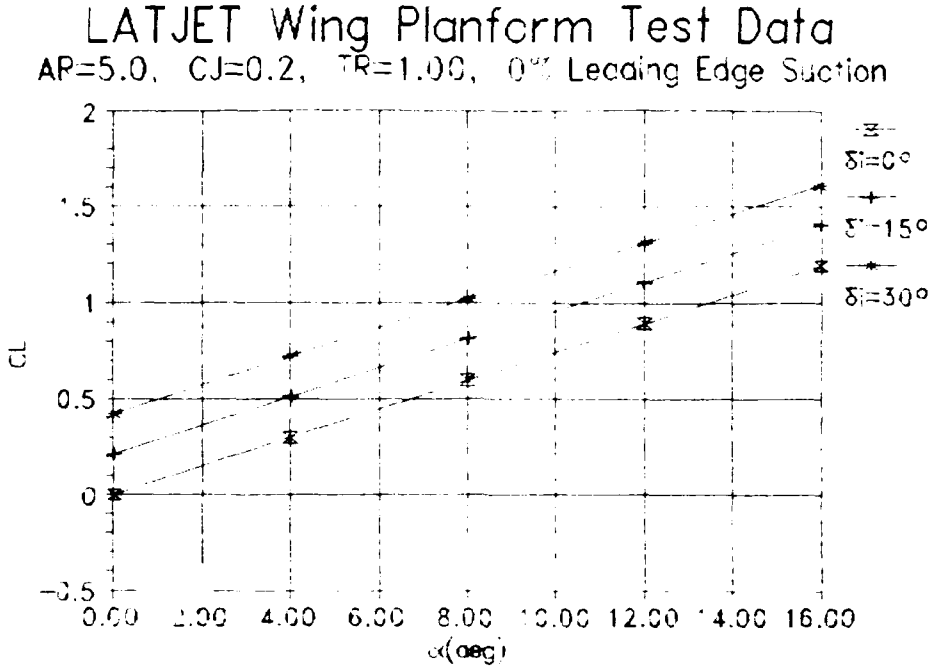

Figure 134 Lift Curve Comparison for δ_j, AR=5, λ=1

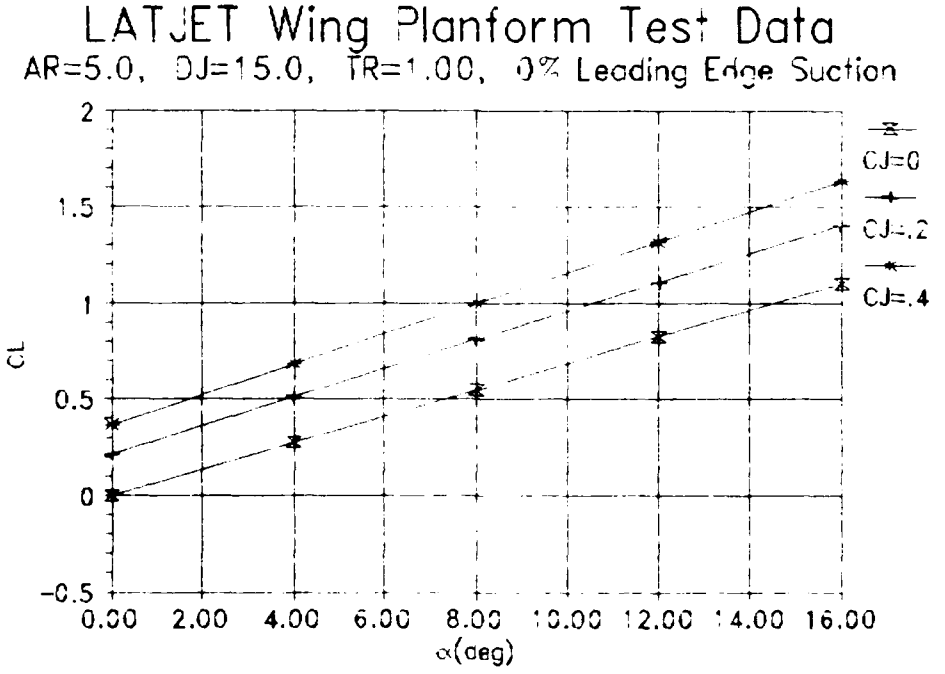

Figure 135 Lift Curve Comparison for BC, AR=5, λ=1

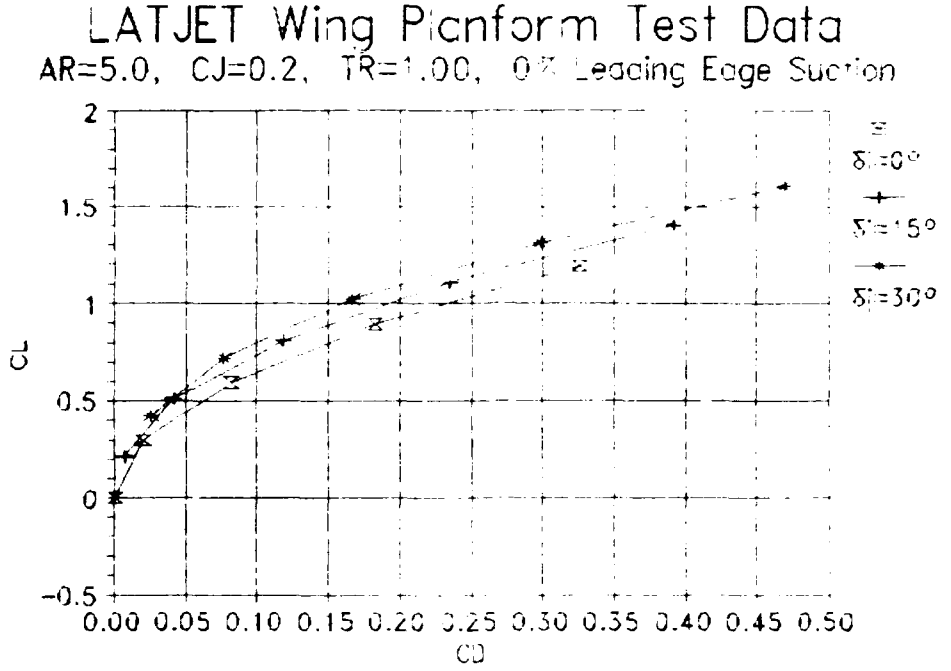

Figure 136 Drag Polar Comparison for δ_j, AR=5, λ=1

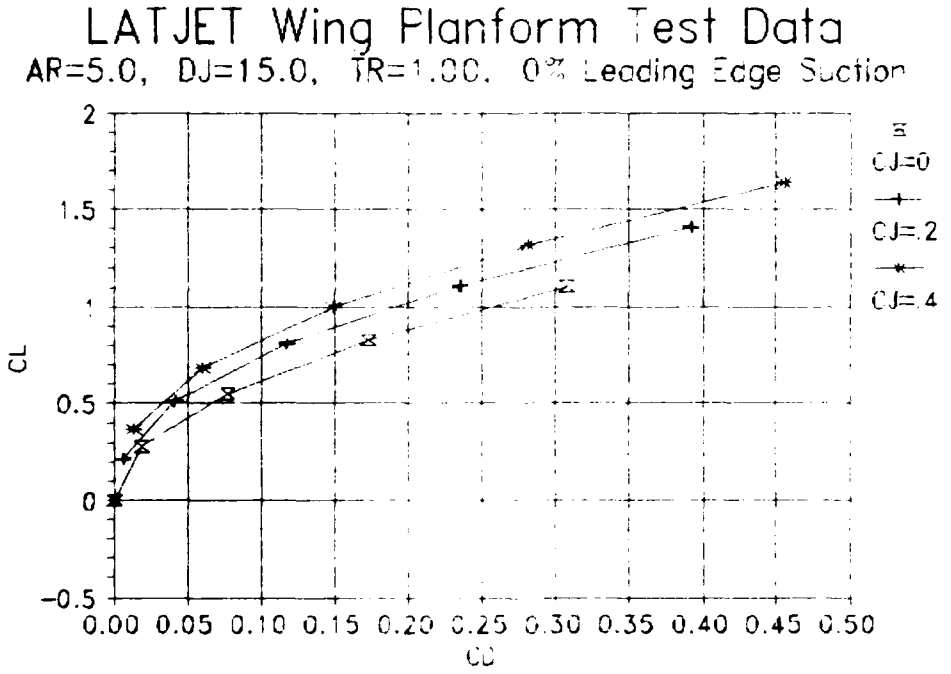

Figure 137 Drag Polar Comparison for BC, AR=5, λ=1

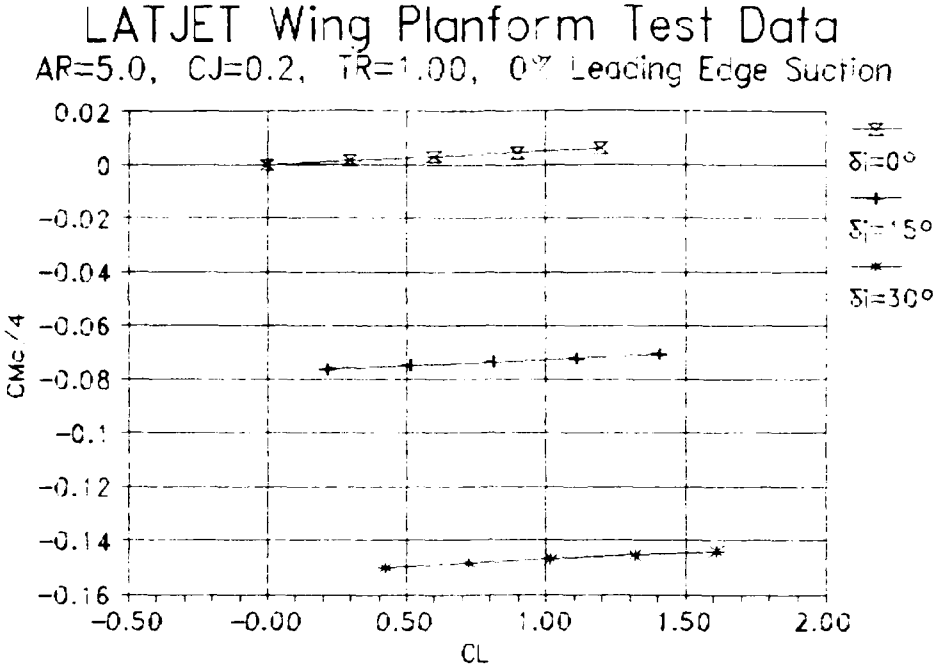

Figure 138 Moment Comparison for δj, AR=5, λ=1

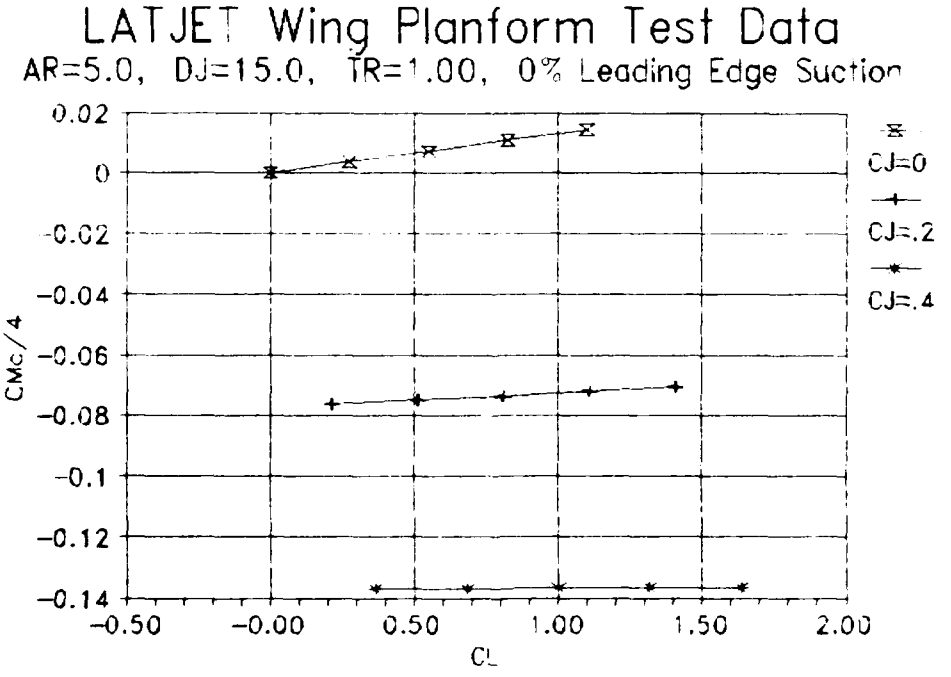

Figure 139 Moment Comparison for BC, AR=5, λ=1

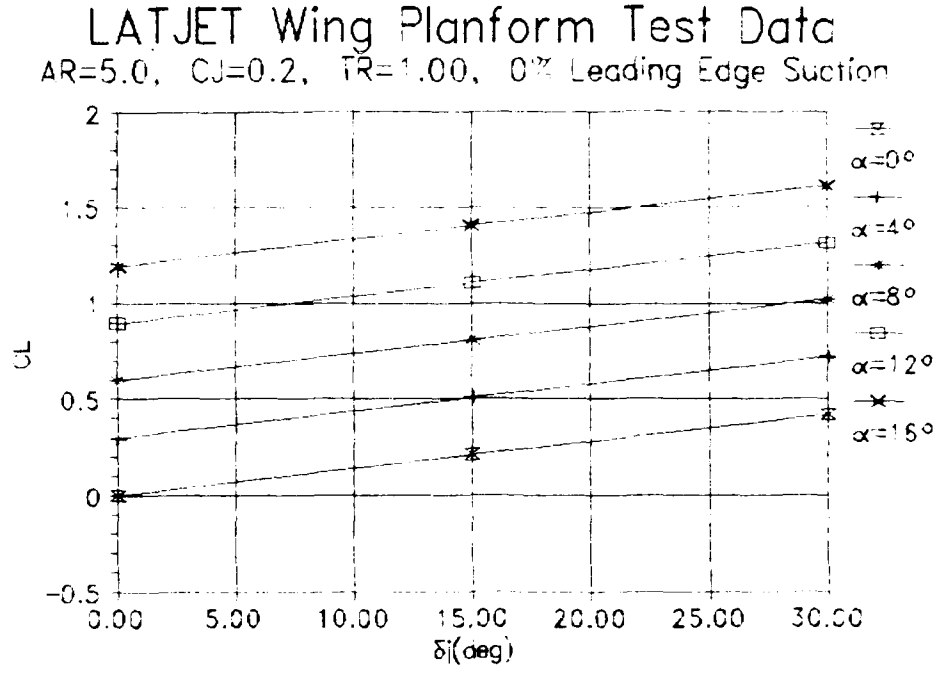

Figure 140 Lift vs δ_j, AR=5, λ=1

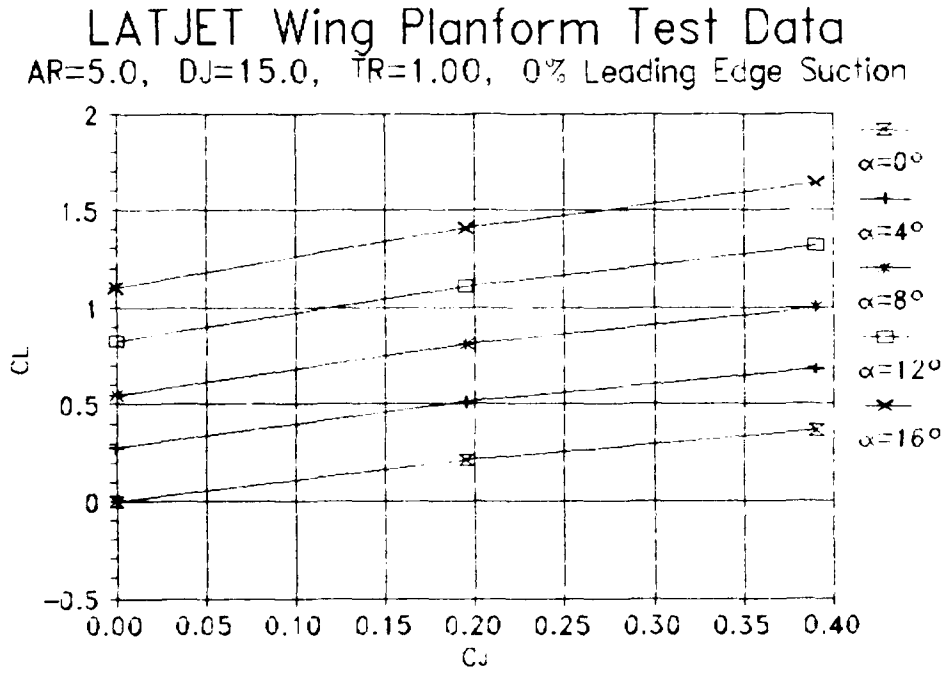

Figure 141 Lift vs C_j, AR=5, λ=1

REPORT DOCUMENTATION PAGE

Form Approved
OMB No. 0704-0188

1. AGENCY USE ONLY *(Leave blank)*	2. REPORT DATE	3. REPORT TYPE AND DATES COVERED
	December 1991	Master's Thesis

4. TITLE AND SUBTITLE
Analysis of an Advanced Fighter Aircraft Using Jet Flap Techniques and the Vortex Lattice Method

5. FUNDING NUMBERS

6. AUTHOR(S)
Steven P. Snyder, Captain, USAF

7. PERFORMING ORGANIZATION NAME(S) AND ADDRESS(ES)
Air Force Institute of Technology, WPAFB OH 45433-6583

8. PERFORMING ORGANIZATION REPORT NUMBER
AFIT/GAE/ENY/91D-27

9. SPONSORING/MONITORING AGENCY NAME(S) AND ADDRESS(ES)
WL/XPAD, WPAFB OH 45433

ASD/XRH, WPAFB OH 45433

10. SPONSORING/MONITORING AGENCY REPORT NUMBER

11. SUPPLEMENTARY NOTES

12a. DISTRIBUTION/AVAILABILITY STATEMENT
Approved for public release; distribution unlimited

12b. DISTRIBUTION CODE

13. ABSTRACT *(Maximum 200 words)*

A computer code employing the vortex lattice method with modified boundary conditions was used to determine the induced aerodynamic characteristics of high aspect ratio, vectoring, exhaust nozzles located at the wing root of a canard configured fighter aircraft. Comparison with existing wind tunnel data verified results of the method. The exhaust was modeled as a singularly blown jet flap at deflection angles of -10, 0, 10, 20, 30, and 40 degrees. Jet momentum coefficients were based gross engine thrust for maximum afterburner and military power settings at a Mach number of 0.6 and an altitude of 20,000 ft. Lift, induced drag, and pitching moment coefficients were calculated for untrimmed conditions. The nozzle provided lift augmentation at all deflections and blowing conditions, a reduction in induced drag at high lift coefficients, and an increased nose down pitching moment. An optimum flap deflection to achieve minimum induced drag existed for each unique lift and blowing condition. Measurement of the static margin showed that the aircraft as configured was statically unstable. Example cases of comparable wing planforms varying in aspect ratio from 2 to 5 and taper ratio from 0.05 to 1 showed similar behavior.

14. SUBJECT TERMS	15. NUMBER OF PAGES
Fighter Aircraft, Jet Flaps, Paneling Methods Aerodynamic Prediction Methods	138
	16. PRICE CODE

17. SECURITY CLASSIFICATION OF REPORT	18. SECURITY CLASSIFICATION OF THIS PAGE	19. SECURITY CLASSIFICATION OF ABSTRACT	20. LIMITATION OF ABSTRACT
Unclassified	Unclassified	Unclassified	UL